University of Milano-Bicocca

Department of Physics "G. Occhialini"

PhD program in Physics and Astronomy – Cycle XXXIII
Plasma Physics Curriculum

Reconstruction of the velocity space of runaway electrons by spectral measurements of the hard X-ray emission in tokamaks

---

Candidate:
Andrea Dal Molin

Registration Number:
745763

Tutor:
Dr. Marco Tardocchi

Supervisor:
Prof. Massimo Nocente

Coordinator of the PhD School: Prof. Marta CALVI

Academic Year 2019/2020

"The issue of current transfer from thermal to relativistic electrons is central to the success of the ITER program but far less central to the success of magnetic fusion energy. For example, little change would occur in stellarator reactor designs if the constraint were imposed that the net plasma current must be smaller than 5 MA."

Allen H. Boozer [1]

UNIVERSITY OF MILANO-BICOCCA

Summary

Department of Physics "G. Occhialini"

Doctor of Philosophy

RECONSTRUCTION OF THE VELOCITY SPACE OF RUNAWAY ELECTRONS BY SPECTRAL MEASUREMENTS OF THE HARD X-RAY EMISSION IN TOKAMAKS

by Andrea DAL MOLIN

Magnetically confined fusion research is stepping into a new phase of its journey. New large-size tokamaks, such as DTT, JT-60SA and ITER are currently being built across the globe. These massive devices are expected to prove the feasibility of nuclear fusion as a large-scale and carbon-free source of energy. The formation of uncontrolled runaway electron beams currently represents one of the major obstacles to the success of these devices. The growth of plasma instabilities can cause a sudden loss of thermal and magnetic energy. In this disruptive event, electrons can be accelerated to relativistic energies and gain a significant fraction of the energy stored in the tokamak magnetic field. At these velocities, Coulomb collisions with background plasma become negligible and the acceleration of the runaway electrons is only limited by relativistic effects and radiative losses. When the post-disruption magnetic field is lost, the energetic runaway electron beam can collide with the in-vessel plasma-facing components causing severe and localized damage. Unmitigated runaway electron events can hinder operation by forcing long shutdown periods of several months to allow repairs. The avoidance of these extreme scenarios is paramount to the success of large-scale tokamaks. The threat posed by runaway electrons is a primary focus in the fusion community. Extensive modelling and experimental campaigns are currently ongoing in most large and medium-scale tokamaks to refine prediction, avoidance and mitigation of these events.

During disruptions, runaway electrons can be accelerated up to energies in the order of several MeVs. One of the mechanisms that limit this acceleration is the emission of bremsstrahlung radiation caused by the interaction of the relativistic particles with the background plasma. Due to the extreme energy these electrons can reach, the bremsstrahlung radiation spectrum extends up to several MeVs, in hard X-ray energy range. This work illustrates how information on the runaway electron velocity space can be extracted from spectral analysis of the measured bremsstrahlung X-ray emission.

The first half of this work is dedicated to the development, characterization and implementation of novel hard X-ray spectrometers optimized for runaway electron bremsstrahlung measurement. Optimized diagnostics are needed to fulfil the strict requirements both posed by the challenging nature of the runaway electron bremsstrahlung radiation and by the harsh environment of a tokamak.

A new compact LYSO:Ce HXR spectrometer was developed as an upgrade of the existing DIII-D Gamma Ray Imager (GRI) diagnostic BGO detectors. The prototype achieved a wide dynamic range in excess of 25 MeV with an energy resolution of approximately 9% at 661.7 keV and counting rate capabilities in excess of 1 MCps. The spectrometer performance allows for successful measurement of the runaway electron bremsstrahlung radiation. In this application, a silicon photomultiplier was used as a photodetector. This allows the spectrometer to operate under the strong magnetic fields experienced at the GRI location that are caused by the close proximity to the tokamak. The effects of energy non-linearity introduced by the silicon photomultiplier were characterized to allow for off-line correction. The LYSO:Ce prototype was tested at the DIII-D tokamak and proved to be 1000 times faster than the existent GRI BGO detector, expanding the diagnostic counting rate capability of approximately three orders of magnitude. The improved diagnostic capabilities contributed to the observation of novel correlations between the RE energy and the insurgence of kinetic instabilities during the current quench phase of a disruption.

Even if the LYSO:Ce prototype largely expanded the amount of HXR flux the GRI could withstand by approximately three orders of magnitude, in many RE scenarios the volume of radiation was too large and the detector was unable to provide information on the single HXR event energy. A new compact HXR spectrometer is under development to further expand the GRI capability to sustain severe HXR fluxes by one additional order of magnitude. This improvement would allow the detector to successfully measure the large portion of RE scenarios at DIII-D. The new prototype design is based on a smaller YAP:Ce scintillator crystal coupled with a silicon photomultiplier. Both the scintillator material and the crystal dimensions were carefully chosen to reduce the detection efficiency while still providing the required properties needed for HXR spectroscopy. The detector has a wide dynamic range in excess of 20 MeV, an energy resolution of approximately 9% at 661.7 keV and a counting rate capability in excess of 1 MCps. The characterization of the YAP:Ce prototype is now complete and tests at the DIII-D tokamak are expected in the near future.

Finally, an additional novel hard X-ray spectrometer optimized for RE bremsstrahlung measurement was developed as part of this thesis. The Runaway Electron GAmma-Ray Detection System (REGARDS) is a portable system designed to be deployed at different medium-sized tokamaks. The detector is based on a LaBr3:Ce scintillator crystal coupled with a photomultiplier tube. A gain control system was

developed to monitor the detector stability under evolving magnetic fields and high HXR fluxes. The system offers a wide energy dynamic range for HXR spectroscopy with an upper bound in excess of 20 MeV and an energy resolution of approximately 3% at 661.7 keV. The counting rate capability of the system is in excess of 1 MCps. REGARDS high counting rate limitations were tested at the COMPASS tokamak where extreme HXR fluxes in excess of 10 MCps were observed. REGARDS was deployed during the experimental campaign at the tokamak AUG where it successfully collected valuable HXR data for many different runaway electron scenarios. REGARDS provided useful information on different mitigation techniques such as resonant magnetic perturbation and massive gas injection and the good quality of the collected data allowed for the reconstruction of the runaway electron energy distribution function for many relevant discharges.

The second half of this thesis is dedicated to the analysis of the runaway electron bremsstrahlung emission collected at the tokamaks AUG and JET. A forward discretized model of the bremsstrahlung emission was created using numerical codes. GENESIS was used to assess the bremsstrahlung radiation emitted by a generic runaway electron beam interacting with the post disruption plasma. Different target ion species were considered to accurately describe plasma composition after massive injections. MCNP models of the different HXR detectors were developed to compute the spectrometers response function and calculate the expected measured spectrum from a known incident radiation. The resulting discretized model was used to recover the runaway energy distribution function from the measured bremsstrahlung spectra. This inversion problem is generally ill-posed, where many solutions could explain the same measured HXR spectrum within the experimental error. First-order Tikhonov regularization algorithm was used to obtain a unique solution by reintroducing constraints such as non-negativity and smoothness.

Runaway electron experiments from the AUG and JET experimental campaigns were investigated using these techniques. The runaway electron energy distribution functions obtained from the measured HXR spectra were used to quantitatively describe the runaway electron beam evolution throughout the discharges. As a result, information useful to validate first-principle models and to evaluate the effectiveness of different runaway electron mitigation techniques such as massive gas injection, shattered pellet injection and magnetic resonant perturbation was provided. A thorough analysis of the data collected at AUG and JET is near completion.

The results presented in this thesis constitute a significant contribution to the development of hard X-ray spectrometers optimized for runaway electron bremsstrahlung measurement. Quantitative information on the energy distribution of runaway electrons and their interaction with post-disruption plasma can be inferred from HXR measurements providing valuable data to validate first-principle models and to evaluate the effectiveness of different runaway electron mitigation techniques.

Contents

Part I

Introduction

Chapter 1

Thermonuclear Fusion

1.1 Nuclear Fusion

Several issues would have to be addressed in the current century. The ever increasing energy demand, the environmental footprint of human activities and the constant growth rate of consumption of finite resources are amongst the most pressing.

Nuclear fusion is largely considered one of the most promising energy sources of the future. There are many reasons for its appeal: a low carbon-footprint, a high fuel abundance, a large energy release per reactant mass and intrinsic nuclear safety of operation are just a few of them. The possible applications of controlled nuclear fusion are vast and expand beyond energy production to deep space exploration and the creation of planetary defence systems against incoming comets [2].

Fusion occurs when two or more atomic nuclei overcome the Coulomb repulsion and merge together into a heavier atom under the effect of strong nuclear force. If the reactants are light isotopes with atomic masses lower than 56, net energy is released as a result of the reaction. This released energy equals the mass defect of the newly produced atom. For heavier isotopes (A > 56) the fusion reaction becomes endothermic and can not be used as a primary source of energy.

Light isotopes such as deuterium, tritium and helium-3 are currently considered the most promising reactants for their low Coulomb barrier and high energy release. The most relevant fusion reactions are

$$\begin{aligned} D + T &\rightarrow {}^4He + n + 17.6\,MeV & \\ D + D &\rightarrow \quad T + p + 4.03\,MeV & (50\%\ branching\ ratio) \\ &\rightarrow {}^3He + n + 3.27\,MeV & (50\%\ branching\ ratio) \\ D + {}^3He &\rightarrow {}^4He + p + 18.3\,MeV & \end{aligned}$$

The deuterium-tritium reaction (DT) shows the highest reactivity at (relatively) low temperatures. Deuterium has a comparably high natural abundance of approximately 0.02% and it could be harvested from water. On the other hand, tritium has a short half-time of approximately 12.32 years and therefore it can not be naturally harvested and must be artificially produced. In a future fusion reactor, tritium could be directly generated on-site, taking advantage of nuclear reactions between the fusion generated neutrons and lithium in special devices called *breeding blankets*.

Lithium is a relatively abundant element present in both Earth's oceans and crust. At the current rate of energy consumption, estimates show that fusion fuel reserves on Earth could last for thousands of years. If controlled thermonuclear fusion is achieved this would grant humankind a long-lasting reliable energy source.

Challenging conditions are needed to overcome the Coulomb repulsion between the reactants and achieve a significant number of fusion reactions. This requirement is commonly expressed by a figure of merit called *triple product*. The triple product is a multiplication of three parameters $nT\tau_E$, where n is the particle density, T is the temperature and τ_E is the energy confinement time that measures the rate at which the system loses energy. When the product of these three parameters is above a threshold, fusion reactions will produce more power than it is needed to sustain them, releasing net energy. This threshold depends on the type of nuclear reaction taken into consideration and it varies as a function of the system temperature. For DT reactions the triple product presents a minimum at $T = 14$ keV which corresponds to approximately 162 MK, i.e. approximately 10 times the temperature at the Sun's core. At such high temperatures, the reactants are in a plasma state. The triple product condition for the DT reaction takes this form near its minimum:

$$n\,T\,\tau_E \geq 3 \cdot 10^{21} \left[\frac{keV s}{m^3}\right] \tag{1.1}$$

Maximising all three plasma parameters in 1.1 at the same time is extremely hard to achieve. Most of the current techniques focus on boosting either the reactants density or the energy confinement time while operating at high temperatures, close to the triple product minimum. This approach gives rise to the two primary branches of fusion research: inertial confinement fusion (ICF) and magnetic confinement fusion (MCF). In ICF high densities and temperatures are achieved by compressing a frozen pellet containing the DT mixture using high energy lasers up to 1 MJ. On the other hand, MCF aims to achieve a sufficiently high triple product by confining the plasma using magnetic fields. In this approach, high temperatures and high τ_e are achieved at lower plasma densities.

Achieving controlled thermonuclear fusion is hard. From the first experiments in the early '50s, several device concepts were tested and many scientific and technological discoveries were made. Today MCF is considered to be the most mature and promising approach to nuclear fusion. The leading reactor design in MCF is the *tokamak*, that has proven throughout the years to outperform its competitors. The tokamak JET (Joint European Torus) currently holds the record for the amount of fusion power generated by achieving a total of 16 MW output with 24 MW of auxiliary heating, i.e. producing approximately 66% of the input power [3].

A new generation of large scale tokamaks is currently being built across the globe. These massive devices are expected to prove the feasibility of nuclear fusion as a large-scale and carbon-free source of energy. The largest and most ambitious of them all is the international experimental reactor ITER, currently under construction in France. ITER is an international scientific and technical effort by the world's leading countries to build the largest experimental reactor ever constructed. The main objectives of ITER are the demonstration of the feasibility of thermonuclear fusion as a viable commercial source of energy, the production of a DT burning plasma, the testing of technologies needed for a fusion power plant, the demonstration of tritium breeding from lithium blankets and the showcase of the safety characteristics of a fusion device. ITER will generate a ten-fold return on energy, producing 500 MW of fusion power from 50 MW of input power. The success of ITER will pave the way to a new experimental commercial reactor called DEMO, which is expected to be built by 2050.

1.2 The Tokamak

The tokamak is currently the most promising design for magnetic confinement fusion devices. In a tokamak plasma is confined in a torus shape by magnetic fields. The principal toroidal magnetic field is generated by external magnetic coils. In JET these coils are made of copper. To achieve the strong magnetic fields, of the order of several teslas, needed for plasma confinement, currents of several tens of kiloampere must be fed into these coils. As a result, the operational time of non-superconducting tokamaks is limited by Joule heating to a few seconds. To overcome this limitation, ITER will adopt niobium-tin superconducting coils that will allow both for stronger magnetic fields and longer operational times.

The toroidal magnetic field alone is not sufficient to prevent charge particle loss. A poloidal magnetic field is also necessary to prevent a net particle drift towards the machine vessel. In a tokamak this poloidal field is mainly produced by a toroidal internal current, induced into the plasma by a central solenoid that acts as a transformer. At JET this toroidal current reaches few megaamperes. In large-sized tokamaks, such as ITER, the plasma current will approach 15 MA. A detailed and more exhaustive description of tokamaks can be found in [4].

A large quantity of energy is stored in the creation of the tokamak poloidal magnetic field. JET poloidal field energy is approximately 11 MJ while ITER will reach 395 MJ [5]. These large quantities are comparable to the plasma thermal energy ($\approx$ 12 MJ for JET and $\approx$ 353 MJ for ITER). When confinement is lost during an adverse event, this large amount of energy must be transferred back both into the plasma and into the nearby conducting surfaces, potentially causing stress and damage to the machine.

1.3 Disruptions and Runaway Electrons

Tokamaks can be subject to sudden losses of plasma confinement. During these *disruptions* the thermal and magnetic energies stored inside the plasma can be rapidly redistributed to the tokamak vessel, potentially causing severe damage. For this reason, disruptions are serious adverse events and active strategies are adopted to predict and avoid their insurgence. Unfortunately, the efficiency of these prevention techniques is not yet sufficiently high to avoid the risk of substantial damage.

The most serious cause of disruption in tokamaks is the insurgence of rapidly growing magnetohydrodynamical instabilities. As a result of these events, large portions of plasma thermal energy can be lost in few a hundreds of microseconds. This phase is often called *thermal quench* due to the sharp drop in the plasma temperature. Usually, following the thermal quench phase of the disruption, the plasma current profile flattens and, to conserve flux, a rapid current increase (in the order of 10% of the pre-disruption plasma current) and a large transient negative loop voltage are observed. After the temperature drop, plasma resistivity increases drastically and causes rapid decay of the plasma current. This phase is often called *current quench*. Due to the finite plasma inductance, a rapid change in the current could give rise to a significant in-plasma toroidal electric field.

In some cases, this internal electric field can generate an accelerating force higher than the collisional frictional force experienced by the plasma electrons. These electrons are then rapidly accelerated to relativistic energies in excess of 10 MeV and become *runaway electrons*. At these energies Coulomb collisions with the bulk plasma are negligible and acceleration is predominantly limited by relativistic effects and radiative losses. As a result, a large portion of the pre-disruption current can be efficiently converted into runaway current. This conversion value can reach up to 70% for large tokamaks.

After the eventual decay of magnetic confinement, the generated runaway beam impacts on the plasma-facing components of the vessel in a localized region. The amount of energy deposited in such a localized area may cause metal vaporization, heating shock damage, recrystallization and crack development. Since the amount of damage is proportional to the impinging runaway current, this problem is much more severe for the new generation of large-sized tokamaks, such as ITER, where high plasma currents near 15 MA can give rise to runaway currents larger than 10 MA.

In the ITER tokamak, major relativistic-electron incidents could cause severe damage that would require months to repair. To ensure the success of the ITER mission the insurgence of these events should be separated by years and occur in the order once in a thousand shots. Prediction, avoidance and mitigation techniques are therefore an essential cornerstone to the success of the next step in magnetically confined fusion.

Chapter 2

Runaway Electrons

2.1 Overview

2.1.1 Elementary Processes

A charged particle moving through a plasma experiences a friction force that acts antiparallel to its velocity. The magnitude of this force varies as a function of the particle velocity v, where v is normalized by the thermal velocity of the background distribution. At $v \ll 1$ the drag experienced by the particle increases linearly in v. In this *resistive regime*, when the particle velocity increases due to the presence of a constant external accelerating force, so also does the drag force acting on the particle itself. The magnitude of the frictional force will eventually match the magnitude of the external force and prevent any further acceleration.

In plasmas, particle collision frequency scales as v^{-3}. Therefore, supra-thermal particles experience far less collisional drag than thermal ones. As a result of this effect, in the classical limit, for particles with $v \gg 1$ the frictional force scales as v^{-2}. In this limit, if a constant external force is applied to a sufficiently fast particle the experienced frictional drag decreases as the particle gains velocity. In this *runaway regime* the particle is continuously accelerated and reaches relativistic energies.

Figure 2.1 shows a schematic representation of the frictional force experienced by an electron moving through a plasma in both the classical and relativistic limit.

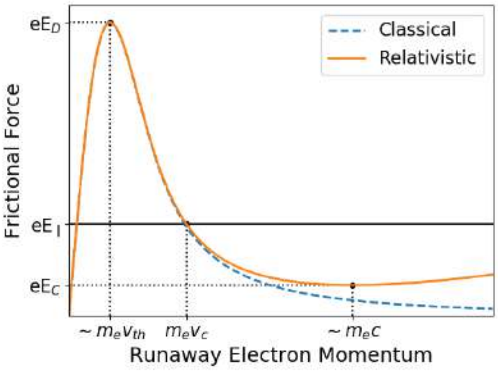

FIGURE 2.1: A schematic representation of the frictional force experienced by an electron in a plasma.

As shown in figure 2.1, the rapidly diminishing collisional frequency limits the maximum drag force a moving electron can experience in a plasma. This maximum is reached near the electron thermal speed v_{th}. If an external force grater than this value is applied to a plasma the entire electron population will be accelerated to relativistic energies and become runaway electrons.

As discussed in section 1.3, in a disruption this accelerating force $eE_{\parallel}$ can be provided by the toroidal electric field $E_{\parallel}$ generated during the current quench phase. The toroidal electric field needed to accelerate the entire electron population into the runaway regime is called *Dreicer field* E_D [6, 7]:

$$E_D = \frac{1}{4\pi\epsilon_0^2}\frac{n_e e^3 \ln\Lambda}{m_e v_{th}^2} \tag{2.1}$$

where ϵ_0 is the vacuum permittivity, n_e is the electron density, e is the electron charge, $\ln\Lambda$ is the Coulomb logarithm, m_e is the electron rest mass and v_{th} is the electron thermal velocity.

If the magnitude of the toroidal electric field $E_{\parallel}$ is less intense than the Dreicer field, only electrons possessing a velocity $v > v_C$ can become runaways. The critical velocity v_C is the value at which the frictional force magnitude equals the accelerating force magnitude, with $v_C > v_{th}$.

In the classical limit, the frictional force experienced by a runaway electron goes to zero as v approaches infinity. This means that for every non-zero toroidal electric field $E_{\parallel}$ there will be a finite critical velocity v_C and therefore, under these conditions, a population of runaway electrons could be always generated from the initial electron population with $v > v_C$. In reality, this is not the case. If relativistic corrections are introduced, we find that the frictional force does not approach zero in the high-velocity limit [8]. Moreover, the frictional force in the high energy range is characterized by the presence of a local minimum, as shown in figure 2.1. This minimum represents the lowest frictional force acting at every time on a high energy electron. As a consequence, there is a minimum value the toroidal electric field must assume in order to overcome the frictional force and generate runaway electrons. This value is generally called *critical field* E_C

$$E_C = \frac{1}{4\pi\epsilon_0^2}\frac{n_e e^3 \ln\Lambda}{m_e c^2} \approx 0.075\, n_e \tag{2.2}$$

where c is the speed of light in vacuum. E_C is approximately proportional to the background plasma electron density n_e. In the last part of equation 2.2 if n_e is expressed in units of $10^{20}/\mathrm{m}^3$, the resulting critical electric field has units of V/m [1].

In addition to collisional drag and relativistic effects, radiative losses contribute to slow down the accelerating runaway electron. There are two main sources of radiative losses for fusion relevant runaway electrons: synchrotron radiation and bremsstrahlung emission. Synchrotron radiation is emitted by the runaway electron beam as it moves around the toroidal magnetic field. Bremsstrahlung is emitted when runaway electrons collide with the background plasma and with the plasma-facing components in the vessel.

The effect of radiation losses is to limit the energy runaway electrons can reach throughout their acceleration and to effectively increase the value of the critical field E_C necessary to generate runaway electrons by several times [9]. These effects can be appreciated in the test particle model presented in section 6.2.2.

2.1.2 Primary Runaway Electron Generation

There are several mechanisms that can generate primary runaway electrons in a tokamak [10]. Here, a list of the most common is presented.

When the toroidal electric field $E_{\|}$ is less intense than the Dreicer field E_D (but strong enough to generate runaway electrons) only a small fraction of the total population is promptly accelerated. This fraction corresponds to the supra-thermal electrons with velocities greater than the critical velocity v_C. Collisions can push electrons that initially did not run away above the critical threshold and produce new runaway electrons. This diffusive source is called *Dreicer mechanism*.

Another common source is the *Hot-Tail*. This mechanism is caused by the lower collisionality of energetic electrons. During a sufficiently fast thermal quench, a partial thermalization of the electron velocity distribution can occur since low energy electrons slow down faster than the high energy ones. The surviving high energy component (hot-tail) of the electron velocity distribution is prone to running away. This mechanism is particularly relevant when gas is injected into the plasma. During this operation, two distinct electron population are created: a hot population derived from the plasma electrons and a cold electron population from the ionization of the injected gas. If a disruption is triggered by the gas injection, the hot population tends to survive the thermal quench phase and becomes a primary seed for runaway generation.

Hot-Tail and Dreicer mechanisms are the most efficient runaway electron seeding sources, but they are not the only ones. In a DT reactor, tritium represents half of the fuel mixture. Tritium is a β^- emitter with a half-life of approximately 12.32 years. The electron generated by the decay has an average energy of 5.7 keV and can reach energies in excess of 18 keV. These energetic electrons could represent a source of primary runaway electrons.

The last source of primary runaway electrons is Compton scattering. Fusion reactors are subject to a large neutron flux produced by nuclear reactions. Under this neutron bombardment, many components of the reactor can become radioactive and emit γ-rays in the MeV energy range. These energetic photons could accelerate thermal plasma electrons above the energy threshold and generate runaway electrons.

2.1.3 Secondary Runaway Electron Generation

The most dangerous runaway generation mechanism for large-scale tokamaks is the *avalanche* generation [11]. In this process, a primary runaway electron collides with a thermal electron in the plasma bulk and transfers enough energy to make it run away. This process leads to a fast exponential growth of the runaway population.

This generation mechanism is dominant in large scale tokamaks. In ITER the avalanche process can multiply the number of relativistic electrons by about twelve orders of magnitude more than in JET [5]. This allows for an efficient conversion of the initial plasma current to runaway electron current, creating a severe threat for potential damage.

2.1.4 Mitigation Techniques

Given the potential threat posed by runaway electron formation to large-scale high-current tokamaks like ITER, a significant effort is placed in developing prediction and avoidance strategies. When these techniques fail, a runaway beam is created. The last defence against possible damage is represented by mitigation techniques. These procedures aim to limit the amount of energy the runaway beam can acquire and therefore lessen the potential damage to the reactor.

Several mitigation strategies are currently being investigated. In the *massive gas injection* (MGI) technique a very large quantity of gas is introduced into the post-disruption plasma [12, 13, 14, 15, 16]. The aim is to increase the electron density in the background plasma and consequently the critical electric field threshold E_C and the critical velocity v_C needed for runaway generation. Moreover, the larger quantity of background target ions will increase the radiation losses, helping limit the runaway beam energy. High-Z materials, such as argon, neon or krypton, are the optimal quenching gasses. They provide a high number of electrons per atom injected and their high-Z largely boosts bremsstrahlung emission. Unfortunately, a complete removal of these gasses from the vacuum vessel after the mitigation can be difficult and can stress the reactor vacuum system. The remaining quantity of these highly radiative impurities can pollute the machine and render subsequent operations more difficult. For this reason, low-Z materials, such as deuterium itself, are also being investigated for runaway electron mitigation.

In a MGI a large quantity of gas is puffed into the background plasma. The gas penetration is sufficient for small and medium-sized tokamak but it is believed that would scale for tokamaks of the size of ITER. A poor gas mixing efficiency will prevent the injected material to reach the inner part of the background plasma and quench the runaway electron formation. The *shatter pellet injection* (SPI) technique was designed to allow deep penetration of the injected material into the background plasma core. SPI launches a solid cryogenic pellet of the target material directly into the background plasma core using a pneumatic system [17, 18, 19]. The pellet is shattered right before entering the vacuum vessel to increase the assimilation of the fragments and to avoid damage to the in-vessel components. Once the material reaches the plasma, it evaporates and mixes into the background plasma. This mitigation technique is currently the primary injection scheme for the ITER Disruption Mitigation System [20].

The last mitigation technique is the *resonant magnetic perturbation* (RMP) [21, 22, 23, 24]. In this scheme, resonant perturbations are applied to the post-disruption magnetic field. The intent of this technique is to help break the remaining close magnetic surfaces and prevent their reformation. Each time a runaway electron completes a full loop of the vacuum vessel its energy increases by eV_{loop}. A fast degradation of the magnetic confinement limits the energy acquired by primary runaway electrons and the creation of secondary electrons.

2.2 Bremsstrahlung Emission

Bremsstrahlung radiation is emitted when a runaway electron is deflected by a plasma ion. The kinetic energy lost in the impact is conserved by the emission of radiation. A complete quantum mechanical bremsstrahlung model was first developed by Bethe and Heitler [25]. Quantum corrections are included in a multiplication factor called Gaunt factor g that multiplies the classical formulation of bremsstrahlung. The bremsstrahlung power emitted per unit volume and unit wavelength can be expressed as [26]:

$$dP = 6.01 \cdot 10^{-30} \frac{g\, n_e^2\, Z_{eff}}{\sqrt{T_e} \lambda^2} \exp\left(-\frac{12.40}{T_e\, \lambda}\right) dV d\lambda \, \left[\frac{W}{cm^3 A}\right] \tag{2.3}$$

where g is the Gaunt factor, n_e and n_i are respectively the electron and ion densities in cm^{-3}, Z_i is the ion electric charge, T_e is the electron temperature in keV and λ is the emission wavelength in Å. Z_{eff} is the plasma effective charge defined as

$$Z_{eff} = \frac{\sum(n_i Z_i^2)}{n_e}$$

where the summation is taken over all the ion species present in the post-disruption plasma.

From equation 2.3 it is clear that high-Z impurities cause a significantly larger emission of bremsstrahlung than low-Z target ions. As discussed in 2.1.4 high-Z elements such as neon, argon ad krypton are often used during runaway electron mitigation. High-Z gas injection is also often adopted to intentionally generate the initial disruption in runaway electron experiments.

Runaway electrons are relativistic particles that can be accelerated to energies of several MeVs. As a result, the bremsstrahlung radiation emitted by the interaction of these relativistic particles with the background plasma can also reach several MeVs.

Since the energy of the emitted bremsstrahlung photon depends on the energy lost during the collision, the bremsstrahlung spectrum generated by a monoenergetic runaway beam is a continuum where the energy of the emitted photon E_{ph} is less or equal than the energy of the incident runaway electron E_{RE}. An example of the bremsstrahlung spectrum generated by a monoenergetic runaway electron beam can be appreciated in figure 5.2 (A).

At these relativistic energies, the bremsstrahlung emission is highly anisotropic. The angular distribution of the emitted photons is largely pinched in a narrow forward cone with an opening angle of $\sim \gamma^{-1}$, where γ is the runaway electron Lorentz factor. Figure 2.2 represents the probability of bremsstrahlung emission as a function of the emission angle in respect to the electron velocity in the rest frame of the particle at varies electron energies. As the energy of the electron increases, so also does the anisotropy in the bremsstrahlung emission. For runaway electrons of energies > 1 MeV the bremsstrahlung emission is predominantly emitted in a forward direction.

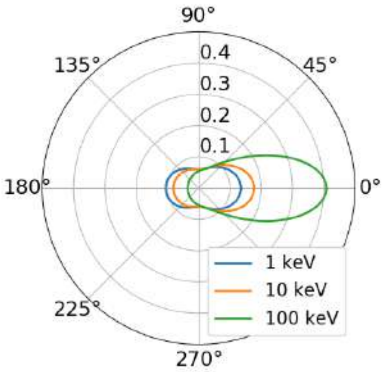

FIGURE 2.2: Normalized probability of relativistic bremsstrahlung emission as a function of the emission angle.

Chapter 5 presents analysis techniques used to recover the runaway electron distribution function from the bremsstrahlung radiation emitted during the interaction with the post-disruption plasma. In particular, section 5.2.1 presents the bremsstrahlung model that was adopted to achieve this result. Moreover, deconvolution techniques, such as Tikhonov regularization are employed to reconstruct the runaway electron energy distribution function from the HXR measured spectra.

2.2.1 Measurement of the RE Bremsstrahlung Radiation

The measurement of runaway electron bremsstrahlung emission is challenging. This radiation covers a wide energy interval up to several MeV, reaching the hard X-ray range. Moreover, runaway electron bremsstrahlung generated in medium and large-sized tokamaks is characterized by severe HXR fluxes, as will be presented in chapters 3 and 4. Runaway electron bremsstrahlung radiation fluxes can easily exceed 10^6 phs/cm^2 s even at several meters from the tokamak.

Bremsstrahlung radiation emitted by relativistic particles is strongly anisotropic. Due to the narrow forward emission cone, detectors placed along a tangential line of sight will experience a significantly larger HXR flux from the incoming runaway electrons than detectors positioned along a radial view line.

Finally, runaway bremsstrahlung emission can quickly evolve on the timescale of a ms. Very fast detectors are needed to successfully characterize this fast-evolving emission and to withstand the severe HXR fluxes.

In addition to the challenges posed by the runaway electron bremsstrahlung radiation, there are a couple of additional complications introduced by the measurement environment. Strong background radiation is usually present in tokamaks. This background radiation is both caused by the γ-ray emitted by the neutron activated materials and by indirect radiation that reaches the detector after one or multiple Compton scattering events.

Moreover, the intense magnetic fields present in tokamaks can interfere with the correct operation of the HXR spectrometer, as discussed in section 4.1.3. Adequate action must be taken to shield the spectrometers from both of these effects.

In this thesis, the development, characterization and deployment of novel hard X-ray spectrometers [27] optimized for runaway electron bremsstrahlung measurement is presented. Optimized diagnostics are needed to fulfil the strict requirements both posed by the challenging nature of the runaway electron bremsstrahlung radiation and by the harsh measurement environment of a tokamak.

Part II

HXR Detector Development

Chapter 3

Detector Development at DIII-D

3.1 LYSO:Ce Detector

3.1.1 Detector Overview

The DIII-D Gamma Ray Imager (GRI), although successful in characterizing the RE radiation in particular low counting rate scenarios [28], was unable to reliably measure during RE discharges without deuterium purging. The main limitation of the system is in its detector array. The GRI HXR detectors are made by BGO scintillator crystals coupled with a PIN diode. A few of them were recently coupled with a SiPM to improve the detector performance. In general, the detector response is too slow to cope with the extreme HXR fluxes of a common RE discharge. As a result, the GRI system reached saturation during not quenched RE discharges and HXR measurement was prevented.

In this chapter, we present the development of a prototype for the GRI detector upgrade. The idea is to replace the existing BGO detectors. This poses several constraints on the design: the detector position in relation to the tokamak, the detector line of sight and the detector maximum dimensions are fixed.

The first compact detector prototypes tested at DIII-D were based on a cerium doped lutetium-yttrium oxyorthosilicate (LYSO:Ce) scintillator crystal coupled with a SiPM. Two different schemes of electronic circuit were developed for shaping the analog output signal of the SiPM. The first one is a zero-pole cancellation circuit made exclusively of passive components, largely based on the one used for the Gamma Ray Camera at JET [29]. The second one is an active readout base that performs the zero-pole cancellation shaping as the passive readout base, but also includes an amplification stage (2X or 5X), a temperature sensor and capability to perform on-line temperature gain compensation.

The two LYSO:Ce prototypes achieved a wide dynamic range for HXR spectroscopy up to 25 MeV with moderate energy non-linearity (see subsection 3.1.4) up to 10 MeV and an energy non-linearity of 50% at 25 MeV. The system energy resolution is approximately 9% at 661.7 keV that extrapolates to few % in the MeV range. The detector fast signals (pulse duration of approximately 150 ns) allow for operation under high HXR counting rate up to 1 MCps.

The work on the LYSO:Ce prototype was presented at the 22nd Topical Conference on High-Temperature Plasma Diagnostics (HTPD 2018). A paper on the technical details of the LYSO:Ce prototype development and its initial performance was also published [30]. A copy of this paper can be found in part IV of this thesis. The development of this prototype was also the topic of a MS thesis [31].

3.1.2 Scintillation Crystal

The first DIII-D prototypes mount a cerium doped lutetium-yttrium oxyorthosilicate (LYSO:Ce) scintillator crystal [32]. LYSO:Ce is a fast inorganic scintillator most widely used today in PET detectors [33]. LYSO:Ce possesses very good scintillation qualities such as good light yield, fast decay time, high density and high Z_{eff} which allows for high HXR detection efficiency. Most relevant characteristics are summarized in table 3.1 and compared with the BGO scintillation properties. LYSO:Ce faster decay time and other scintillation properties make this material more suitable for measuring the RE bremsstrahlung radiation than BGO.

Scintillation Material	Density [gr/cm^3]	Z_{eff}	Decay Time [ns]	Light Yield [phs/keV]	$\lambda_{em,max}$ [nm]
BGO	7.13	71.5	300	9	480
LYSO:Ce	7.1	62.3	36	33.2	420

TABLE 3.1: A brief comparison of the most relevant scintillation properties of bismuth germanate and cerium doped lutetium-yttrium oxyorthosilicate. The reported values are taken from [34, 35]

.

As presented in subsection 2.2.1, the radiation we are trying to measure is characterized by a very high flux emission. The existing geometry of the GRI restricts the new detector prototype to be positioned along a tangential view line and very close to the tokamak magnetic axis. This is an unfavourable position for measuring the RE bremsstrahlung emission. Relativistic bremsstrahlung emission is highly anisotropic and it is mostly emitted in the direction of the RE velocity. The great majority of runaway electrons have passing orbits. The GRI is positioned to look directly at the incoming RE beam. The combination of all of these factors makes the counting rate at the position of the GRI extremely high. As a consequence, BGO detectors reached complete saturation during unquenched RE shots. To sustain this extreme rate it is crucial to have very fast HXR signals. To generate these rapid signals a very fast scintillator needs to be coupled with a fast light collection device, such as a photomultiplier tube or a silicon photomultiplier. LYSO:Ce primary scintillation decay time is approximately 36 ns, almost one order of magnitude faster than BGO. More information on the typical pulse duration for REGARDS is presented in the next section (3.1.3) and in figure 3.3 while a comparison with the BGO detectors can be found in 3.1.6.

LYSO:Ce has a high Z_{eff}. This property increases the overall stopping power of the crystal and promotes photoelectric and pair production processes, where the full energy of the HXR is deposited inside of the crystal, over Compton scattering resulting in a high peak to Compton ratio. LYSO:Ce has a good light yield of approximately 33.2 photons/keV. The manufacturer quotes an energy resolution of approximately 8 % at 662 keV measured with a 1 cm^3 crystal [35]. On the other hand, achieving high energy resolution is not a major priority for this application since the bremsstrahlung radiation is characterized by a continuous spectrum.

Lutetium-yttrium oxyorthosilicate naturally contains ^{176}Lu, a β^- emitter. ^{176}Lu has a natural abundance of 2.6% [36]. ^{176}Lu decays to ^{176}Hf by a β^- decay followed by 3 gamma-ray cascade of 307, 202 and 88 keV [36]. The branching ratio of this nuclear decay is 99.66 %. There is a small 0.34 % that the initial β^- decay is followed by a 4 gamma-ray cascade of 401. 307, 202 and 88 keV. The self-absorption of this radiation gives rise to the LYSO:Ce intrinsic radioactive background. This background can be appreciated in figure 3.1. In the spectrum are visible the gamma-ray sum peaks and the β^- continuum. Most prominent is the 88 + 202 + 307 keV sum peak that occurs at 597 keV. The manufacturer quotes an expected background count rate of 39 cps/g [37]. This corresponds to approximately 2340 cps for a 13 x 13 x 50 mm^3 rectangular parallelepiped crystal and therefore it is negligible when compared with the high HXR fluxes measured during a RE experiment. The LYSO:Ce background radiation is limited to low energy region of the measured HXR spectra that is of less interest for the reconstruction of the runaway electron distribution function. Furthermore, the intrinsic radiation can be potentially used to check the detector calibration during operation without the presence of external radioactive sources.

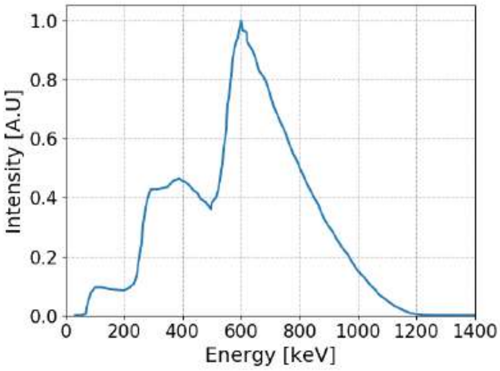

FIGURE 3.1: The intrinsic background of the LYSO:Ce crystal. The 88 + 202 + 307 keV sum peak is clearly visible at 597 keV. Reproduced from [35].

The LYSO crystal dimensions were based on the existing GRI detector BGO scintillator [38]. The overall crystal length of 50 mm was maintained while the shape was changed to a 13 x 13 x 50 mm^3 rectangular parallelepiped to better fit the SiPM detection area (a 13 x 13 mm^2 square). The LYSO:Ce crystal was coupled to a Hamamatsu SiPM [39] using optical grease to ensure optimal light collection. A picture of the crystal can be seen in figure 3.2

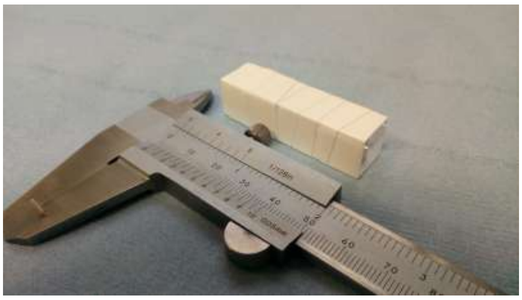

FIGURE 3.2: The LYSO:Ce scintillator crystal used for the DIII-D prototypes. All faces but the one that couples with the SiPM are wrapped in Teflon to increase reflectance and reduce scintillation photon loss.

3.1.3 Silicon Photomultiplier

A silicon photomultiplier array (SiPM) [40] was chosen as scintillation light collection device. This choice was guided by two main constraints posed on the detector design by the already existing GRI structure. The GRI system is made by an array of small detectors tightly packed in a honeycomb structure. The distance between two adjacent detectors is determined by the line of sight geometry of the system. In GRI line of sight are determined by a lead pinhole collimator. The distance between the centres of two line of sight in the honeycomb structure is approximately 2.7 cm. A hard requirement of this project was not to modify the lead collimator. As a result, the new prototype is restricted to have the same compact dimensions of the old BGO detectors. The second constraint is given by the relative position of the GRI in respect to the tokamak. Due to the GRI close proximity to the tokamak magnetic coils and plasma, the detector location is characterized by the presence of strong and variable magnetic fields. These two constraints render the choice of using a photomultiplier tube (PMT) as a photodetector for the LYSO:Ce prototypes impractical. PMT are very susceptible to external magnetic fields, as discussed in detail in section 4.1.3. A very large volume of magnetic shielding material would be required to provide sufficient protection against the external magnetic field making the individual HXR detector very large and not suitable for use in an array configuration, as the GRI requires. SiPMs, on the other hand, are compact devices that are insensible to magnetic fields. These qualities make them the most natural choice for this application.

Silicon PhotoMultipliers (SiPMs) are solid-state photodetectors made by thousands of avalanche photodiodes (APD) connected in parallel and operated in Geiger mode. In addition to being compact devices and to be insensible to magnetic fields, they possess other notable qualities. SiPM can reach high gain in the order of 10^5 -

10^6 (comparable those of PMTs) at a relatively low bias voltage (near 60 V). Moreover, it has been proven that SiPM can sustain the high neutron flux associated with close proximity to tokamaks with little or no permanent damage [41].

The APDs of a SiPM are also commonly referred to as pixels. In a common-bias and common-cathode SiPM matrix ADP pixels connected in parallel. In standard operation, the reverse bias voltage applied to each pixel is higher than its breakdown voltage and therefore each APD cell in a SiPM matrix operates in Geiger-mode. When a scintillation photon reaches the depletion volume of a pixel it can generate an electron-hole pair trough photoelectric effect by promoting an electron from the valence band to the conduction band. The free carriers are then accelerated by the internal electric field at the opposite sides of the PN junction. In Geiger-mode the primary carriers are accelerated enough to generate secondary charge pairs in a self-sustainable avalanche process. This allows the APD to reach very high gains of 10^5 - 10^6 (comparable to the ones generated by PMTs) trough the avalanche process. When an APD operates in Geiger-mode its output signal solely depends on the reverse bias voltage applied to it and it is independent by the initial number of photo-carriers that started the avalanche. In this sense the output of a SiPM pixel is binary. Since the information of the initial number of photo-carriers is lost, the output of a pixel conveys only the information that a signal was detected or not. When a pixel is fired, the APD cell is unable to detect any other photo-carrier for the entire duration of the avalanche. A quenching resistance is introduced in series with the ADP cell to terminate the avalanche process. The avalanche current flowing trough the quenching resistance causes a voltage drop in the bias voltage experienced by the single ADP cell. When the bias voltage drops below the breakdown voltage the avalanche is terminated and the pixel is restored to its ready state. The signal generated by all fired cells is added up in the common-cathode configuration. Therefore the SiPM output signal is proportional to the number of fired cells. SiPM contains thousands of pixels. When the number of scintillation photons reaching the SiPM active surface is small in respect to the total number of the SiPM pixels the probability of one photon impinging on a pixel that is already in the process of being fired is small. In this scenario, the SiPM output is proportional to the number of scintillation photons reaching the SiPM. In subsection 3.1.4 the scenario when this assumption is not valid is explored.

APDs gain declines as temperature increase. The same holds for SiPMs, that are in fact an array of APDs. This decrease in gain is generated by an increase in the breakdown voltage caused by an increase in phonon vibration and thus greater scattering collisions and losses in kinetic energies of avalanching carriers [40]. A common strategy adopted to counter this behaviour is to implement a temperature-compensation circuit that adjusts the applied bias voltage with thetemperature changes to maintain a constant SiPM gain. The variation of the breakdown voltage is in the range of 30 - 50 $\mathrm{mV/C^\circ}$ [31, 39]. In general, for application were no significant temperature change is expected, there is no need for temperature-compensation. A plasma discharge in tokamaks with no superconducting coils lasts a few seconds. The LYSO:Ce prototypes inside of the GRI are sufficiently shielded from the plasma thermal loads and no significant change in temperature caused by the tokamak discharge is expected. On the other hand, detectors are not positioned in a climate-controlled location and therefore ambient temperature can influence the SiPM gain on the scale of hours or days. In this sense, a temperature-compensation system is needed to ensure that data collected in different discharges at very different times are still easily comparable.

A Hamamatsu SiPM (model number S13361-3050-NE04) [39] was chosen for this application. This SiPM has a dimension of 13 x 13 mm^2, well suited for the compactness requirement of this prototype. Few characteristics of this SiPM are shown in table 3.2.

Parameter	Value	Unit
Number of channels	16 (4 x 4)	-
Number of pixels/channel	3584	-
Fill factor	74	%
Spectral response range	320 to 900	nm
Peak sensitivity wavelength	450	nm
Photon detection efficiency	40	%
Gain	1.7 x 10^6	-
Breakdown voltage	53 ± 5	V

TABLE 3.2: Tabulated values are referred to room temperature of 25 ° C and an overvoltage of 3 V. The reported values are taken from [39]

.

If no pulse shaping circuit is applied, the SiPM signal pulse has a long tail with a fall time that can reach 1 μs[42, 43]. This signal is too slow for RE applications where high counting rates are expected. Two components contribute to the duration of the pulse fall time, a fast component given by the scintillator primary decay time and a slow component given by the SiPM characteristic time. The introduction of a pole-zero cancellation circuit allows compensating for the effect of the slow component introduced by the SiPM and reduce the pulse duration. On the other hand, this compensation also attenuates the pulse amplitude. The passive components of the pole-zero cancellation circuit were carefully selected to ensure a short pulse duration without en excessive loss of the pulse amplitude. The signal obtained from the LYSO:Ce crystal coupled with the SiPM and the pole-zero cancellation can be seen in figure 3.3.

The signal obtained is quite fast, with a total duration of approximately 150 ns and a FWHM of approximately 60 ns. The decay time of the pulse is approximately 50 ns. A comparison with the existing BGO detectors is presented in section 3.1.6. Moreover, a comparative test conducted between a LYSO:Ce crystal coupled with

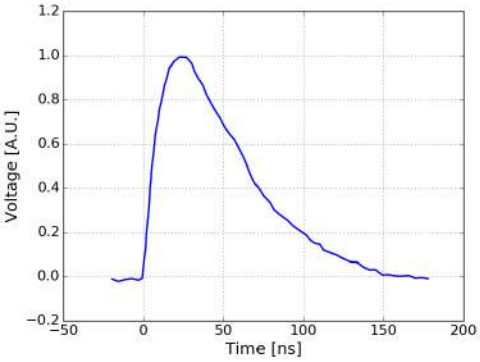

FIGURE 3.3: A typical signal from a LYSO:Ce + SiPM prototype. The pulse has a duration of approximately 150 ns, a FWHM of 60 ns and a decay time of approximately 50 ns.

a PMT model (R9420-100-10 by Hamamatsu) and an identical LYSO:Ce crystal coupled with the SiPM showed that both detectors had comparable energy resolutions when measured with the same acquisition chain [30]. This test proved that no energy resolution was lost by adopting a SiPM instead of a PMT.

3.1.4 Energy Non-Linearity

Linearity, the property by which a detector signal is linearly proportional with the detected HXR energy, is a desirable quality in a spectrometer. Linearity greatly simplifies the interpretation of the measured data. Two factors play a major role in determining a detector linear response: the scintillation crystal linearity, i.e. the property by which a number of scintillation photons are emitted proportionally to the energy of the HXR interacting with the crystal, and the linearity of the photomultiplier, i.e the ability of the light collecting sensor to produce a signal that is directly proportional to the number of scintillation photons detected.

Silicon photomultipliers are intrinsically non-linear photodetectors. This is caused by the finite amount of pixels in a SiPM array and the recovery time a fired pixel takes to discharge and return to a ready state. When a small number of scintillation photons are collected by the matrix they have a high probability to interact with an available pixel. In this scenario the SiPM signal is linear. But when the number of scintillation photon is of the same magnitude of the number of pixels in the SiPM, the probability of one or more of these photons to interact with a pixel that is in recovery time is not negligible. These photons are therefore not detected and do not contribute to the overall SiPM signal. In this scenario, the SiPM response is not linear and the output signal is lower than expected. Since the number of scintillation photons is proportional to the HXR energy, non-linearity is more prominent for energetic HXRs.

A non-linear detector response does not hinder the measurement if its non-linearity is limited and well characterised. If the non-linearity curve is well known it is also possible to correct the deviation during off-line analysis. A dedicated experimental setup was designed to measure this effect. Careful measurement of the LYSO:Ce detector non-linearity was performed to ensure the capability of correcting the detector response in the high energy range, the region of greatest interest for runaway electrons. The measurement procedure is detailed in [31] and the results presented in [30].

An experimental setup was designed to measure the SiPM non-linearity in energy. Two LYSO:Ce detectors were assembled for this purpose. The first detector was a 13 x 13 x 50 mm^3 LYSO:Ce crystal coupled with a SiPM, i.e. the DIII-D prototype, while the second one was made by an identical LYSO:Ce crystal coupled with a PMT (model R9420-100-10 by Hamamatsu [44]). To better distinguish the two detectors, the first one will be addressed as the "SiPM detector" while the second one as the "PMT detector".

SiPM non-linearity becomes more significant at higher energies. In the energy range of common laboratory radioactive sources (< 2 MeV) the SiPM detector was not expected to show noticeable deviation from linearity. To highlight the SiPM non-linearity is necessary to access higher gamma-ray equivalent energies. For this purpose, a blue LED (model NSPB500AS by Nichia [45]) was used to simulate the scintillation light emitted by a LYSO:Ce crystal and was used to illuminate the two photodetectors. The LED was piloted by a pulser (Keysight model 81150A [46]) at a low firing rate (10 kHz). The parameters of the trapezoidal pulse used by the pulser to pilot the LED were finely tuned to best fit the emission of a LYSO:Ce scintillation event. In particular, by changing the amplitude of the pulse it was possible to simulate scintillation events of different equivalent gamma-ray energies and perform a detailed scan of the detectors dynamic range.

The LED source was placed in a dark box to avoid ambient light. The light emitted by the LED was carried out of the light-tight box and split in two using optical fibers. One fiber carried the light to the SiPM, while the other to the PMT. The two detectors were calibrated using radioactive sources, ^{60}Co and ^{137}Cs ($E\gamma$= 1173.2 keV and 1332.5 keV for ^{60}Co and $E\gamma$= 661.7 keV for ^{137}Cs) for the SiPM detector and ^{22}Na ($E\gamma$= 511.0 keV and 1274.5 keV) for the PMT detector. The calibration process is necessary to assign an equivalent energy to LED emission measured by the two detectors. Ideally, once the LED source was turned on both detectors would be exposed to the same amount of light. In reality, the two optical fibers are not exactly identical and so the light fraction to a detector could be higher than to the other. It is possible to correct for this bias introduced by the optical fibers by firing the LED at low voltage. In this situation, the equivalent energy measured by the two detectors is in a region where linearity can be assumed for both of them (< 500 keV). The discrepancy in the LED equivalent energy measured by the two detectors is therefore only caused by a difference in light transmission. In this way, it is possible to compute an optical coefficient that corrects for this discrepancy. Once this coefficient is introduced and the optical difference is accounted for, we can assume both fiber optics branches as identical.

At this point, the LED is fired at increasing higher voltages and the equivalent gamma-ray energy measured by both detector is recorded. Once the optical difference is corrected for, the remaining discrepancy in the equivalent energies measured by the two detectors is only caused by the non-linearity of the SiPM. The results of this measurement are presented in figure 3.4. Non-linearity in figure 3.4(B) is computed as the relative difference between the measured detector response and the ideal behaviour shown by the solid black line in figure 3.4(A).

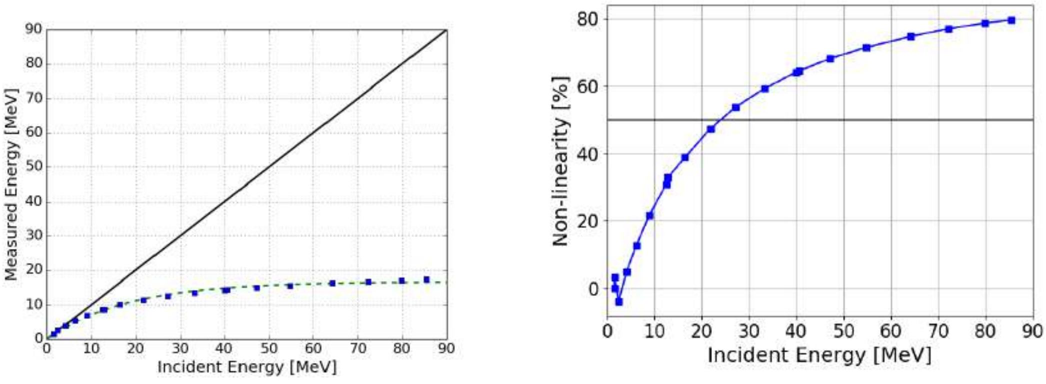

(A) (B)

FIGURE 3.4: SiPM non-linearity. (A) Blue dots represent the equivalent LED energy measured by the SiPM detector plotted against the one by the PMT. The dashed green line is a fit of the measured data. The solid black line indicates the behaviour expected for a perfectly linear system. (B) The SiPM non-linearity as a function of the HXR energy. The black horizontal line indicates a value of 50%.

As expected, the SiPM detector behaviour is linear at low energies and progressively becomes less and less linear as energy increases. At 10 MeV, the non-linearity of the detector is approximately 20% and at 25 MeV is around 50%. We assume this energy as the limit of the SiPM detector energy dynamic range. This dynamic range is more than sufficient to characterize the radiation of a DIII-D runaway electron discharge.

3.1.5 High Rate Non-Linearity

SiPMs are very sensitive to bias voltage fluctuation. A small change in the detector overvoltage substantially modifies the SiPM gain [39, 31]. At high counting rates, the output signal current produced by the SiPM can become significant. This relatively large output current produces a voltage drop in the SiPM overvoltage that causes a reduction in the detector gain. The SiPM gain at high counting rates is strictly decreasing as the output current increases. This effect produces a scaling down of the measured spectrum toward lower energies.

A similar setup to the one described in [47] was used to characterise the detector gain at high counting rates. The measurement procedure is detailed in [31] and the results presented in [30]. The working principle of this measurement is to illuminate the detector with two types of light pulses. The first one is a low frequency, high equivalent energy (3 MeV) LED light pulse that is used as a reference signal. The second type is a high frequency, low equivalent energy (either 600 keV or 1.1 MeV) light pulse that is used as a perturbation. The idea is to simulate, using this second type of pulse, the load on the detector generated by a high counting rate HXR radiation. The LED equivalent energy represents the average energy of the replicated impinging HXR radiation. By using a blue LED (model NSPB500AS by Nichia [45]) and a pulser (Keysight model 81150A [46]) the perturbation signal can be modulated both in its rate and in its equivalent energy. As done for the energy non-linearity tests described in subsection 3.1.4, the pulser parameters were selected to best mock a LYSO:Ce scintillation event.

During these tests, two different equivalent energies were used for the perturbation signal: 600 keV and 1.1 MeV. The perturbation rate was increased up to 1.25 MHz. To avoid any problem generated by the ADC (CAEN model DT5730 [48]) at these high counting rates, the acquisition threshold was placed just above the perturbation signal equivalent energy, so no perturbation pulse would be acquired during the measurement. The reference signal, also generated by an independent LED source, was set at an energy above the ADC threshold, at 3 MeV. In the first segment of the measurement only the reference LED is on. After a few seconds the perturbation LED is also turned on. The generated signal current causes a small drop in the SIPM bias voltage and consequently a gain drop. This is visualized by a shift of the reference peak to the lower energies. By measuring this reference peak shift it is possible to quantify the detector gain shift introduced by the perturbation. The results of these measurements can be appreciated in figure 3.5.

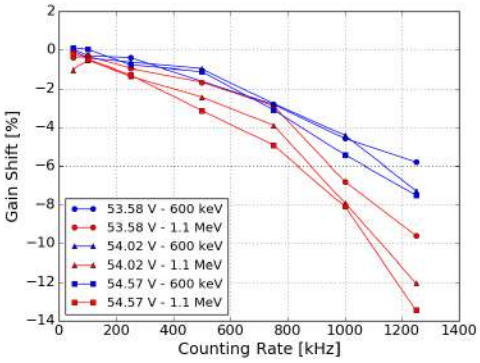

FIGURE 3.5: Detector gain shift caused by high rate perturbation events. Blue markers indicate the gain shift caused by LED events at an equivalent gamma-ray energy of 600 keV, the red ones at 1.1 MeV. Different markers shapes represent the different SiPM bias voltages.

From figure 3.5 we can appreciate that the detector gain is strictly decreasing in a non-linear way as the perturbation increases. By increasing the SiPM bias voltage the shift increases. Moreover, by almost doubling the equivalent energy of the perturbation signals, the detector gain shift increases accordingly. Finally, we can compare the high rate performance of the LYSO:Ce prototypes with one of the GCU detectors [29]. At a perturbation of approximately 600 keV and a rate of 500 kHz, the shift of the reference peak is below 1.5%. This compares favourably with the GCU detectors, that use a $LaBr_3$:Ce crystal coupled with a SiPM [43, 49]. The GCU detector and the LYSO:Ce prototypes mount the same SiPM model and pulse-shaping circuit. This greater stability of the LYSO:Ce prototypes is caused by the lower light yield of the LYSO:Ce crystal when compared to $LaBr_3$:Ce. The LYSO:Ce prototypes fast pulses and limited high rate non-linearity proved to be suitable for high counting rate operation, up to 1 MHz.

3.1.6 Tests at DIII-D

In 2018 the two LYSO:Ce detectors were transported to San Diego for installation at the tokamak DIII-D. One detector was coupled to the active readout base while the other to the passive readout base. Figure 3.6 shows the two detectors assembled with light-tight cases.

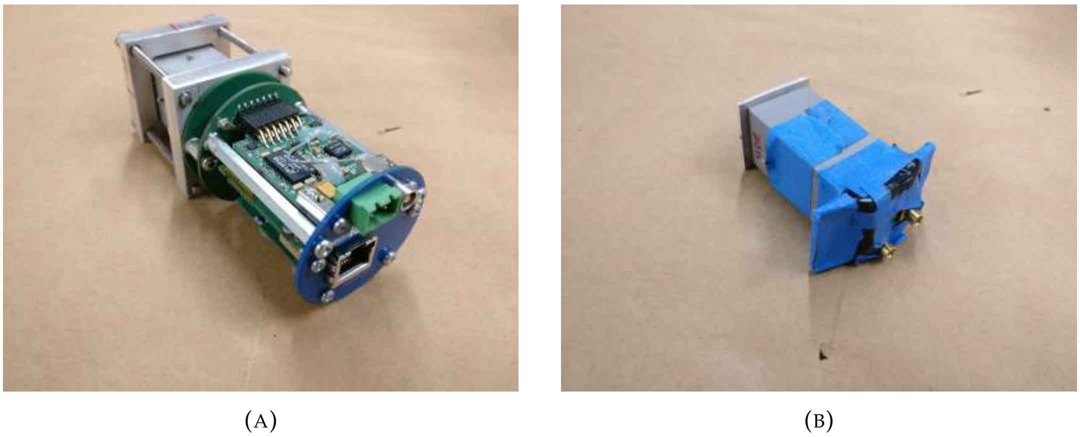
(A)

(B)

FIGURE 3.6: (A) The LYSO:Ce detector coupled with the active readout base. The electronics is visible in the picture front. In the back a light tight aluminum case contains the LYSO:Ce crystal. (B) The LYSO:Ce detector coupled with the passive pole-zero cancellation circuit. The readout board is really compact and only the MCX terminations are visible. The light tight case contains the LYSO:Ce crystal.

Detectors were assembled and tested in the facility laboratory. The tests performed confirmed the good performance of the prototypes. Table 3.3 shows a comparison between the LYSO:Ce detectors and the GRI BGO detectors.

The two LYSO:Ce prototypes are more than 1000 times faster when compared with the standard GRI BGO detector. As a result the LYSO:Ce prototypes can sustain an HXR counting rate 3 orders of magnitude higher than the GRI BGO detector and suffer less pile-up. To achieve fast pulses a pole-zero cancellation circuit is used in both LYSO:Ce detectors. This type of circuit can cause the signal amplitude to diminish. Comparison between the BGO detectors and the LYSO:Ce prototypes

Detector	Signal Amplitude [mV/MeV]	Pulse Decay Time [ns]
BGO + PIN diode	40	60000
BGO + SiPM	60	2000
LYSO:Ce + SiPM	40	50

TABLE 3.3: A comparison between the GRI BGO detectors and the LYSO:Ce prototypes. The new detectors are more than 1000 times faster than existent GRI BGO detectors, proving more suitable for high counting rate operation.

showed a comparable signal amplitude. This is an important characteristic to preserve a healthy signal to noise ratio.

After the laboratory measurements, the LYSO:Ce prototypes were installed inside the GRI along two central lines of sight and tested during RE experiments. To ensure optimal performance, the two LYSO:Ce detectors were encapsulated in light-tight cases. As a result, the two detectors were not small enough to fit in the plastic honeycomb holder of the GRI used to facilitate alignment with the lead pinhole collimator. A custom holder was fashioned to allow the placement of two detectors inside the GRI port. Figure 3.7 presents a picture of the two detectors positioned inside of the GRI port.

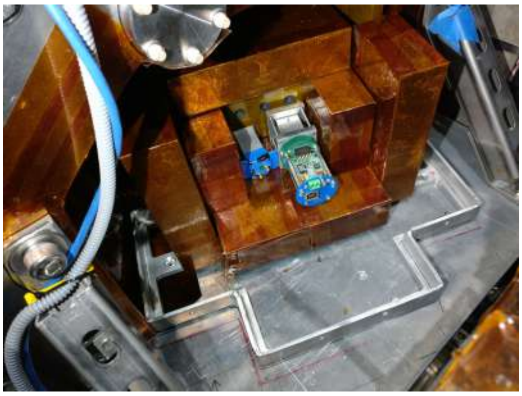

FIGURE 3.7: A picture of the two LYSO:Ce prototypes encapsulated in their light tight cases. The detectors are mounted on a custom holder and position inside of the GRI port. Additional lead bricks are positioned around the detectors to reduce background noise.

During the first RE experiments at the DIII-D tokamak, the LYSO:Ce prototype coupled with the active readout base suffered from a strong noise, that rendered any measurement difficult to interpret. Upon further investigation, it was discovered that the active circuit itself was the cause of this noise. Since the detector worked as intended outside the GRI port, we deem this behaviour caused by the interaction of the active readout base with the severe electrical noise that can be present near a tokamak. On the other hand, the passive readout base performed as expected thorough the experiment, within its technical capabilities.

The geometry of the GRI favours high HXR fluxes. No previous data on the expected flux for a typical RE discharge was available since the existing GRI BGO detectors were too slow and reached saturation almost instantly. The LYSO:Ce prototypes are 1000 times faster and can sustain a counting rate 3 orders of magnitude larger than the BGO detectors, but even the LYSO:Ce prototypes struggled to sustain the extreme HXR counting rate faced during the DIII-D RE discharges.

In figure 3.8 time traces measured by the LYSO:Ce prototype during two DIII-D RE discharges are shown. In the first discharge (#175753) a runaway electron beam is deliberately formed at t = 1.28 s by launching an argon pellet into the plasma. After the RE beam formation, an extreme flux of bremsstrahlung radiation HXR invested the LYSO:Ce prototype. As a result of an extreme level of pile-up, the detector baseline shifted up to +40 mV. In this phase no single LYSO:Ce pulse is identifiable. After the RE current decays the detector recovers the original baseline and pulses generated by the crystal background radiation or by the prompt activation of tokamak components becomes again identifiable. In discharge #175759 the runaway is again triggered by an argon pellet injection at t = 1.2 s. In the early phase of the discharge the LYSO:Ce detector behaves identically as in discharge #175753. The baseline shifts up to +40 mV and no single pulse can be identified. At t = 1.5 s a large amount of deuterium is injected in the machine to flush out the argon gas. This process is called *deuterium purge*. By strongly reducing the plasma Z_{eff} the power radiated by bremsstrahlung strongly decreases. This allowed for a more favourable HXR counting rate and pulses became again individually visible, albeit suffering severe pile-up, after the deuterium purge. Once again, after the RE phase is terminated the detector completely recovers its baseline and pulses return to be individually visible. Two 5 μs enlargement of the detector signal for discharge #175759 are shown in figure 3.9. Figure 3.9 (A) shows the signal at t = 1.3 s, before the deuterium purge, while 3.9 (B) shows the signal at t = 1.8 s, after the purge.

While a full pulse shape analysis is not achievable when excessive pile-up prevents to recover the individual pulse, information of the HXR radiation is not completely lost. In this regime, often called current mode, the output signal of the detector is proportional to the radiation power flux. Moreover, if a deuterium purge is applied to the runaway phase of the discharge it is possible to recover some pulse information e perform a crude pulse shape analysis to gain an estimate of the HXR spectrum.

Even with these limitations, the new LYSO:Ce prototype granted access to previously unavailable information on the RE bremsstrahlung emission and contributed to scientific discoveries at the DIII-D tokamak. Most noticeably, in 2018 the detector allowed to draw a correlation between the RE energy and the insurgence of kinetic instabilities during the current quench phase of a disruption [50] and in 2019 where chirping instabilities were observed modifying the runaway electron distribution function [51].

The measurements performed at DIII-D with the prototype detectors in 2018, although successful, revealed some technical limitations. First of all, the extreme HXR

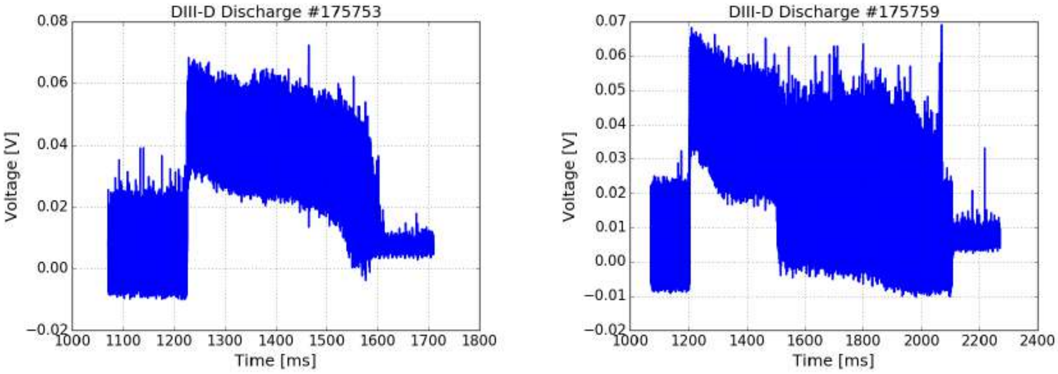

(A) (B)

FIGURE 3.8: Times traces of the prototype signal for two DIII-D RE electron discharges. (A) The RE beam is formed at t = 1.28 s. The severe HXR flux causes the detector baseline to shift up to +40 mV. The baseline recovers only after the RE current decay. (B) The RE beam is generated at t = 1.2 s. Once again, severe HXR flux causes the detector baseline to shift up to +40 mV. At t = 1.5 s a deuterium purge severely reduces the plasma Z_{eff} and consequently the bremsstrahlung flux. After the purge the detector baseline recovers before the RE termination (t = 2.1 s).

flux measured at the GRI location that sometimes exceeded the LYSO:Ce prototype high counting rate capability and in these scenarios prevented the reconstruct of the RE bremsstrahlung spectrum. Another limitation is posed by the detector nonlinearity at high rates. As discussed in section 3.1.5, severe fluxes can modify the gain of the detector making its calibration unreliable. Moreover, the DIII-D GRI location turned out to be not suitable for an active readout base. While the LYSO:Ce proved to be a useful diagnostic even under these technical limitations, a new detector was developed to address these issues. The development of this new compact HXR spectrometer is presented in the next section of this thesis.

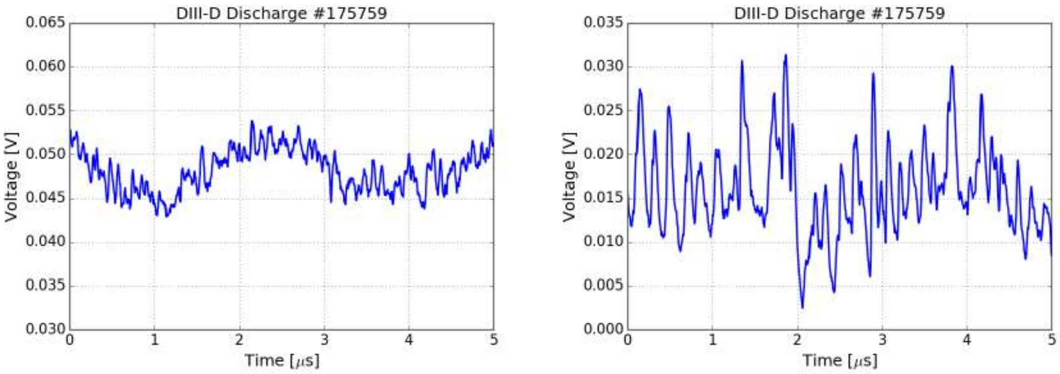

(A)

(B)

FIGURE 3.9: (A) A 5 μs enlargement of the LYSO:Ce signal at t = 1.3 s (before the deuterium purge) for discharge #175759. The signal is almost flat (the oscillation is caused by a low frequency pick up noise in the cables) and no individual pulse is recognizable. (B) A 5 μs enlargement of the LYSO:Ce signal at t = 1.8 s (after the deuterium purge) for discharge #175759. The detector baseline is almost restored. Individual pulses are visible under severe pile-up.

3.2 YAP:Ce Detector

3.2.1 Detector Overview

Several valuable considerations can be made on the LYSO:Ce prototypes performance in 2018 at the tokamak DIII-D. The most important ones can be summarized in this list:

- The LYSO:Ce prototypes were significantly faster than the current GRI BGO detectors. This result was achieved by using a fast scintillator crystal coupled with a fast photodetection device and a pole-zero cancellation circuit. The LYSO:Ce pulse decay time is more than 1000 times shorter than the current BGO spectrometers. This improved the high rate capability of the system by 3 orders of magnitude.
- The GRI location is not suitable for the correct operation of the active readout base. This is probably due to the presence of electromagnetic background noise that interferes with the electronics. On the other hand, the passive readout base had no performance issue and behaved as expected.
- During the DIII-D RE discharges extremely high HXR flux was experienced by the LYSO:Ce prototype. This is caused by the proximity of the GRI system to the plasma and the tangential nature of its line of sights. No previous information on the order of magnitude of the expected HXR flux was available, since the existing detectors saturated in most of the unquenched RE scenarios. The LYSO:Ce prototype, thanks to their high counting rate capability, did not saturate. On the other hand, in the unquenched stage of the RE discharges the LYSO:Ce detector operated in the so-called current mode, where the detector output is proportional to the radiation power flux. In this stage no individual HXR pulses are visible and the HXR spectrum can not be reliably reconstructed. The maximum counting rate experienced in these scenarios is roughly estimated to be greater than 20 MCps. When a deuterium purge is applied to the post-disruption plasma the HXR flux drops drastically. In this scenario, the LYSO:Ce detector is able to measure individual pulses, but severe pile-up still occurs.
- Few elements of the plasma discharge can be adjusted to lower the RE bremsstrahlung radiation flux to the GRI detectors. First of all, the aforementioned deuterium purge can significantly reduce the HXR flux by substantially lowering the plasma Z_{eff}. Moreover, the DIII-D plasma current polarity can be inverted so that the generated RE beam is moving away from the GRI instead of towards it. This should reduce the HXR flux due to the anisotropy in the relativistic bremsstrahlung emission.
- There was no gain monitor system installed with the BGO detectors or LYSO:Ce prototypes. As presented in 3.1.5, high counting rate can produce a substantial

detector gain shift. After the 2018 tests revealed the magnitude of the expected HXR radiation flux the necessity of this system was evident.

- In the end the requirements for a compact detector were relaxed to allow the LYSO:Ce prototypes to use cumbersome light-tight cases, as shown in figure 3.6. For the new DIII-D prototype compactness will be considered a hard requirement in order to preserve the current array GRI geometry in its entirety.

For a more detailed discussion on the development of the LYSO:Ce prototypes and the results of 2018 DIII-D measurements see section 3.1.

By far, the largest issue is presented by the extreme HXR flux at the location of the GRI system during a RE discharge. In the new HXR prototype, this problem is addressed in two independent ways: by redesigning the scintillator crystal and by introducing a tungsten attenuator in front of the spectrometer. The new detector was also designed to be very compact so to respect the strict geometrical requirements of the GRI array system. Learning from our previous experience, the passive configuration of the detector readout base was chosen for this application. In addition, a LED was installed directly into the detector itself to monitor the spectrometer gain during operation.

The new DIII-D spectrometer is based on YAP:Ce scintillator crystal coupled with a SiPM. A picture of the new detector can be appreciated in figure 3.10.

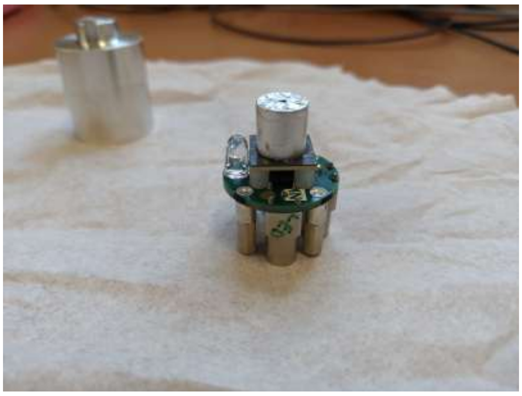

FIGURE 3.10: The new YAP:Ce spectrometer designed for the DIII-D GRI. The scintillator crystal is smaller than in the previous LYSO:Ce prototype. The crystal is wrapped in aluminium foil to reduce the loss of scintillation photons at its edges. The SiPM and the passive readout electronics are visible underneath the crystal. Finally, the LED used for the detector gain monitoring can be spotted at the lest side of the SiPM.

The new spectrometer is very compact. The overall length is just 3 cm and the diameter is 2.7 cm, even more compact than required. To achieve this, the old prototype passive readout base was redesigned. More details on this topic can be appreciated in subsection 3.2.3. The YAP:Ce prototype has a wide dynamic range in excess of 20 MeV with an energy non-linearity of approximately 30% at 10 MeV. The spectrometer energy resolution is approximately 9% at 661.7 keV. The new YAP:Ce detector has an HXR detection efficiency that is almost 8 times lower than the LYSO:Ce prototypes. This quality makes this detector more suitable for this application.

The proposal of this new compact HXR spectrometer for the GRI system upgrade won a research grant from the USA Department of Energy. The test and characterization of this spectrometer was also part of a MS thesis.

3.2.2 Scintillation Crystal

The scintillator crystal redesign is one of the main strategies to mitigate the detector counting rate under severe HXR flux. As presented in section 3.1, the first DIII-D prototype mounted a 13 x 13 x 50 mm^3 LYSO:Ce scintillator crystal. The test performed at DIII-D presented two areas of potential improvement. The first one is the high stopping power of the LYSO:Ce material. For this application, a high stopping power is actually a drawback, since we are trying to reduce the amount of HXR detected. Cerium doped yttrium aluminium perovskite (YAP:Ce) due to its lower density and lower Z_{eff} offers a lower HXR detection efficiency. A comparison between LYSO:Ce and YAP:Ce main scintillation properties are presented in table 3.4. The second area of improvement is the crystal geometry. As presented in subsection 3.1.2, the dimensions of the LYSO:Ce crystals were largely based on the dimensions of the existent BGO detectors. The measurements conducted in 2018 showed the crystal dimensions were larger than necessary. By reducing the crystal dimension it is possible to further reduce the spectrometer detection efficiency.

Scintillation Material	Density [gr/cm^3]	Z_{eff}	Decay Time [ns]	Light Yield [phs/keV]	$\lambda_{em,max}$ [nm]
LYSO:Ce	7.1	62.3	36	33.2	420
YAP:Ce	5.37	31.3	25	25	370

TABLE 3.4: A brief comparison of the most relevant scintillation properties cerium doped lutetium-yttrium oxyorthosilicate and cerium doped yttrium aluminum perovskite. The reported values are taken from [35, 52].

The new DIII-D detector mounts a cylindrical YAP:Ce crystal that measures 1 cm in diameter and 1 cm in length manufactured by Crytur. The reduction in the crystal detection efficiency can be estimated. The first contribution is given by the reduced cross section of the crystal to the HXR beam. LYSO:Ce cross-section is a square of area equal to 169 mm^2 while YAP:Ce circular cross-section is equal 78.5 mm^2. If we assume a uniform spatial distribution of the HXR collimated beam, the new YAP:Ce cross-section intercepts only 46% of the area previously covered by the LYSO:Ce. Moreover the reduction in absorption efficiency from a 5 cm long LYSO:Ce crystal to a 1 cm long YAP:Ce was estimated using MCNP simulations. The YAP:Ce crystal has an absorption efficiency at 1 MeV that is approximately equal to 28% of the LYSO:Ce crystal. These two effects combined bring the overall detector efficiency to less than 13% of the old LYSO:Ce prototype. This corresponds to an almost 8 fold reduction in the expected detector counting rate. As an example the 20 MCps HXR counting rate estimated during the most severe conditions experienced by the LYSO:Ce prototype at DIII-D is expected to be reduced to a more manageable 2.6 MCps HXR rate for the YAP:Ce detector.

YAP:Ce is a fast inorganic scintillator. As can be appreciated form table 3.4, the scintillation decay time is even faster than LYSO:Ce. This was one of the main criteria for selecting the scintillator material. As explained in 3.1.2, a fast scintillator is essential to generate a fast HXR spectrometer that is suitable for this application. More information on the YAP:Ce detector signal duration is presented in subsection 3.2.3.

Cerium doped yttrium aluminium perovskite features two additional properties that are beneficial for this application. A good light yield of about 25 photons/keV, that is sufficiently high to generate strong signals in the SiPM but is also lower than the LYSO:Ce light yield and therefore contributes to lower the energy non-linearity of the YAP:Ce spectrometer induced by the finite amount of pixels in the SiPM. The second effect that is equally beneficial to reduce the SiPM non-linearity is the wavelength of the scintillation emission. At 370 nm, the wavelength at which the maximum YAP:Ce scintillation occurs, the SiPM photon detection efficiency is approximately 28% while at 420 nm, the wavelength for the LYSO:Ce, is approximately 38% [39]. These two effects combined reduce the number of scintillation photons detected per keV to approximately 56% when compared to the old LYSO:Ce prototype. This greatly reduces the YAP:Ce detector energy non-linearity.

YAP:Ce is not hygroscopic and does not have an intrinsic background radiation. The main inconvenience with this scintillator material is the low peak to Compton ratio caused by the relative low Z_{eff}. This property does not preclude the measurement of the RE continuous bremsstrahlung radiation but makes it less straightforward to interpret the measured HXR spectrum.

3.2.3 Silicon Photomultiplier

The YAP:Ce prototype uses the same SiPM model of the LYSO:Ce prototype (Hamamatsu, model S13361-3050-NE04 [39]). For more information on the SiPM specifications see subsection 3.1.3 and table 3.2. In the LYSO:Ce prototypes the SiPM was directly deposited on the same silicon base of the pole-zero cancellation circuit. As shown in figure 3.10, the YAP:Ce prototype SiPM is not directly deposited on the readout base but it is connected to it through a connector (SAMTEC model ST4-20-1.00-L-D-P-TR). The SiPM is therefore placed above the circuit board, saving valuable space for the passive components and making a more compact design possible. Using a SiPM that is not directly deposited on the circuit board also allows installing the temperature sensor directly on its bottom side, making the temperature measurement more accurate. Four plastic pins are installed to mechanically support the SiPM and prevent any bending or twisting of the connector.

Figure 3.11 shows the typical pulse shape for an HXR event detected by the YAP:Ce spectrometer. The pole-zero cancellation circuit is identical to the one used for the LYSO:Ce prototypes. As a result, the pulse timing is very similar to LYSO:Ce detectors. The signal is fast (approximately 150 ns) and allows for high counting rate operation.

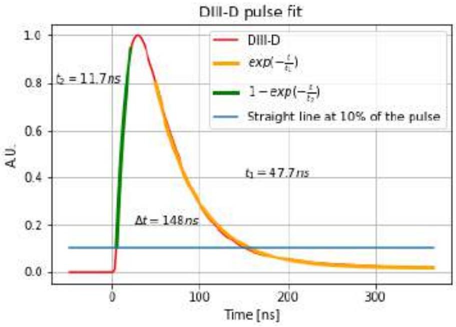

FIGURE 3.11: Typical pulse shape for an HXR event measured by the YAP:Ce spectrometer.

As explained in subsection 3.2.2, the YAP:Ce detector is expected to fire approximately 56 % of the number f pixel an HXR event of the same energy would have triggered in the LYSO:Ce detector. As a consequence, also the signal amplitude measured at a 1 V of overvoltage is approximately half of the one measured for the LYSO:Ce detector. Table 3.5 shows a comparison between the two different prototypes and the BGO detectors.

Detector	Signal Amplitude [mV/MeV]	Pulse Decay Time [ns]
BGO + PIN diode	40	60000
BGO + SiPM	60	2000
LYSO:Ce + SiPM	40	50
YAP:Ce + SiPM	21	50

TABLE 3.5: A comparison between the GRI BGO detectors, the LYSO:Ce prototype and the YAP:Ce spectrometer.

In the event the signal amplitude turns out to be too small and the signal to noise ratio is not optimal it is always possible to increase the amplitude of the detector by increasing the SiPM overvoltage. At 2 V of overvoltage the signal amplitude is approximately 40 mV / MeV.

The YAP:Ce has an energy resolution of approximately 9% at 661.7 keV (^{137}Cs). This is the same energy resolution of the LYSO:Ce prototypes.

3.2.4 Energy Non-Linearity

As detailed in subsection 3.1.4, the SiPM energy non-linearity arises when the number of scintillation photons impinging on the SiPM is comparable with the number of its total pixels. As presented in subsection 3.2.2, due to the lower light yield and different wavelength of emission, the amount of scintillation photons collected by the SiPM of the YAP:Ce detector is expected to be approximately 56% of the one that the LYSO:Ce spectrometer SiPM would have collected for the same HXR. This reduction in the effective number of scintillation photons/keV increases the energy linearity of the SiPM. On the other hand, the smaller crystal reduces the number of pixels available. If a uniform pixel spatial distribution on the active surface of the SiPM is assumed this decrease can be approximated as the ratio between the circular base area of the YAP:Ce crystal and the SiPM surface area. This value is found to be approximately 46%. These two effects have approximately the same magnitude and opposite effects on the YAP:Ce detector energy non-linearity, so they cancel each other. The YAP:Ce prototype is expected to have approximately the same energy non-linearity curve of the LYSO:Ce detector, with possibly a slightly reduced linearity due to the larger effect of the loss of pixels.

The same measurements detailed in subsection 3.1.4 were reproduced with the YAP:Ce prototype. The result of these tests can be seen in figure 3.12.

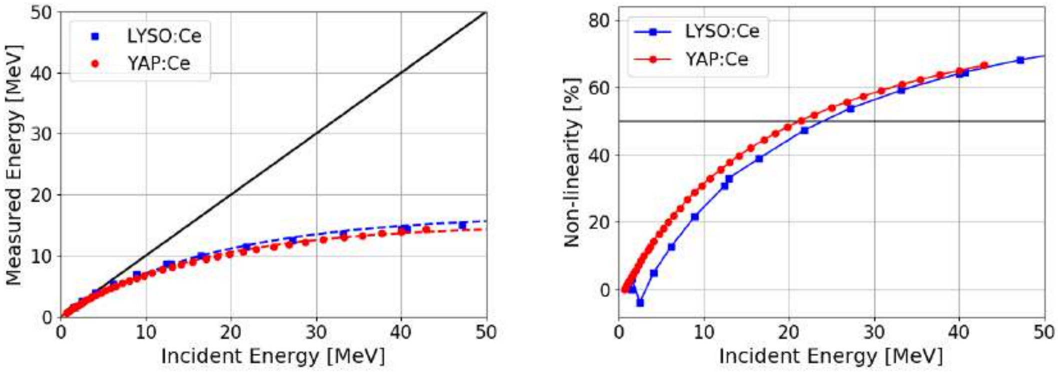

(A)

(B)

FIGURE 3.12: YAP:Ce spectrometer non-linearity. (A) Energy measured by the detector as a function of the incident energy. Blue squares refer to the LYSO:Ce prototypes while red dots represent data collected by the YAP:Ce detector. The dashed lines are fits of the measured data. The solid black line indicates a linear behaviour. (B) The LYSO:Ce (blue squares) and YAP:Ce (red dots) non-linearity as a function of the HXR energy. The black line indicates a value of 50%.

As expected, the YAP:Ce detector energy non-linearity (red) is comparable with the one measured for the LYSO:Ce prototype (blue). At 10 MeV, the non-linearity of the YAP:Ce detector is approximately 31%. At 21.5 MeV the non-linearity reaches 50%. As we did in subsection 3.1.4, we assume this last energy value as the limit of the SiPM detector energy dynamic range. A dynamic range in excess of 20 MeV is more than sufficient for this application.

3.2.5 High Rate Non-Linearity

In subsection 3.1.5 the effect of high signal current on the SiPM gain was discussed. In this particular application, high output current is generally achieved by high HXR counting rates. The design of this detector was guided by the attempt of reducing the HXR counting rate experienced by the spectrometer in the harsh environment of the GRI system without compromising its performance. The strategies adopted to this end are presented in subsection 3.2.2.

YAP:Ce spectrometer high counting rate response was tested using the same procedure detailed in subsection 3.1.5. After 2018 test performed at the DIII-D tokamak the high rate response was investigated with perturbation signals up to 2 MHz. The results of these measurements are presented in figure 3.13.

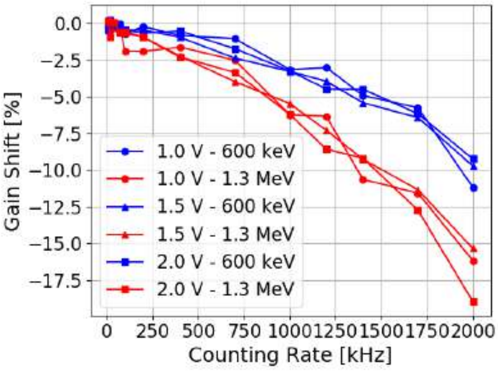

FIGURE 3.13: YAP:Ce detector response under high rate perturbation events. Blue markers indicate the gain shift caused by LED events at an equivalent HXR energy of 600 keV, the red ones at 1.3 MeV. Different marker shapes represent the different SiPM overvoltages.

As for the LYSO:Ce prototypes, the detector gain is strictly decreasing as the rate of perturbation increases and by almost doubling the equivalent energy of the perturbation signals, the detector gain shift increases by the same amount. The high counting rate of the YAP:Ce detector is comparable with the one of the LYSO:Ce prototypes. This makes the YAP:Ce spectrometer suitable for high counting rate operation, in excess of 1 MHz.

By design, the YAP:Ce spectrometer has an HXR detection efficiency almost 8 times lower than the LYSO:Ce prototypes while retaining the same high counting rate capability. For this reason, this novel spectrometer can withstand HRX fluxes almost 1 order of magnitude higher than the previous prototypes. Moreover, by reducing the length of the scintillator by 45 mm, more space in front of the detector is now available and could be used to install a lead or tungsten rod to further attenuate the HXR flux, if needed.

3.2.6 Gain Control System

A gain monitoring system was introduced in the detector design to measure the YAP:Ce spectrometer gain shift caused by high HXR counting rates during a RE discharge. This feature was added in response to the severe HXR flux observed at the DIII-D GRI system in 2018. In these situations, where the spectrometer gain could shift significantly, it is crucial to be able to quantify the magnitude of this effect to ascertain the data quality and to possibly correct for it in off-line analysis.

The gain monitor system is similar to the one adopted for REGARDS (see section 4.1.4) with the exception that in this application the LED is directly embedded inside of the HXR detector. The principle of operation is to intermittently fire the LED at a fixed bias voltage using an electrical pulse generator in order to expose the SiPM to a constant light source. The resulting electrical signal can be used as a reference throughout the discharge. If the SiPM gain shifts during the plasma discharge, under a severe HXR emission, the amplitude of the reference pulse will also shift accordingly. In off-line analysis the LED reference pulses can be isolated using pulse shape discrimination techniques and the YAP:Ce spectrometer gain can be inferred by observing their amplitudes. An example of how this technique is applied in practice can be observed in sections 4.1.5 and 4.1.6.

The YAP:Ce detector gain monitoring system uses a blue light-emitting diode (model NSPB500AS by Nichia [45]) as its constant light source. The LED is visible on the left side of figure 3.10. The LED is directly mounted inside of the light-tight HXR detector aluminium casing. This is a very convenient and compact solution. By contrast, REGARDS uses an external light-tight box to house the LED and an optical fiber to transport the emitted light to the PMT photocathode. This type of solution is not adequate for the YAP:Ce prototype due to the requirement of a compact geometry for array operation. Moreover, using an external light-tight box and one optical fiber for each detector would have made the design less scalable and modular.

As explained in subsection 3.12, the YAP:Ce crystal covers only 46% of the SiPM surface area. The crystal is also wrapped in aluminium foil to increase its reflectance. This wrapping also prevents the LED photons to pass through the YAP:Ce crystal and fire a SiPM pixel under it. In this way, the SiPM area below the crystal is dedicated to the detection of the HXR scintillation photons while the area that is not covered by it remains available to collect the LED signal.

This gain monitoring system is effective if LED pulses are individually visible and can be separated using pulse shape discrimination methods. This technique is an integral part in the HXR counting rate reduction strategy adopted for the YAP:Ce prototype as it would not be able to give information on the detector gain shift if the spectrometer operates in current mode.

Chapter 4

Detector Development at ASDEX Upgrade

4.1 REGARDS

4.1.1 System Overview

The Runaway Electron GAmma-Ray Detection System (REGARDS) is a novel hard X-ray spectrometer developed for RE bremsstrahlung measurement. The system was designed to be easily transported and deployed at different middle-sized tokamak sites and to provide quality data in a variety of measuring conditions. The ability to be easily deployed in different locations was carefully taken into account in the system design.

REGARDS satisfies all the challenging requirements associated with RE bremsstrahlung measurements presented in section 2.2.1. REGARDS provides a wide dynamic range for HXR spectroscopy with an upper energy bound in excess of 20 MeV. The system energy resolution is approximately 3% at 661.7 keV. Moreover, the HXR detector gain is very stable even under severe HXR fluxes, with a gain shift inferior to 3% at 1 MCps HXR counting rate.

Conceptually, we can divide the REGARDS system into three main components: the hard X-ray (HXR) detector, the gain control system and the digital acquisition system. A schematic representation of the REGARDS system can be found in figure 4.1. The blue dotted box encompasses all the elements that are part of the HXR detector. REGARDS HXR detector is constituted by a cerium doped lanthanum bromide ($LaBr_3$:Ce) scintillator crystal coupled with a photomultiplier tube. A desktop HV module provides the bias voltage for the PMT. The gain control system, encircled in the green dotted box in figure 4.1, is used to monitor the detector gain during the runaway discharge. More details on this system are presented in section 4.1.4. Finally, the orange box contains the elements of the fast acquisition system used for data collection.

A paper on the technical details of the REGARDS development and its initial performance was submitted for publishing. A copy of the submitted document can also be found in part IV of this thesis.

In the following sections of this chapter, a review of the REGARDS development and fist deployment in MST1 tokamaks Asdex Upgrade and COMPASS is presented.

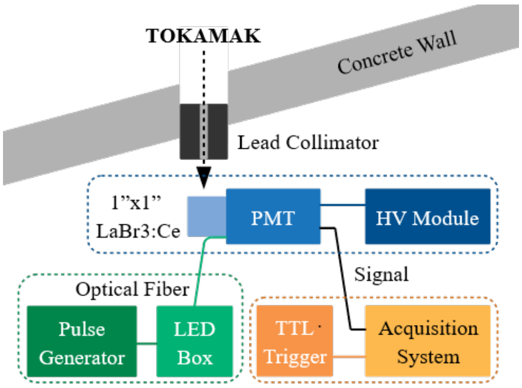

FIGURE 4.1: A schematic representation of the Runaway Electron GAmma-Ray Detection System.

4.1.2 Scintillation Crystal

Cerium doped lanthanum bromide is a fast inorganic scintillator. This material was chosen for the scintillator crystal in REGARDS HXR detector. Lanthanum bromide is a relatively new scintillator crystal [53] but due to its excellent properties has quickly become a common choice for gamma-ray and HXR spectrometers in fusion nuclear devices. For example, currently, the JET large spectrometers and the JET Gamma Camera Upgrade use this type of crystal [43, 29].

This scintillation material offers several qualities that are very useful for measurement of the RE bremsstrahlung radiation. A brief summary of $LaBr_3$:Ce scintillation properties can be found in table 4.1.

Density [gr/cm^3]	Z_{eff}	Decay Time [ns]	Light Yield [phs/keV]	λ_{em} [nm]
5.07	45.3	25	63	380

TABLE 4.1: A brief summary of the most relevant scintillation properties of cerium doped lanthanum bromide. The reported values are taken from [37]

$LaBr_3$:Ce is a fast inorganic scintillator. Its fast primary scintillation decay time is approximately 25 ns. This property, when coupled with a fast light collection device, allows for the very fast signals that are crucial for high counting rate operation, generally associated with RE bremsstrahlung emission. More information on the typical pulse duration for REGARDS is presented in the next section (4.1.3) and in figure 4.4.

Lanthanum bromide has a very high light yield that provides strong scintillation signals and good energy resolution. The manufacturer quotes a $LaBr_3$:Ce energy resolution of approximately 2.9 % at 662 keV. The tests were performed with a 3" x 3" cylindrical crystal [37].

In a lanthanum bromide crystal, intrinsic background radiation caused by the nuclear decay of ^{138}La can be observed. ^{138}La can decay to ^{138}Ba by emitting a gamma-ray of 1436 keV or to ^{138}Cs with the combination of a β^- decay and the emission of a gamma-ray of 798 keV. The decay branching ratios are approximately 66.4% and 33.6% respectively [36]. The background LaBr$_3$:Ce spectrum can be seen in figure 4.2. In the spectrum the 1436 keV peak, the β^- continuum and the 798 keV plus β^- continuum sum peak are visible. ^{138}La has a natural abundance of 0.09% [36]. The manufacturer quotes an expected background count rate of 0.393 cps/cc [37]. This corresponds to approximately 20 cps for a 1" x 1" cylindrical crystal. Due to its low counting rate, LaBr$_3$:Ce background radiation hardly alters the quality of the measured HXR spectra. This holds especially true for very high HXR counting rate applications, like measuring the runaway electron bremsstrahlung, where signals can easily surpass the MCps threshold. Contrarily, this background radiation, and particularly its characteristic 1436 keV peak, can be useful to perform quick detector calibration between plasma shots, that are usually several minutes apart.

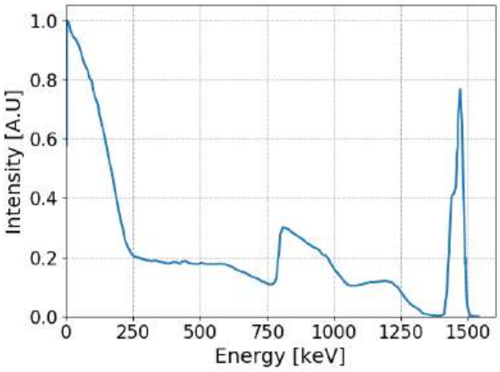

FIGURE 4.2: The LaBr$_3$:Ce intrinsic background. The characteristic 1436 keV peak and the β^- continuum plus 798 keV sum peak are visible. Reproduced from [37].

Finally LaBr$_3$:Ce is characterized by a high Z_{eff}. This characteristic favours photoelectric and pair production processes over Compton scattering. These are the two processes where the full energy of the HXR is deposited inside of the crystal. The high peak to Compton ratio simplifies the interpretation of the measured HXR spectra.

The crystal HXR detection efficiency is primarily a function of the impinging HXR energy and the crystal dimensions. Given the constraints of the expected HXR radiation spectrum and its flux on one hand and of the detector maximum counting rate capability on the other, the scintillator crystal dimensions and the detector collimation have to be selected accordingly.

Initially, a 1.5" x 2" LaBr$_3$:Ce cylindrical crystal was considered for REGARDS. The crystal dimensions were decided based on rough estimates of the HXR radiation expected in a typical AUG RE shot.

A 1.5" x 2" LaBr$_3$:Ce crystal was coupled with a R6231 Hamamatsu PMT [54] and installed at AUG. Preliminary tests were conducted at AUG in December 2018, during the first shots of the MST1 campaign. The measured HXR counting rate during these exploratory pulses was very high (in excess of 2 MCps) and the PMT response at these rates was not satisfactory. The dimensions of the REGARDS $LaBr_3$:Ce were reconsidered based on the data collected during these tests in order to reduce the amount of detected HXRs. A 1" x 1" $LaBr_3$:Ce cylindrical crystal was adopted to allow a reduction in the detector efficiency of about 20% and the PMT was changed to better fit the new crystal dimensions. Tests form February 2019 confirmed the improvement in REGARDS performance.

4.1.3 Photomultiplier Tube

REGARDS scintillator crystal is coupled with a photomultiplier tube (PMT). The role of the PMT is to convert the scintillation events into a proportional electrical signal that can be recorded by the digital acquisition system. Photomultiplier tubes are very linear and reliable devices and they are commonly used in HXR spectroscopy.

The photomultiplier tube principle of operation is the following. A scintillation photon is emitted by the scintillation crystal and impinges on the photocathode layer of the PMT. An electron is extracted from the photocathode by the photoelectric effect. This photoelectron is now focused and accelerated towards an electron multiplication stage by electric fields. The PMT multiplication stage is made out of a series of electrodes called dynodes. Each dynode is kept at a higher voltage than the previous one by a voltage divider circuit. The incident photoelectron is accelerated towards the first dynode and collides with it, extracting secondary electrons. These secondary electrons are then accelerated towards the second dynode, where they collide and release even more secondary electrons. This process repeats for each interstage, exponentially amplifying the signal. At the end of the multiplication stage, the resulting current is collected by an anode. This amplification method allows PMTs to reach high gain in the range of 10^4 - 10^6. The PMT gain has a linear dependence with the bias voltage and can be therefore easily adjusted by changing the voltage provided by the HV module.

Sensitivity to Magnetic Fields

The amplification process employed by PMTs is very sensitive to the influence of magnetic fields. Electrons travel path is relatively long and their trajectories can be easily modified by the presence of a small magnetic field, even with a magnetic flux density inferior to 1 mT [55]. This effect is more relevant at the first stages of the multiplication, where the loss of even a single electron results in a significant variation in the current collected at the anode. PMTs where the distance between the photocathode and the first dynode is long and where the ratio between the first dynode area and the photocathode active surface are is small are the most sensitive to magnetic fields due to the higher risk of losing the original photoelectron.

In tokamaks plasma is confined by strong magnetic fields with magnetic flux densities of a few teslas. In addition, the intensity of these magnetic fields is constant in time but they can evolve during the plasma discharge by significant amounts. These strong and evolving magnetic fields render the use of PMT close to the tokamak troublesome. The amount of material needed for an appropriate magnetic shielding of the detector would make the PMT solution highly inconvenient. A more adequate solution for a compact HXR detector that needs to be positioned close to the tokamak is the SiPM, as discussed in sections 3.1, 3.2.

REGARDS is designed to be positioned at a significant distance from the tokamak. At AUG the detector was positioned behind the torus hall wall along a collimated line of sight of the tokamak midplane at a distance of approximately 11 meters. The concrete wall is two meters thick. As discussed in section 4.1.4 even in this location is possible to measure the effects of the evolving AUG magnetic field due to the high sensitivity of REGARDS. To mitigate the effect of the magnetic fields two layers of magnetic shielding were used. The first and innermost layer a μ-metal magnetic shield case by Hamamatsu (model E989-03) that completely envelops the PMT for its entirety. The second and outermost layer is provided by a soft iron cylinder 10 cm thick placed around the whole HXR detector. The soft-iron cylinder can be seen in figure 4.3 surrounding the detector.

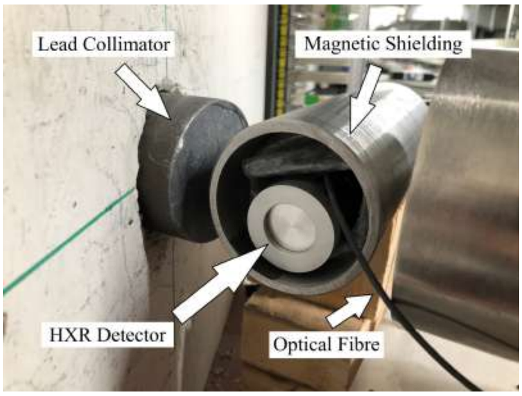

FIGURE 4.3: REGARDS HXR detector at AUG. The tokamak is behind the concrete wall on the left of the picture. The lead collimator can be seen sticking out of the line of sight. The HXR detector is placed inside a soft iron cylinder for magnetic shielding. On the right side of the picture the gain control system optical fiber and the NE-213 neutron spectrometer are visible.

High Rate Non-Linearity

The photomultiplier tube exhibits good linearity over a wide range of incident photon fluxes. However, if the incident light amount is too large, the output anode current begins to deviate from the ideal linearity. This is caused by the parasitic effect on the voltage-divider bias current generated by the output current flowing through the dynodes. The effective current that flows on a given interstage resistance equals the difference between the unbiased divider current and the current flowing through the two consecutive dynodes. The reduction in the effective current between dynodes decreases the voltage difference between them, reducing the secondary electron generation. For relatively small dynode currents this effect is negligible. However, for high incident light levels, the resultant anode and dynode currents are significant and the voltage distribution for each dynode varies considerably.

The divider current has the same value throughout all the voltage-divider. On the other hand, the dynode current monotonically increases at each step of the multiplication process. This means that the voltage drop is more significant on the latter stages of the voltage-divider and especially between the last dynode and the anode. Since the overall cathode-to-anode voltage is kept constant by the high-voltage power supply, the loss of the interstage voltage at the latter stages corresponds to an increase in the interstage voltage in the early stages.

The most significant loss of interstage voltage occurs between the last dynode and the anode, where no secondary electron emission takes place. This causes an overall increase in the voltage of the entire PMT multiplication stage, resulting in a boost of the current amplification. Therefore, for relative large anode current, the PMT response is initially more than linear. If the anode current is further increased the voltage between the last dynode and the anode drops to a level where the anode secondary-electron collection efficiency is seriously degraded. This leads to a fast saturation of the output current and the PMT response becomes quickly less than linear.

Runaway electron discharges can produce severe HXR fluxes, leading to high counting rates scenarios where this effect becomes not negligible. An extreme example of this behaviour is discussed in section 4.1.5.

REGARDS PMT and Acquisition System

After the January 2019 tests, a R9420-100-10 Hamamatsu PMT [44] was selected to better fit the new crystal dimensions. A CAEN HV desktop module (model NDT1470 [56]) is used to power the PMT. The HV module is connected through a USB cable to the acquisition system computer and can be operated remotely. The REGARDS PMT is usually operated in its lower bias voltage range at a value of approximately -570 V. This low bias voltage allows REGARDS to have a wide dynamic range in excess of 20 MeV. This large dynamic range is necessary to collect the entirety of the RE bremsstrahlung emission.

In REGARDS HXR detector output signal is directly recorded by the digital acquisition system without any intermediate pulse shaping circuit. An example of the average REGARDS pulse is shown in figure 4.4.

A fast inorganic scintillator paired with a fast photodetector, like a PMT, grant a very fast output signal. The duration of a REGARDS pulse is approximately 100 ns, with a full width at half-maximum of approximately 30 ns. A very fast signal is required to allow high counting rate operation and to reduce the effects of pile-up. REGARDS proved to be a robust HXR spectrometer even at high counting rates up to a few MCps in runaway electron discharges at the tokamak AUG.

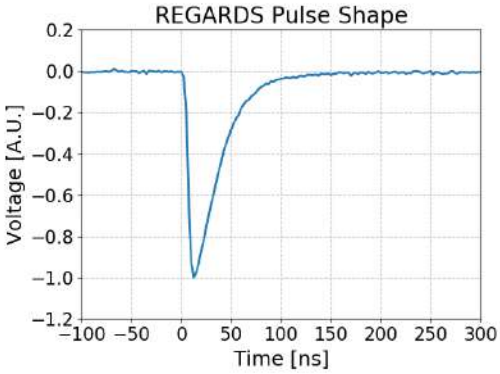

FIGURE 4.4: A typical REGARDS output signal obtained form a radioactive source (^{137}Cs). The pulse duration is approximately 100 ns, allowing for high counting operation in the range of 1 MCps.

The acquisition system chosen for REGARDS is an ADC model NI5772 with PXIe-7976 FlexRIO module by National Instruments [57]. This system grants continuous data collection at a 400 MHz sampling rate for more than 10 seconds. This time is more than sufficient to entirely cover the duration of a plasma discharge in a MST1 tokamak. Given the expected high counting rate for this application, it is preferable to acquire the data in a continuous stream instead of the more common triggered mode. Even though the continuous mode generates bigger data files (approximately 4 GB binary file for 10 seconds of acquisition) loss of data caused by acquisition dead time is prevented. Moreover, pile-up detection and recovery are easier than in a fixed segmented since the entirety of the pile-up event is acquired. REGARDS data acquisition is started with an external TTL trigger to ensure synchronicity with the plasma discharge and other diagnostics. Data is stored in non-volatile memory right after the plasma discharge. This process usually takes a few minutes and happens in the time between two plasma discharges, that are usually tens of minutes apart.

4.1.4 Gain Control System

As presented in section 4.1.3, the two leading causes for detector gain shift during a runaway electron discharge are the presence of an evolving magnetic field and of a high HXR counting rate. The first effect is caused by the residual tokamak magnetic field that is not blocked by the two layers of magnetic shielding and it is able to interact with the PMT and to interfere with its multiplication stage (see section 4.1.3). This effect can be significant due to the strong magnetic fields generated by tokamaks during plasma discharges. Moreover, tokamak magnetic field intensity can drastically change during the discharge, leading to a time-evolving PMT gain shift. Is therefore of great importance to be able to measure this detector gain shift to be sure that the magnetic shielding is adequately mitigating the influence of the residual magnetic field and bring it under a tolerable threshold. The second effect causing a gain shift in the HXR detector is generated by the PMT non-linear response as the signal current approaches the bias voltage-divider current (see section 4.1.3). For runaway electron measurements this is mainly caused by very high HXR counting rates, in the order of the MCps. Once again, it is very important to be able to quantify the amount of gain shift occurred during a runaway electron discharge to be able to ascertain the data quality.

An external gain control system was created to monitor the REGARDS HXR detector gain during the plasma discharge. The principle of operation of this system is to intermittently expose the PMT photocathode to a known and constant light source and to use the resulting signal as a reference throughout the discharge. If no gain shift occurs the reference pulses will all have the same amplitude throughout the discharge, within the statistical fluctuation of the light source. If the detector gain shifts during the plasma discharge, either due to the influence of the tokamak magnetic field or to a strong output current, the reference pulse will also shift accordingly and deviate from the unperturbed value. The gain shift occurred during a plasma discharge can then be computed by isolating the reference pulses and observing the relative deviation from their unperturbed value throughout the discharge.

A schematics of REGARDS gain control system can be seen encircled in the blue dotted box in figure 4.1. The system uses a blue light-emitting diode (model NSPB500AS by Nichia [45]) as a light source. The LED is mounted in a light-tight box to reduce background light noise and to keep the light level to the PMT photocathode within its acceptable range. The light is transported from the LED to the PMT photocathode using an optical fiber. The fiber is securely mounted at both ends to ensure that no movement or dislodgement occurs during operation. Particular care was placed in the HXR detector casing design to ensure a light-tight opening for the optical fiber. An electrical pulse generator (model 577 by Berkeley Nucleonics [58]) is used to fire the LED at a constant rate. The LED bias voltage is kept the same throughout the discharge to ensure the most constant light output as possible.

In our tests, we found that the greatest source of fluctuation in the LED light output was caused by the pulse generator. In particular, the bias voltage generated by our module was not very stable if operated in its mid-lower amplitude range. The solution to this problem was to fire square pulses at its maximum amplitude (+45 V), in a range where the pulse generator is very stable, and then dump the signal with a -20dB voltage attenuator. The resulting voltage bias measured at the LED end is therefore approximately +4.5 V. Using this technique the LED light output was greatly stabilized.

The changing the free parameters of the electrical pulse generator it is possible to modify the LED pulse shape. These values are chosen so that the light emitted by the LED reasonably mimics the scintillation of a high energy HXR interacting with the LaBr3:Ce crystal. For these experiments, we chose to fire the LED at a constant rate of 10 kHz with a square pulse width of 50 ns. The LED equivalent HXR energy is approximately 12.5 MeV. Examples of the gain control system operation are presented in subsections 4.1.5 and 4.1.6.

4.1.5 Tests at COMPASS

The tests performed at the medium-size tokamak COMPASS are a good way to highlight the importance and effectiveness of the gain and control system. In January 2020 REGARDS was transported and installed at COMPASS to test the detector performance at extremely high HXR fluxes. Distance from the tokamak and radiation shielding play crucial roles in managing the intensity of the HXR flux impinging on the detector and, by extension, the HXR counting rate. At COMPASS the available position for the HXR detector was relatively close to the tokamak. Moreover, no existent collimated line of sight was available. The detector was therefore positioned in a room adjacent to the torus hall and oriented in the direction of the tokamak. A 10 cm thick lead collimator was placed in front of it and lead bricks were laid around the remaining sides to shield the detector against background radiation. Figure 4.5 shows the detector setup at COMPASS before it was completely surrounded by the lead bricks.

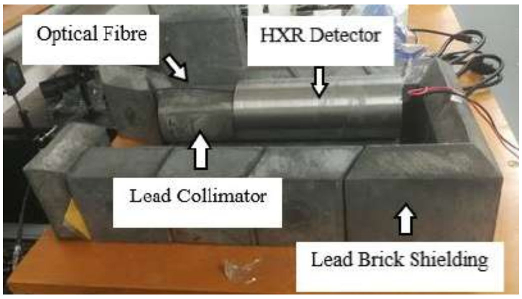

FIGURE 4.5: REGARDS at COMPASS. The HXR detector is place inside the soft iron magnetic shielding cylinder. A 10 cm lead collimator is placed front of the detector. Lead bricks are used to shield the detector from background radiation.

In general, the tests performed at COMPASS were, as expected, characterized by an extreme HXR counting rate. As we will see, this rate was beyond the high counting rate capability of REGARDS and therefore the data quality was compromised. Even though the data collected during these tests is beyond recovery and cannot be used to reliably describe the physics of the RE at COMPASS, it is extremely useful to characterize REGARDS performance and limitations.

In this respect, discharge #19979 is probably one of the most illustrative discharges collected during this experimental session. In this scenario, extremely high counting rates exceeding 10 MCps were recorded. As a consequence, the effect of PMT non-linearity, as discussed in section 4.1.3, are clearly visible. Figure 4.6 (A) shows the time trace of the digitized LED pulses during the discharge as measured by the digital acquisition. To enhance readability, only LED pulses are shown and only the maximum amplitude of each individual LED pulse is plotted. The black dashed line represents the value assumed by the reference LED when unperturbed. This value corresponds to approximately -830 ADC channels. Figure 4.6 (B) shows the relative detector gain shift obtained as the ratio between the measured LED equivalent energy and the reference value for the same discharge.

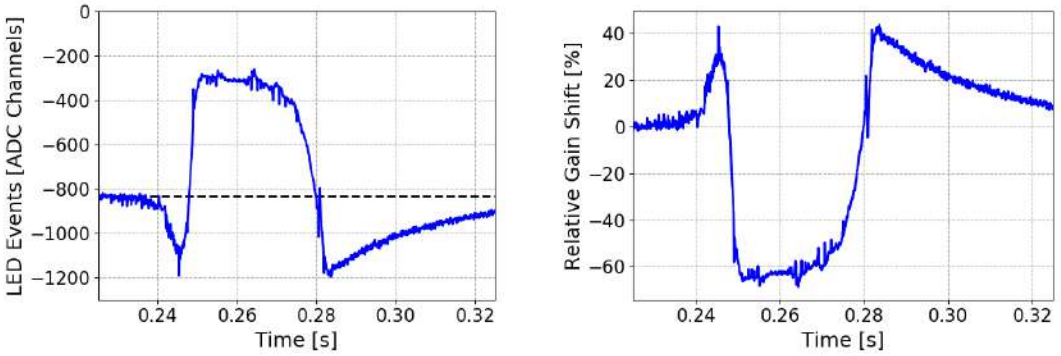

(A)

(B)

FIGURE 4.6: (A) In this graph the maximum amplitude of the LED pulses generated by gain control system are plotted as acquired by the ADC. The dashed black line represents the reference value for an unperturbed LED signal. (B) The relative gain shift computed as the ratio between the measured LED pulse amplitude and the reference value.

In the initial stage of discharge #19979, the HXR high rate causes the detector gain to increase. This is clearly the result of the PMT non-linearity at high output current. The reduction of the voltage difference between the last dynode and the anode results in an overall increase of the interstage voltage difference in the PMT multiplication stage. This process causes the gain increase. This initial phase reaches a maximum with a very high gain shift in excess of +40% at t = 0.245 s, with an HXR counting rate of 4 MCps. The subsequent HXR flux increase caused a sharp gain drop. The further increase in the output current reduced the voltage difference between the last dynode and the anode to a point where the loss in the anode electron collection efficiency prevailed. During this second phase, PMT non-linearity quickly moved from being more than linear to less than linear and the gain shift plunged below a value of -60%. The estimated HXR rate in this stage is in excess of 10 MCps. The detector response remained severely less than linear for most of the duration of the RE discharge. After the conclusion of the runaway electron phase (t = 0.283 s) the detector recovers in a few seconds.

4.1.6 Tests at AUG

Managing the HXR Flux

During the early tests performed at AUG on December 2018 the old 1.5" x 2" $LaBr_3$:Ce detector suffered under a severe HXR counting rate beyond its capability. As a result, the spectrometer design changed and a new HXR detector based on a 1" x 1"

$LaBr_3$:Ce crystal was assembled. On February 2019 the new 1" x 1" $LaBr_3$:Ce detector was tested at AUG. The counting rates experienced by new detector were less severe than the ones experienced by the first one. This improvement was mainly a consequence of the smaller detection efficiency caused by the smaller $LaBr_3$:Ce crystal. Although promising, this reduction in the counting rate was not sufficient to bring the experienced HXR counting rate below the level of a 1 MCps for most of the RE discharges.

A series of 5 mm thick lead sheets were placed in front of the detector to attenuate the HXR signal. A picture of this process can be seen in figure 4.7. By removing or adding a lead sheet it is possible to experimentally find the thickness of material needed to bring the HXR counting rate down to 1 MCps or less. It is also important not to reduce the HXR counting rate too much, since the spectrometer time resolution is intrinsically determined by the HXR statistics. A 30 mm thick lead attenuator was found to provide the optimal shielding.

FIGURE 4.7: REGARDS HXR detector at AUG. Six lead sheets are placed in between the spectrometer and the line of sight to attenuate the HXR flux.

Using an attenuator is a simple and effective way to reduce the HXR flux. Since transmittance of the attenuator material is not uniform throughout the impinging HXR energy range, the attenuator modifies the HXR radiation detected by the spectrometer. A better method to manage the HXR flux impinging on the detector is to use a collimator to narrow the HXR beam. In principle, a collimator should not alter the impinging HXR spectrum but only reduce its flux. After MNCP calculation a 10 cm thick lead collimator with 1 cm aperture in diameter was designed for AUG. In figure 4.8 a comparison between the 3 cm lead attenuator and the 10 cm lead collimator can be appreciated.

Figure 4.8 shows the spectra of a monoenergetic HXR beam measured by the detector when either a collimator or an attenuator is placed in front of the spectrometer. The use of a collimator enhances the detection of the full HXR energy (green region) while introducing a lower amount of low HXR background (red region) when compared whit the attenuator.

Following the results of this MCNP calculations, a cylindrical lead collimator 10 cm thick and with an aperture of 1 cm in diameter was manufactured by the AUG

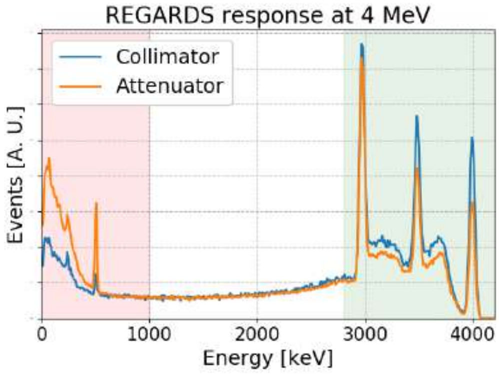

FIGURE 4.8: A comparison between the spectra obtained from a monoenergetic 4 MeV source if either a 3 cm lead attenuator or a 10 cm collimator with an aperture of 1 cm in diameter are used to manage the incoming HXR flux. Results obtained from MCNP simulations.

workshop. The collimator was installed and tested for the first time during the AUG RE experiments in June 2019.

REGARDS Gain Stability

In an ordinary 2019 AUG runaway electron discharge the formation of the runaway electron beam was started around t = 1 s by injecting a large amount of gas into the plasma. The gas most commonly used for this purpose was argon. Figure 4.9 shows the plasma current and the toroidal magnetic field intensity measured during the AUG RE discharge #35887.

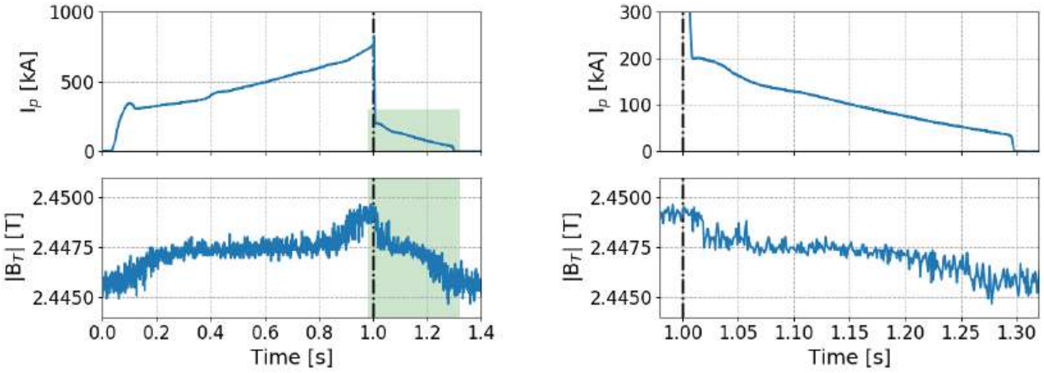

(A) (B)

FIGURE 4.9: (A) The plasma current (top) and toroidal magnetic field (bottom) measured during AUG discharge #35887. The dashed line indicates when the disruption was triggered by a massive gas injection (B) An enlargement of the data shown in the green shaded region of figure (A).

At t = 0 s the discharge is initiated. After the plasma breakdown, the plasma current is steadily increased by the tokamak transformer. Pre-disruption plasma current is often one of the variable sexplored during a RE experiment. The plasma current ramp-up is adjusted to reach the desired value of pre-disruption plasma just before the disruption event is triggered. In this particular shot, a pre-disruption plasma current of 760 kA was achieved at t = 1 s, before the argon massive gas injection triggered the plasma disruption. Subsequent to the plasma collapse, a runaway electron beam was formed. The electrical current carried by the RE beam after the disruption can be seen in figure 4.9 (A) highlighted by the green box. Figure 4.9 (B) shows an enlargement of the RE phase of AUG discharge #35887. In this particular shot, a RE current of 200 kA was achieved. This is more than 26% of the pre-disruption plasma current. As in this case, in a typical AUG RE discharge, the RE phase lasted few hundreds of milliseconds before complete current decay of confinement loss.

Throughout the discharge the, gain control system periodically generates a reference LED pulse of approximately 12.5 MeV. For more details on the gain control system, see subsection 4.1.4. This reference pulse is acquired at the same time as the HXR bremsstrahlung radiation emitted by the runaway electron beam slowing down in the post-disruption plasma. During off-line analysis LED pulses can be distinguished from regular HXR events taking advantage of the signal periodicity and the pulse shape difference. Figure 4.10 shows the spectrum of the HXR events and LED reference pulses collected throughout discharge #35887. The RE bremsstrahlung spectrum is visible in blue. As expected, it is a mostly exponential continuous spectrum with no particular features such as bumps or peaks. The maximum energies measured during this discharge are around 10 MeV. This spectrum is a good example of what a typical AUG RE bremsstrahlung spectrum looks like. A detailed analysis of the AUG RE HXR spectra is presented in chapter 6.

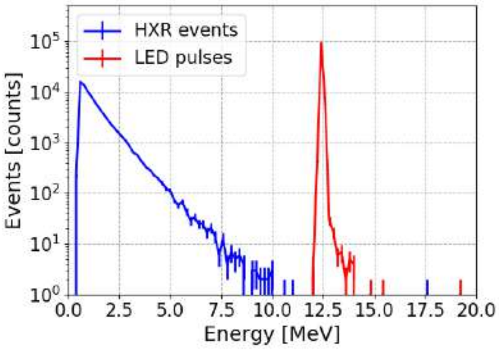

FIGURE 4.10: The HXR spectrum (blue) measured during the AUG discharge #35887. The spectrum of the gain control system LED pulses (red).

Once LED pulses are separated from HXR events, using pulse shape algorithms, it is possible to extract from them information on the detector gain stability. As explained in subsection 4.1.4, if the detector gain shifts this is also reflected on the amplitude of the measured LED pulses. This effect is also visible in the small high energy tail in the LED distribution in figure 4.10. The reference LED value is computed by averaging the equivalent energy of the pulses collected in the last 5 seconds of the acquisition time, more than 3 seconds after the discharge has ended. By this time no residual tokamak magnetic field or high rate HXR radiation is present and so the PMT gain can be assumed to be stable.

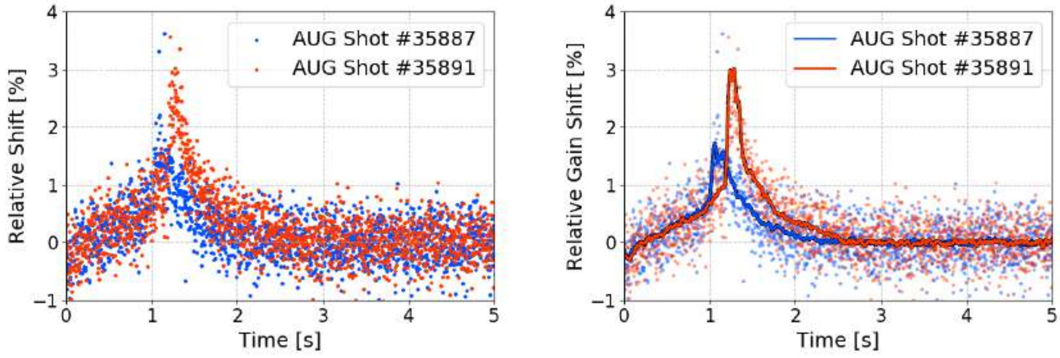

(A)

(B)

FIGURE 4.11: (A) Dots indicate the relative deviation of the measured LED pulsed from the unperturbed reference value for AUG discharges #35887 (blue) and #35891 (red). (B) A Savitzky-Golay filter (solid line) is applied to the data presented in (A) to underline the detector gain shift.

In figure 4.11 (A) the LED events collected throughout the plasma discharge are presented as the relative deviation from the unperturbed reference value for AUG discharges #35887 and #35891. Even when no detector gain shift occurs, the LED emission experience statistical fluctuations. These can be recognized as the vertical spread in the blue and the red dots in the region after 3 s. For this particular discharge, the LED equivalent energy was set to μ = 12.5 MeV as can be appreciated in figure 4.10 (red line). Therefore, μ = 12.5 MeV is also the unperturbed LED reference vale. When unperturbed the LED emission is characterized by a standard deviation σ = 0.042 MeV. This gives a coefficient of variation for the LED events that is equal to σ/μ = 0.34%, that is equivalent to an energy resolution of approximately 0.8% at 12.5 MeV. To highlight the detector gain shift a Savitzky-Golay filter (solid line) is applied to the LED pulses in figure 4.11 (B).

We can divide the pulses #35887 and #35891 into three different phases. The first one is the pre-disruption phase. In this stage, the plasma breakdown is achieved and the plasma current and magnetic fields are ramped up, as can be seen in figure 4.9. This stage starts with the plasma breakdown (t = 0 s) and terminates with the plasma disruption (t = 1.008 s for pulse #35887 and at t = 1.186 s for pulse #35891 respectively). During this initial phase, the progressive increase of the tokamak magnetic field causes the detector gain to shift up to 0.8% for shot #35887 and up to 1.0% for shot #35891. The second stage of the discharge is the runaway electron beam phase, that starts with the plasma disruption and lasts a few hundreds of milliseconds for the duration of the beam. During this phase, the detector gain shift sharply increases right after the massive argon gas injection. This change is the result of the high HXR counting rate experienced by the detector as discussed in section 4.1.3. In figure 4.12 the HXR counting rate during this stage of discharge #35887 is compared to the relative detector gain shift.

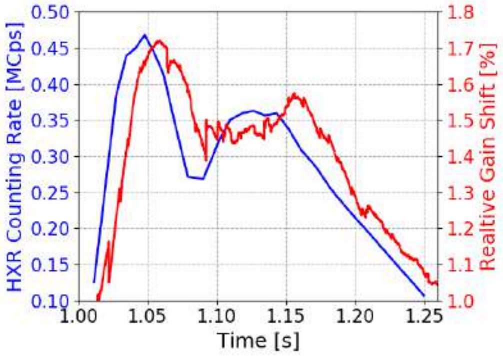

FIGURE 4.12: A clear correlation between the HXR counting rate (blue) and the detector gain shift (red) during the runaway electron phase of AUG discharge #35887.

The correlation between the two curves is clearly visible. A time delay of approximately 13 ms in the detector gain shift can be attributed to finite response time of the detector to the current changes. The maximum HXR counting rates measured in this second stage of the discharges were 0.48 MCps for shot #35887 and 1.23 MCps for shot #35891. Even under these high counting rates, the total detector gain shift was below 3%. In the third and last phase of the discharge, i.e. after the complete termination of the runaway electron beam, it can be noticed that the detectors gain recovers in a few seconds.

The measurement performed during the 2019 MST1 runaway electron campaign at AUG proved the high rate capability of REGARDS. The system gain suffered a shift inferior to 3% even under severe HXR fluxes in excess of 1 MCps. Moreover, data provided by the dedicated LED monitoring system can be used to perform an off-line correction of this small gain shift. A detailed presentation of the data analysis conducted on the data collected through this experimental campaign is presented in chapter 6 of this thesis.

Part III

Runaway Electron Data Analysis

Chapter 5

Analysis Techniques

5.1 The Problem of Inversion

Information on the RE beam energy can be inferred by directly observing the bremsstrahlung radiation emitted in its interaction with the post disruption plasma. As an example, figure 5.1 (B) shows HXR spectra collected by REGARDS during the RE phase of AUG discharge #35887. Both spectra consist of 3000 HXR events. The HXR spectrum presented by blue dots was collected at the beginning of the RE formation while the one presented by red triangles near the end of the RE phase. HXR counting rate for the same discharge is shown in 5.1 (A). The two arrows indicate the bins from which the HXR spectra presented in 5.1 (B) are taken.

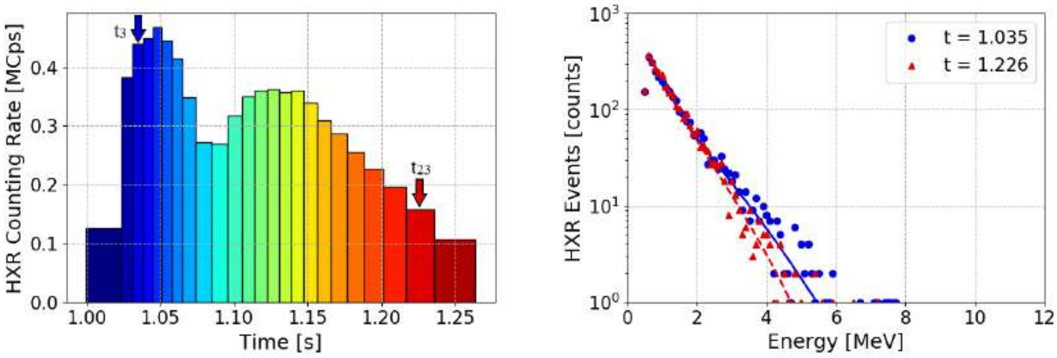

(A)

(B)

FIGURE 5.1: (A) HXR counting rate for AUG discharge #35887. Each bin contains 3000 HXR events. Arrows indicate the two time windows from which HXR spectra displayed in (B) are taken. (B) HXR spectra collected at two different stages of the RE phase. Blue dots indicate the HXR spectrum collected at the beginning of the RE formation, while red triangles refer to the one measured close to the beam termination.

As presented in section 2.2.1, the energy of the HXR photon emitted during the bremsstrahlung process is always less or equal to the initial energy of the deflected runaway electron. The HXR spectrum collected at the beginning of the RE phase of AUG discharge #35887 (blue dots) is more populated in the high energy range ($E_{HXR} \geq 2$ MeV) than the one at the end of the discharge (red triangles). Following this simple observation, we can expect that the RE beam energy was higher during the initial stage of the RE phase than at its end. This type of analysis is useful to qualitatively gauge the behaviour of the RE beam energy throughout the discharge but it is unable to provide more detailed information on the RE energy distribution function.

The goal of this chapter is to illustrate the analysis techniques used to recover the time resolved RE energy distribution function from the bremsstrahlung HXR spectrum. To better explain these techniques it is useful to look at the discretized description of the problem. In this model the binned histogram of the HXR spectrum **S** is related to the discretized runaway energy distribution function **F** through a set of linear equations:

$$\boldsymbol{S} = \boldsymbol{W} \cdot \boldsymbol{F} \tag{5.1}$$

where **S** is a m-dimensional vector and **F** is a n-dimensional vector. **W** is a m x n dimensional matrix. **W** is commonly referred as model or transfer matrix, since **W** maps **F** to **S**. A more complete description of the model can be obtained by expanding **W** in its two components: the matrices **D** and **E**.

$$\boldsymbol{S} = \boldsymbol{D} \cdot \boldsymbol{E} \cdot \boldsymbol{F} \tag{5.2}$$

The p x n dimensional **E** matrix represents the model for the bremsstrahlung emission of the relativistic runaway electrons slowing down in the post disruption plasma. The computation of this matrix takes into account all the relevant post-disruption plasma properties, such as the ion species considered, and the angle of the bremsstrahlung emission with respect to the RE velocity. More information on how this matrix is computed is presented in subsection 5.2.1.

By applying the **E** matrix to the discretized RE energy distribution function **F** we obtain the bremsstrahlung spectrum emitted by the beam **B**, i.e. $\boldsymbol{B} = \boldsymbol{E} \cdot \boldsymbol{F}$. Using this notation, equation 5.2 becomes

$$\boldsymbol{S} = \boldsymbol{D} \cdot \boldsymbol{B} \tag{5.3}$$

The m x p dimensional **D** matrix simulates the detector response function to a generic impinging HXR radiation. Subsection 5.2.2 details the process of determining the detector **D**. The measured spectra **S** is obtained by applying the **D** matrix to B.

Since

$$\boldsymbol{S} = (\boldsymbol{D} \cdot \boldsymbol{E}) \cdot \boldsymbol{F} = \boldsymbol{W} \cdot \boldsymbol{F} \tag{5.4}$$

we have $\boldsymbol{W} = \boldsymbol{D} \cdot \boldsymbol{E}$.

Hence, the transfer matrix **W** is obtained by the dot product of **D** and **E**. This allows for a very modular approach to describe the RE emission. The JET experiments aimed at investigating RE suppression through Shatter Pellet Injection are a good example to illustrate this flexibility. In these experiments, the RE phase was initiated by a massive Ar gas injection. Few hundreds of milliseconds after the beam formation a frozen deuterium pellet was injected into the plasma. The effect of this second injection was to flush out the initial Ar gas and effectively change the background plasma ion species to deuterium. To describe this behaviour in our model it is sufficient to compute two **E** matrices, one with Ar and one with D as the background ion species, and use the appropriate one in each stage of the RE phase of the discharge.

Similarly, if a change in the HXR radiation detection stage is introduced, e.g. by adding additional shielding material in front of the detector to manage the HXR flux, only the **D** matrix needs to be changed and no additional computation of the **E** matrix is required.

Equation 5.1 represents the forward model of the RE bremsstrahlung emission. Given the model matrix **W** and the discretized RE energy distribution function **F**, it predicts the HXR spectrum **S** measured by the detector. The forward model can be used in a synthetic diagnostic approach where a theoretical first-principle calculation of the RE energy distribution function can be tested against the experimental measurement of the HXR bremsstrahlung radiation by computing the expected spectrum using 5.1.

Another viable approach is try to find an energy distribution function $\hat{\boldsymbol{F}}$ that solves for equation 5.1 where, in this case, **S** represent the experimentally measured HXR spectrum and **W** is the computed transfer matrix. This inverse problem is generally ill-posed and many different solutions $\hat{\boldsymbol{F}}_i$ could explain the same measured spectrum **S** within the experimental uncertainty. Different numerical methods, such as Single Value Decomposition, Richardson-Lucy Deconvolution [59] or Tikhonov Regularization, can be applied to ill-posed problems to extract the most reasonable solution. Section 5.3 presents the numerical methods used in this thesis to reconstruct the RE energy distribution function from the HXR spectra measured at the tokamaks AUG and JET. Results of this analysis are shown in chapters 6 and 7 respectively.

5.2 Transfer Matrix Computation

5.2.1 RE Bremsstrahlung Emission

In the discretized model, the **E** matrix describes the RE bremsstrahlung emission. The computation of this matrix is performed using the GENESIS code [60, 61]. The double differential cross section for the generation of a bremsstrahlung HXR can be expressed as [62]

$$\frac{d^2\sigma}{dW d\Omega} = \frac{d\sigma}{dW}(Z, E, k)\frac{1}{2\pi}p(Z, E, k|\cos\theta_V) \tag{5.5}$$

where W is the energy of the HXR, Ω is the solid angle along the emission direction, Z is the ion target atomic number, E is the initial energy of the deflected electron, $k = W/E$, θ_V is the emission angle in respect to the electron velocity. The first term, $d\sigma/dW$, is the bremsstrahlung differential cross-section per unit photon energy. GENESIS uses the semi-empirical Bethe-Heitler differential cross-section presented in equation (49) of [63]. The second term in equation 5.5, $p(Z, E, k|\cos\theta_V)/2\pi$, is the normalized probability distribution function of $\cos\theta_V$ and represents the anisotropy of the relativistic bremsstrahlung emission. As presented in [61], when this term is described by a dipole distribution in the rest frame of the runaway electron, it loses its dependencies on Z and k and can be described as

$$p(Z, E, k|\cos\theta_V) = p(E|\cos\theta_V) = \frac{3}{16\pi}\left[1 + \left(\frac{\cos\theta_V - \beta}{1 - \beta\cos\theta_V}\right)^2\right]\frac{1}{\gamma^2(1 - \beta\cos\theta_V)^2} \tag{5.6}$$

Where $\beta = \sqrt{1 - 1/\gamma^2}$, and $\gamma = 1 + E/(m_e c^2)$. m_e and c are the electron rest mass and speed of light in vacuum, respectively. Figure 2.2 in chapter 2 shows equation 5.6 for different electron energies.

Using GENESIS it is possible to compute the expected bremsstrahlung emission for a monoenergetic RE beam slowing down into a plasma slab. As it appears from equation 5.5, the GENESIS code requires as input the plasma ion impurity Z, the energy of the RE beam E and the angle of emission at which the radiation is collected by the diagnostic $\cos\theta_V$. The code output is a p-dimensional vector of the discretized bremsstrahlung emission spectrum normalized by the plasma ion density n_i and solid angle of emission Ω. Figure 5.2 (A) shows the bremsstrahlung emission computed with GENESIS for six different RE energies. The background plasma used for this simulation was Argon and the angle of emission considered was $\pi/2$, which corresponds to the emission collected by a detector placed along a radial line of sight.

The p x n matrix **E** is constructed by stacking n p-dimensional vectors computed for increasing RE energies. The RE energy range used for this application uniformly covers the interval from 0.1 MeV up to 30 MeV with a step of 0.1 MeV, i.e. n = 300. An identical range was selected for the discretization of the resulting bremsstrahlung vector, p = 300. The resulting 300 x 300 **E** matrix can be seen in figure 5.2.1 (B). This matrix represents the bremsstrahlung emission of a RE beam at the emission angle $\pi/2$ for an Argon background plasma. **E** is a triangular matrix due to the bremsstrahlung property $E_{HXR} \leq E_{RE}$.

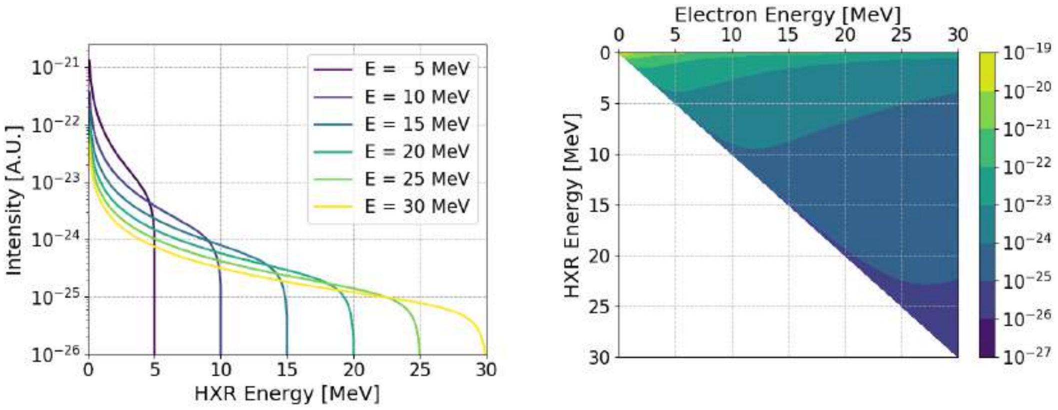

(A) (B)

FIGURE 5.2: (A) Bremsstrahlung emission computed using the GENESIS code for an Ar background plasma. The emission angle considered is $\pi/2$. The emission of six different monoenergetic RE beams are shown. (B) The **E** matrix computed using the GENESIS code. The background plasma considered is purely Ar an the angle of emission is $\pi/2$.

The **E** matrix is normalized by the ion species density. This fact allows to easily combine **E** computed for different ion species to simulate the emission in an impurity mixture plasma, provided that the angle of emission and the energy discretization used are the same for both matrices. As an example, to model the bremsstrahlung emission of a RE beam in a background plasma with a fraction f_{Ar} of Argon and $(1 - f_{Ar})$ of Deuterium the two matrices can be proportionally added:

$$\boldsymbol{E_{mix}} = f_{Ar} \cdot \boldsymbol{E_{Ar}} + (1 - f_{Ar}) \cdot \boldsymbol{E_D} \, . \tag{5.7}$$

This property is extremely useful since it allows to model any possible gas mixture by just computing the **E** matrices for the elementary ion species and then combining them according to their fractional abundances to obtain the desired result.

5.2.2 Detector Response Function

The detector response function matrix (**D**) is computed using Monte Carlo N-Particle Transport (MCNP). MCNP is a Monte Carlo radiation transport code developed by Los Alamos National Laboratory [64]. The role of the **D** matrix is to describe the detection of the bremsstrahlung photons emitted by the RE beam. For this purpose, full models of the HXR detectors employed for the RE experiments and their surrounding materials were created.

Given the scintillator crystal material and dimensions and the energy of the HXR source, MCNP simulates the crystal detection efficiency and the relative probability of Compton scattering, photoelectric effect and pair production. An example of this computation can be seen in figure 5.3 (A). This picture shows the expected HXR spectra measured by the REGARDS HXR detector for six impinging monoenergetic

HXR sources. As the energy increases the detector detection efficiency decreases and the relative proportion of Compton scattering, pair production and photoelectric effect changes.

The **D** matrix is generated by stacking the detector response function of several monoenergetic HXR sources, in a way similar to the method used for the computation of the **E** matrix detailed in subsection 5.2.1. For the purpose of the RE experiment analysis, the HXR spectrometers **D**s were computed using an energy range spanning from 0.1 MeV up to 30 MeV with a step of 0.1 MeV for both the HXR monoenergetic source and for the resulting discretized HXR spectrum. Figure 5.2.2 (B) shows the **D** matrix for REGARDS spectrometer. Since the energy range of the detected spectrum is lower than or equal to the energy of the HXR source, the resulting **D** matrix is triangular. The region corresponding to the full energy, single escape and double escape peaks can be appreciated near the diagonal. The intensity of these peaks fades as the HXR source energy increases. A thin horizontal line corresponding to the detection of the 511 keV annihilation photon can be seen near the upper axis.

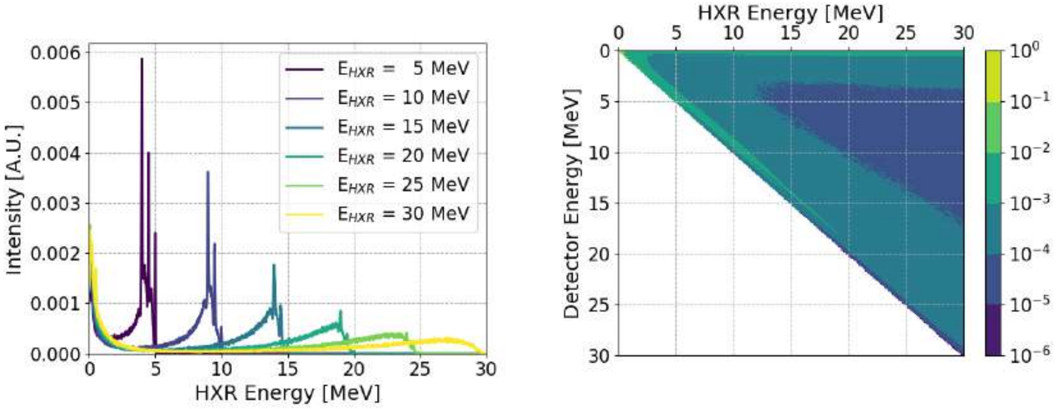

(A) (B)

FIGURE 5.3: (A) Expected HXR spectra measured by REGARDS spectrometer for different monoenergetic HXR sources. These spectra were computed using MCNP. (B) The REGARDS spectrometer **D** matrix computed using MCNP.

The **D** matrix includes also the effect of the materials surrounding the detector. Of most importance are the shielding materials placed in front of the HXR spectrometer to either manage the incoming HXR flux or to block neutrons. The effect of these materials on the overall spectrometer detection efficiency and on the measured HXR spectra is significant, and therefore they must be carefully included in the MCNP calculations. Figure 4.8 shows the effect of two different types of shielding placed in font of the REGARDS spectrometer. One is a 3 cm lead solid brick while the other is a 10 cm lead collimator with a 1 cm diameter aperture. The two D matrices were computed to design the best shielding configurations for REGARDS detector at AUG. It is worth noting that the two matrices are not interchangeable when it comes to the analysis of the data collected during the AUG RE campaign. Using the wrong matrix results in an under or overestimation of the attenuation of the incident HXR beam and, consequently, this leads to an error in the reconstructed RE energy distributions. A detailed discussion on the differences between the two shielding configuration is presented in subsection 4.1.6. Finally, **D**s of the large JET LaBr$_3$:Ce spectrometers were computed to allow for analysis of the JET RE experiments.

5.3 Inversion Techniques

Reconstruction of the RE energy distribution function from the measured HXR bremsstrahlung spectrum is an ill-posed problem. Several possible solutions $\hat{\boldsymbol{F}}_i$ can explain the same collected data within the experimental uncertainties. This is a consequence of a loss of information in the forward process. In principle all valid solutions are equally acceptable, therefore it is necessary to introduce some additional assumptions in order to discriminate amongst them and obtain a unique solution.

Several numerical methods can be applied to an inversion problem. Tikhonov Regularization was found to be the most effective for this application.

5.3.1 Tikhonov Regularization

Tikhonov Regularization [65, 66] is part of the family of the Regularized Least Squares methods commonly employed to solve ill-posed problems. As an example, this method is currently used in tomographic velocity-space inversions of fast ion measurements in fusion plasmas [67, 68, 69, 70, 71, 72, 73, 74, 75].

In Tikhonov Regularization, the solution is found by finding **F** that minimizes the following problem

$$minimize\,\{\|\boldsymbol{W}\cdot\boldsymbol{F}-\boldsymbol{S}\|_2^2+\alpha\,\|\boldsymbol{L}\cdot\boldsymbol{F}\|_2^2\}\;with\,\boldsymbol{F}\geq\boldsymbol{0} \tag{5.8}$$

where **W** is the transfer matrix, **F** is the discretized RE energy distribution function, **S** is the measured bremsstrahlung spectrum, α is the regularization parameter, **L** is the regularization matrix and $\|\ldots\|_2$ is the Euclidean norm. Solution must obey the constraint $\boldsymbol{F}\geq\boldsymbol{0}$ to represent an acceptable runaway electron energy distribution function.

The addition of the regularization matrix **L** allows to introduce additional assumptions on the solution $\hat{\boldsymbol{F}}_i$. By appropriately choosing the **L** matrix it is possible to penalize or favour some features in the shape of $\hat{\boldsymbol{F}}_i$. In 0^{th}-order Tikhonov Regularization the identity matrix **I** is chosen as the regularization matrix **L**. This choice penalizes solutions with large amplitudes. In 1^{st}-order Tikhonov Regularization the first derivative operator is chosen as **L** and therefore solutions with large gradients are penalized. These two are the most commonly used regularization matrices. Nevertheless, higher orders of the derivative operator or even custom regularization matrix can be used for particular applications.

The regularization parameter α is a non-negative constant that controls the intensity of the regularization. The higher the value of α, the higher the regularization term will weight in 5.8, thus providing a more regularized solution. Several empirical methods, e.g the L-curve method [76], can be used to select an adequate value for the regularization parameter.

Finally, problem 5.8 can be equivalently restated as

$$minimize \left\| \begin{bmatrix} \boldsymbol{W} \\ \alpha \boldsymbol{L} \end{bmatrix} \cdot \boldsymbol{F} - \begin{bmatrix} \boldsymbol{S} \\ \boldsymbol{0} \end{bmatrix} \right\|_2^2 \quad with\, \boldsymbol{F} \geq \boldsymbol{0}. \tag{5.9}$$

This formulation is more convenient since the problem takes the form of as a least-square problem. This allows the use of optimized numerical algorithms to efficiently find solutions complying with the non-negative constraint [77].

The 1^st-order Tikhonov Regularization method was used to recover the runaway electron energy distribution function from the measured bremsstrahlung spectra collected during the RE experiments at the tokamaks AUG and JET. The results of this analysis are presented in detail in chapters 6 and 7, respectively.

Figure 5.4 shows the RE energy distribution functions reconstructed for the two HXR spectra of AUG discharge #35887 shown in figure 5.1 (B). The lines in figure 5.1 (B) represent the spectra obtained by applying the forward model (equation 5.1) to the solutions found using the Tikhonov Regularization algorithm. The shaded area in figure 5.4 represents a 1-σ confidence interval in the reconstruction. To compute this confidence interval, 100 different synthetic HXR spectra were generated starting from the original measured bremsstrahlung spectrum assuming Poisson statistics. Tikhonov Regularizatlyion was then performed on each of them. The confidence interval is the results of the statistical analysis of these new solutions. In figure 5.4 we can notice the shape of the RE distribution function. The average energy of the beam decreases during the RE phase of the discharge. Moreover, we can notice that the high energy range ($E_{RE} > 5$ MeV) is more populated at the beginning of the RE phase than at the end. This confirms the qualitative observation on the runaway electron energy evolution made directly from the HXR spectra in section 5.1.

Tikhonov Regularization allows for quantitative reconstruction of the RE energy distribution function. In addition, if the spectra collected during the entire RE phase of the discharge is subdivided in time windows (e.g. as shown in figure 5.1 (A)) this analysis can offer information on the time evolution of such energy distribution.

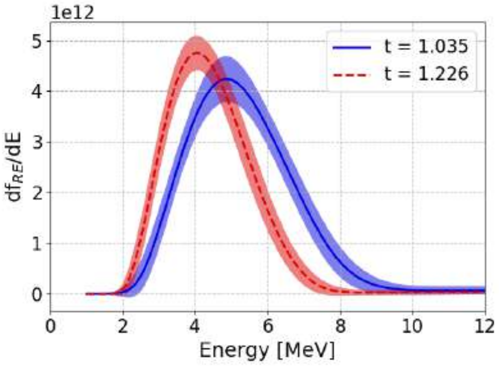

FIGURE 5.4: RE energy distribution functions reconstructed using the $1^{s}t$-order Tikhonov Regularization algorithm for the two different stages of the RE phase in discharge #35887 shown in figure 5.1.

5.3.2 Poisson Statistics

Tikhonov Regularization has an implicit built-in assumption of normal distributed data. This is more evident if $\alpha = 0$ is chosen. the problem 5.8 becomes a least square problem

$$minimize \ \|\boldsymbol{W} \cdot \boldsymbol{F} - \boldsymbol{S}\|_2^2 \ with \, \boldsymbol{F} \geq \boldsymbol{0} \tag{5.10}$$

In this formulation, the optimal solution $\hat{\boldsymbol{F}}$ is the one that minimizes the norm of the residual. On the other hand, the number of counts in each bin of the HXR spectrum is subject to Poisson statistics. The difference between the two statistics is less relevant when the number of counts in a bin is high but becomes noticeable when there are few counts in a given bin. In this application the region of greatest discrepancy is the high energy part of the bremsstrahlung spectrum ($E_{HXR} > 5$ MeV), where few counts (< 5) are expected.

A modified version of the Tikhonov Regularization algorithm based on the Poisson statistic was implemented [78, 79]. In this new formulation the residual norm in equation 5.8 is substituted by the negative Poisson log likelihood:

$$minimize \ \left\{ \ell(\boldsymbol{W} \cdot \boldsymbol{F} | \boldsymbol{S}) + \frac{\alpha}{2} \|\boldsymbol{L} \cdot \boldsymbol{F}\|_2^2 \right\} \ with \, \boldsymbol{F} \geq \boldsymbol{0}. \tag{5.11}$$

where $\ell(\boldsymbol{W} \cdot \boldsymbol{F} | \boldsymbol{S})$ is the negative Poisson log likelihood

$$\ell(\boldsymbol{W} \cdot \boldsymbol{F} | \boldsymbol{S}) = \sum_{i=1}^{n} ([\boldsymbol{W} \cdot \boldsymbol{F}]_i + \beta) - \sum_{i=1}^{n} (S_i \log([\boldsymbol{W} \cdot \boldsymbol{F}]_i + \beta)). \tag{5.12}$$

where β is a small positive constant.

The modified 1^{st}-order Tikhonov Regularization algorithm was used to analyse the data collected during the RE experiments at AUG and JET. An example of the RE energy distribution reconstructed using this algorithm can be seen in figure 5.5. The same two HXR spectra from AUG discharge #35887 are presented in figure 5.5

(A). The best fit line of the modified Tikhonov regularization includes more points in the high energy range ($E_{HXR} > 5$ MeV) where the number of counts is small. As a result, the reconstructed RE energy distribution function shown in figure 5.5 (B) is very similar to the one found with the traditional 1^{st}-order Tikhonov Regularization algorithm with the exception of two small high energy tails in the distribution.

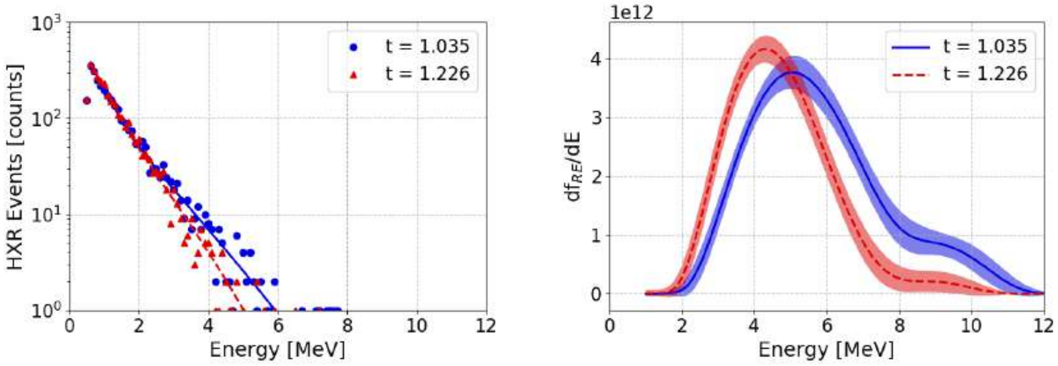

(A) (B)

FIGURE 5.5: (A) HXR spectra collected at two different stages of the RE phase of AUG discharge #35887. Blue dots indicate the HXR spectrum collected at the beginning of the RE formation, while red triangles the one measured near the beam termination. Lines indicate the best fit for the modified Tikhonov Regularization algorithm. (B) RE energy distribution functions obtained with the modified 1^{st}-order Tikhonov Regularization algorithm.

The downside of using this algorithm is that it is approximately 1 order of magnitude slower than the traditional Tikhonov Regularization algorithm. This is mostly due to the less efficient minimization algorithm (Truncated Newton method) used to find a non-negative solution $\hat{F}$. Further optimization of the algorithm could reduce the computational time.

Chapter 6

Runaway Electrons at ASDEX Upgrade

6.1 Experiments Overview

The Runaway Electron GAmma-Ray Detection System (REGARDS, see chapter 4) was deployed in December 2018 at the tokamak ASDEX Upgrade to collect data for the EUROfusion MST1-T08 campaign.

The MST1-T08 campaign is a series of experiments dedicated to foster the understanding of the runaway electron physics with particular focus on their interaction with injected gas and magnetic perturbations. The goals of the MST1-T08 experiments include the study of mitigation techniques such as massive gas injection (MGI) [12, 13, 14, 15, 16] and resonant magnetic perturbation (RMP) [21, 22, 23, 24], the exploration of the effect of plasma geometry on post-disruption RE generation and the identification of the conditions needed for achieving runaway-free disruptions. In parallel to the experimental sessions, T08 focuses on development and validation of modelling tools, with particular attention on mitigation techniques.

EUROfusion MST1-T08 experiments are performed in different medium-sized tokamaks across Europe, namely Asdex Upgrade, TCV, MAST-U and COMPASS. REGARDS results obtained within this framework at the COMPASS tokamak are briefly presented in subsection 4.1.5. The goal of this chapter is to showcase the analysis technique of the data collected at AUG.

In a typical AUG runaway electron discharge, the beam generation is triggered by an Ar MGI disruption at t = 1 s. The pre-disruption parameters, such as plasma current, plasma geometry and magnetic field intensity can be modified to study the effects of initial conditions on the RE beam generation. After the RE beam formation, different mitigation techniques can be investigated. The RE phase at AUG typically lasted a few hundreds of ms before the beam was lost or terminated.

6.1.1 Discharge List

Table 6.1.1 shows a complete list of the MST1-T08 AUG discharges measured with REGARDS. The same data was analyzed using the Tikhonov Regularization inversion technique to reconstruct the RE energy distribution function. A highlight of the analysis results is given in section 6.2.1.

Few useful additional information is presented on the table, such as the pre-disruption plasma current I_{P0}, the post-disruption runaway current I_{RE}, the current drop $I_{P0} - I_{RE}$, the target species used to trigger the disruption and the type of HXR attenuation used for that particular discharge. For more information on this last point see subsection 4.1.6.

The last column in table 6.1.1 presents a short note on the quality of the HXR data collected. *Good pulse* indicates a discharge were the HXR detector gain was stable and where the HXR statistics was sufficiently high to allow for a time-resolved analysis of the RE phase. *Low counts* marks a discharge where the HXR statistics was low (total HXR counts < 1000). This scenario commonly happens when a very short-lived RE beam is generated after the disruption. Since HXR statistics dominate the temporal resolution of the system, a time analysis of the RE energy distribution function is not achievable for these discharges. At the other hand of the spectrum, if the HXR counting rate is to high (> 2 MCps) the detector gain could shift significantly (see subsection 4.1.3). When this effect causes the detector gain to shift beyond 10% we deem that data cannot be recovered and the pulse is not analysed. Only three pulses (#36421, #36429 and #38076) surpassed this threshold and were rejected. These pulses are indicted in table 6.1.1 by the label *Not stable*. Finally, *Pulse lost* tags the discharges where data was lost due to a failure in the acquisition system, usually a false trigger.

AUG Discharge #	I_{P0} [kA]	I_{RE} [kA]	$I_{P0} - I_{RE}$ [kA]	Plasma Species	HXR Flux Attenuation	Notes
35885	717	6	712	Ar	Attenuator	Low counts
35886	719	128	591	Ar	Attenuator	Good pulse
35887	763	200	562	Ar	Attenuator	Good pulse
35888	768	98	669	Ar	Attenuator	Good pulse
35889	767	198	569	Ar	Attenuator	Good pulse
35890	768	169	599	Ar	Attenuator	Good pulse
35891	962	380	582	Ar	Attenuator	Good pulse
35892	921	6	915	Ar	Attenuator	Low counts
36225	768	8	760	Ar	Attenuator	Low counts
36226	767	151	616	Ar	Attenuator	Good pulse
36227	768	71	696	Ar	Attenuator	Good pulse
36228	766	133	633	Ar	Attenuator	Good pulse
36229	768	127	640	Ar	Attenuator	Good pulse

AUG Discharge #	I_{P0} [kA]	I_{RE} [kA]	$I_{P0} - I_{RE}$ [kA]	Plasma Species	HXR Flux Attenuation	Notes
36230	768	131	637	Ar	Attenuator	Good pulse
36231	767	138	629	Ar	Attenuator	Good pulse
36232	767	161	607	Ar	Attenuator	Good pulse
36259	965	248	717	Ar	Attenuator	Good pulse
36260	963	186	777	Ar	Attenuator	Good pulse
36313	810	219	591	Ar / Kr	Attenuator	Pulse lost
36416	985	9	976	Ar	Collimator	Low counts
36417	985	289	695	Ar	Collimator	Good pulse
36418	981	4	977	Ar	Collimator	Low counts
36419	702	128	574	Ar	Collimator	Good pulse
36420	701	4	697	Ar	Collimator	Low counts
36421	849	180	668	Ar	Collimator	Not stable
36423	847	4	843	Ar	Collimator	Low counts
36424	768	99	669	Ar	Collimator	Good pulse
36425	770	10	760	Ar	Collimator	Low counts
36426	769	179	590	Ar	Collimator	Good pulse
36427	760	4	755	Ar	Collimator	Low counts
36428	761	6	755	Ar	Collimator	Low counts
36429	933	125	808	Ar	Collimator	Not stable
36431	759	249	510	Ar	Collimator	Good pulse
36432	761	6	755	Ar	Collimator	Low counts
36433	760	6	754	Ar	Collimator	Low counts
36436	766	6	759	Ne	Collimator	Low counts
36437	766	3	763	Ne	Collimator	Low counts
36438	766	3	763	Ne	Collimator	Low counts
37779	800	90	710	Ar	Collimator	Low counts
37780	800	172	628	Ar / D	Collimator	Good pulse
37783	800	200	600	Ar	Collimator	Good pulse
37784	800	180	620	Ar	Collimator	Pulse lost
37785	800	235	565	Ar	Collimator	Good pulse
37786	800	170	630	Ar	Collimator	Good pulse
37787	800	60	740	Ar / D	Collimator	Low counts
37789	800	150	650	Ar	-	Good pulse
37790	800	196	604	Ar	-	Good pulse
37791	800	175	625	Ar	-	Good pulse
37792	800	230	570	Ar	Collimator	Pulse lost
37793	800	190	610	Ar	Collimator	Pulse lost
38076	1000	260	740	Ar	-	Not stable
38077	800	265	535	Ar	Collimator	Good pulse
38078	800	230	570	Ar	Collimator	Good pulse

AUG Discharge #	I_{P0} [kA]	I_{RE} [kA]	$I_{P0} - I_{RE}$ [kA]	Plasma Species	HXR Flux Attenuation	Notes
38079	800	260	540	Ar	Collimator	Good pulse
38080	800	220	580	Ar	Collimator	Good pulse
38081	800	225	575	Ar	Collimator	Good pulse
38082	800	220	580	Ar	Collimator	Good pulse
38084	800	155	645	Ar	Collimator	Good pulse
38086	800	160	640	Ar	Collimator	Good pulse
38087	800	220	580	Ar	Collimator	Good pulse
38088	800	220	580	Ar	Collimator	Good pulse

TABLE 6.1: A list of the MST1-T08 AUG discharges collected with REGARDS. Information on a few of the discharge parameters is presented.

6.1.2 Detector Stability

As presented in subsections 4.1.3 and 4.1.3, the REGARDS HXR detector gain can shift under the influence of the AUG residual magnetic field and under severe HXR flux. During the MST1-T08 AUG campaign, the maximum gain shift experienced was $< 5\%$ for all discharges except the three labelled as *Not stable* in table 6.1.1. A gain shift inferior to 5% was deemed small enough for the purposes of the analysis of these discharges and no off-line correction was applied to the data.

During AUG discharges #36421, #36429 and #38076 the gain shift exceeded 30% with an estimated HXR counting rate in excess of 10 MCps. In discharges #36421 and #36429 the extreme HXR flux was likely caused by an impact of the runaway electron beam on the plasma-facing component of the vessel. The magnetic axis position can be used as a crude approximation of the RE beam centre location inside the vessel. In these two discharges, the magnetic axis time traces suggest a rapid loss of confinement of the RE beam and hints to a possible impact. Finally, the high HXR flux experienced during AUG discharge #38076 was caused by the lack of HXR attenuation in front of the detector.

6.2 Analysis of the AUG RE Experiments

The toroidal electric field $E_{\parallel}$ that accelerates the runaway electrons during the current quench phase can be described as:

$$E_{\parallel} = \frac{V_l}{2\pi R_0} \simeq \frac{L}{2\pi R_0} \frac{I_{P0} - I_{RE}}{\tau_d} \tag{6.1}$$

where V_l is the loop voltage, R_0 is the radial position of the runaway beam, L is the plasma inductance, I_{P0} is the pre-disruption plasma current, I_{RE} is the post-disruption runaway current and τ_d is the current quench time.

Under the assumption of similar L and τ_d throughout different discharges we can expect a larger accelerating toroidal electric field for higher current drops $I_{P0} - I_{RE}$.

A correlation between the maximum energy of the bremsstrahlung spectrum E^*_{HXR} and the current drop $I_{P0} - I_{RE}$ can be observed from the data collected during the MST1-T08 AUG experiments. Figure 6.1 shows the measured E^*_{HXR} as a function of the current drop $I_{P0} - I_{RE}$ for the AUG discharges in table 6.1.1 labeled as *Good pulse*. The maximum energy E^*_{HXR} of the spectrum is computed as the value at which the cumulative distribution of the HXR events reaches 90%.

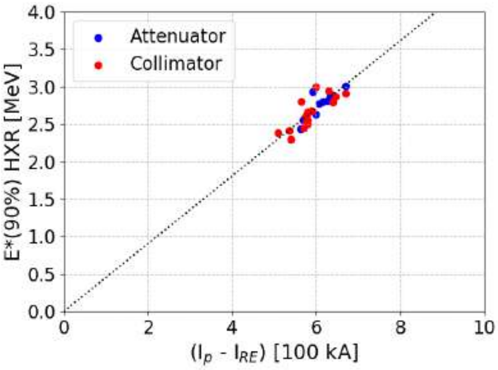

FIGURE 6.1: The measured E^*_{HXR} as a function of the current drop $I_{P0} - I_{RE}$ for the *Good pulse* discharges in table 6.1.1. Blue dots indicate data collected using the HXR lead attenuator, while red dots data acquired with the lead collimator. The dashed black line indicates the linear best fit.

The blue dots in figure 6.1 represent data collected using the 3 cm lead plates as HXR attenuation while the red dots indicate data measured using the lead collimator. The black dotted line is the linear best fit. The slope m = 0.452 ± 0.003.

This simple example shows that the measured HXR bremsstrahlung contains information on the runaway electron physics. In the next subsection, more sophisticated inversion techniques are applied to the measured HXR bremsstrahlung radiation to reconstruct the RE energy distribution function and to characterize the beam evolution throughout the discharge.

6.2.1 Reconstruction of the RE Energy Distribution Function

Integral quantities of the reconstructed runaway energy distribution function, such as the average energy $<E_{RE}>$ or the maximum energy E^*_{RE}, are useful to characterize the global behaviour of runaway electron beam throughout the discharge. These parameters are less dependent on the fine structure of the reconstructed energy distribution and are therefore more robust against possible artefacts introduced by the inversion algorithm.

The vertical black dashed line in figure 6.2 indicates the average energy $<E_{RE}>$ of the reconstructed RE energy distribution function (in blue). For the purposes of this analysis, the maximum RE energy E^*_{RE} is defined as the energy value at which the RE cumulative energy distribution reaches the value of 90%. E^*_{RE} is shown in figure 6.2 by a vertical solid black line. E^*_{RE} is a useful parameter to describe the general behaviour of the energetic tail of the RE distribution function.

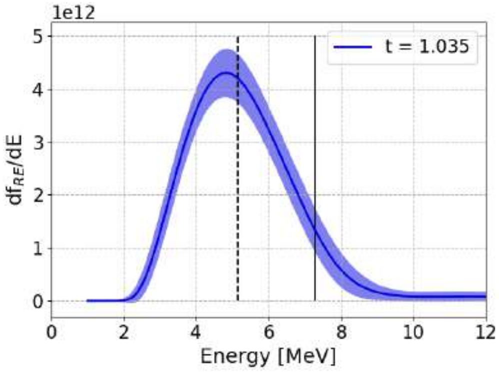

FIGURE 6.2: Different integral parameters of the RE energy distribution function (blue). The vertical black dashed line indicates the average energy $<E_{RE}>$ while the vertical solid black line the maximum energy E^*_{RE}.

By monitoring the evolution of these parameters, information can be extracted on the behaviour of the RE beam energy throughout the discharge. Figure 6.3 presents time traces of the average RE energy $<E_{RE}>$ (panel A) and the maximum energy E^*_{RE} (panel B) for AUG discharge #35887.

The $<E_{RE}>$ and E^*_{RE} traces time resolution is determined by the HXR events statistics. For this analysis the measured HXR data was subdivided into different time intervals, each one containing 3000 HXR events. Figure 5.1 (A) shows the different time intervals used for discharge #35887. The bin time steps are adjusted so each interval contains the same number of HXR events. The average time step for this analysis is approximately 10 ms.

Time traces of the relative $<E_{RE}>$ and E^*_{RE} are shown respectively in 6.3 (A) and (B). In these panels, the same colour scheme as the one for time intervals in figure 5.1 (A) was used.

The $<E_{RE}>$ and E^*_{RE} time traces allow for a quantitative description of the RE beam energy evolution. After the beginning of the RE generation, the RE beam energy remains almost constant, with a slight increase. This behaviour is visible both in $<E_{RE}>$ and in E^*_{RE} up to t = 1.10 s. After t = 1.10 s E^*_{RE} starts to progressively decrease while $<E_{RE}>$ remains constant. This behaviour is caused by a loss in the high energy tail of the RE energy distribution paired with an overall increase of the beam energy. After t = 1.14 s the $<E_{RE}>$ starts to decrease in a similar way to E^*_{RE}. This evolution can also be appreciated in figure 6.4 where the RE energy distribution function is presented at different moments of the discharge. Here the

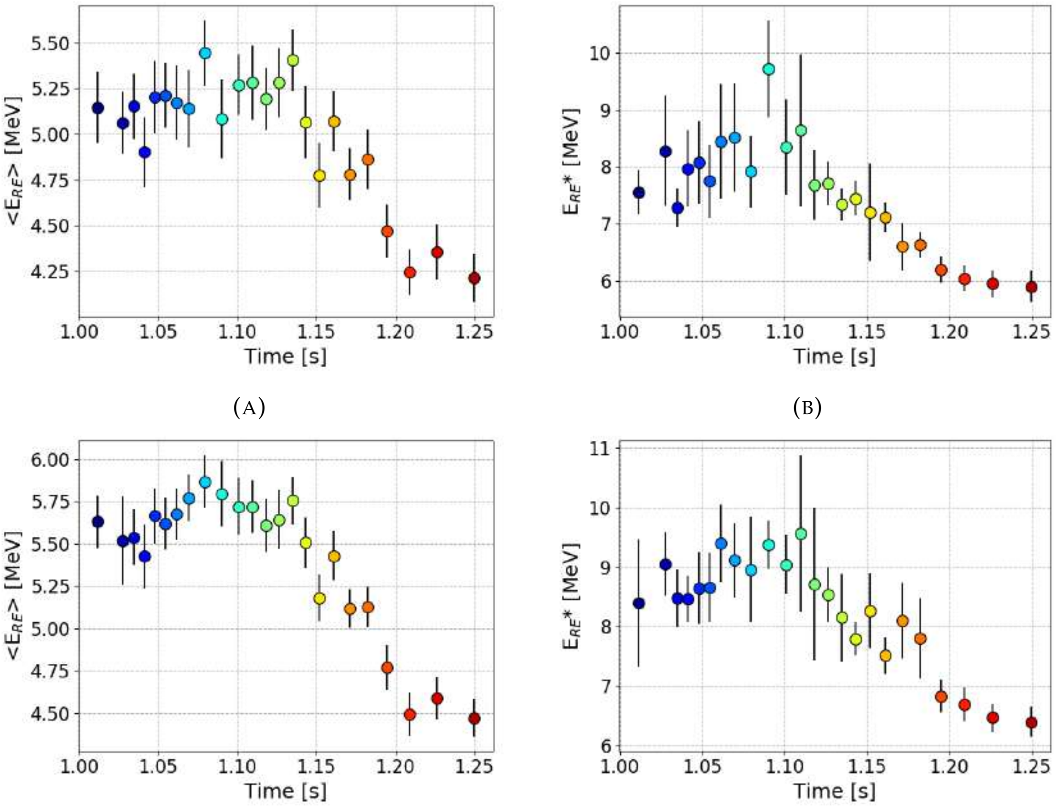

(A) (B)

(C) (D)

FIGURE 6.3: A comparison between the inversion results obtained for AUG discharge #35887 using the Tikhonov regularization (top panels) and the Poisson-like Tikhonov regularization (bottom panels). The average energy and the maximum energy computed from the reconstructed runaway electron energy distribution functions are presented on the left and right side respectively.

colour associated with t = 1.135 s was changed from yellow to green to enhance readability.

Figure 6.3 more broadly shows a comparison between the $<E_{RE}>$ and E^*_{RE} computed using Tikhonov regularization (top panels) and the Poisson-like Tikhonov regularization algorithm (bottom panels) for the same discharge (AUG #35887).

The values of $<E_{RE}>$ and E^*_{RE} obtained using the two different methods are very similar. Values obtained using the Poisson-like Tikhonov regularization algorithm are slightly higher ($\approx$ 0.5 MeV) due to the higher relative weight of the less populated high energy bins (see subsection 5.3.2). This similarity between the results obtained using the two algorithms was observed for all the AUG discharges presented in table 6.1.1. As discussed in subsection 5.3.2 the Poisson-like Tikhonov algorithm is far less computationally efficient than the regular Tikhonov Regularization technique. The computational time needed to invert the same dataset with the Poisson-like Tikhonov algorithm is approximately 9 times slower than with the regular Tikhonov Regularization. Therefore, while the Poisson-like Tikhonov algorithm is formally a more suitable method for the inversion the measured HXR spectrum,

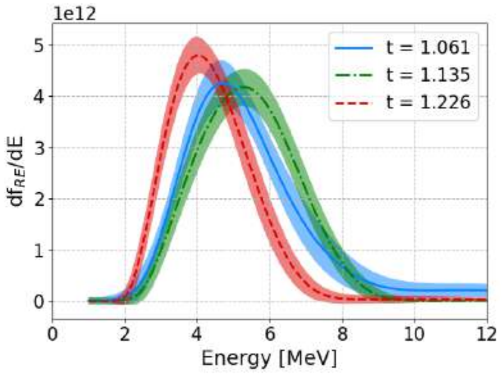

FIGURE 6.4: The evolution of the RE energy distribution function throughout AUG discharge #35887. The color associated with t = 1.135 s was changed from yellow to green to enhance readability.

Tikhonov regularization can deliver a much faster and still reasonably accurate deconvolution.

The analysis technique described in this chapter was adopted for all the *Good pulse* AUG discharges presented in table 6.1.1. A complete review of the analysis results is currently underway and it is soon to be published.

6.2.2 Test Particle Model

A simple test particle model was implemented to study the expected dynamics of the runaway electron as a function of the plasma parameters measured during an AUG RE discharge. The model includes acceleration of the RE particle by the toroidal electric field, collisions with the background plasma and deceleration due to radiation losses [80, 81, 82, 83]. Given the companion plasma parameters, the momentum space of the runaway electrons can be computed.

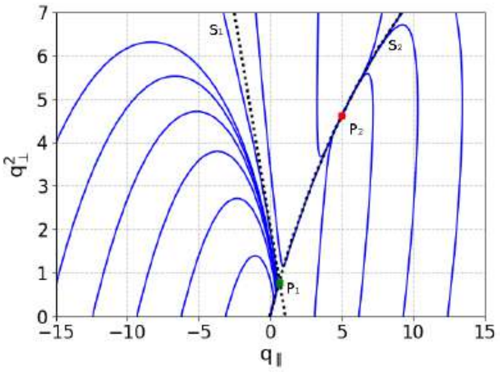

FIGURE 6.5: RE momentum space. The two separatrices are indicated by the dotted black lines. The green P_2 dot is the saddle point, while the red P_1 dot is the stable focus point. The blue lines denote the test particle trajectories.

Figure 6.5 shows an example of RE momentum space. $q_{\parallel}$ and $q_{\perp}$ are the components relative to the magnetic field of the normalised momentum $q = p/m_e c$. Blue lines show the test electron trajectories in the momentum space.

When the accelerating toroidal electric field is larger than the critical electric field necessary for RE generation [8], the RE momentum space is characterized by two separatrices and two critical points as shown in figure 6.5. Electron trajectories inside the S_1 separatrix (left side in figure 6.5) will eventually converge to the origin ($q = 0$). This region contains electrons that due to collisional and radiative losses thermalize and do not become runaways. On the other hand, electron trajectories outside the S_1 separatrix do not thermalize and eventually converge to the stable focus point P_2. This critical point represents the maximum energy that the test RE electron can reach taking into account relativistic effects and radiative losses. The area outside the separatrix S_1 (right side in figure 6.5) represents the runaway electron region. The intersection of the two separatrices is the saddle point P_1.

If the toroidal electric field is less strong than the critical value the electron momentum space does not present any critical point and all the test electron trajectories converge to the origin. As a consequence all test particles thermalize and no runaway electron is created.

The RE momentum space can be easily converted in the more immediate RE energy E and pitch μ coordinates. The pitch angle is defined as $\mu = \cos\theta$ where θ is the angle between the RE momentum and the magnetic axis. Figure 6.6 (A) presents the RE momentum space shown in 6.5 in E-μ coordinates.

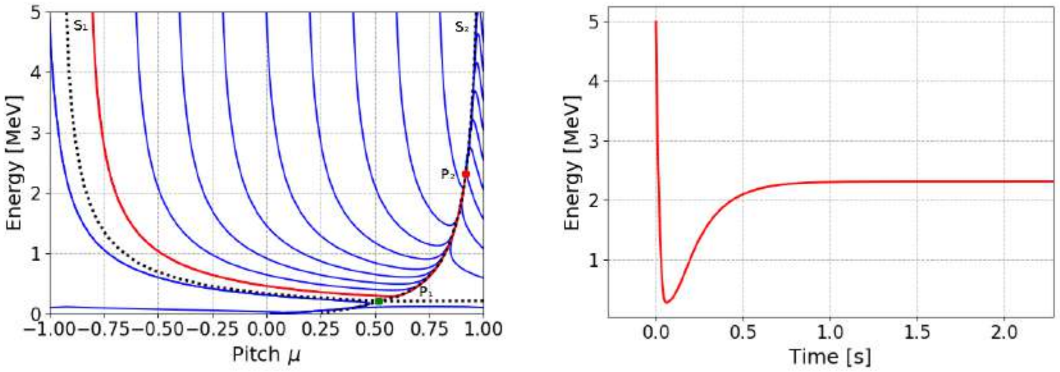

(A)

(B)

FIGURE 6.6: (A) RE E-μ space. The two separatrices are indicated by the dotted black lines. The green P_2 dot is the saddle point, while the red P_1 dot is the stable focus point. The blue lines denote the test particle trajectories. The red line shows the simulated trajectory of a test particle with initial values $E_0 = 5$ MeV and $\mu_0 = -\ 0.8$. (B) The test particle energy as a function of time.

In figure 6.6 (A) the sable focus point P_2 is characterized by a high positive pitch μ. This indicates the tendency of the RE test particle to become a strongly co-passing particle. The red line represent the simulated trajectory of a test particle with initial values $E_0 = 5$ MeV and $\mu_0 = -0.8$. These initial values are unrealistic and were chosen for only a demonstrative purpose. Figure 6.6 (B) shows the energy of the test particle as it moves on its trajectory towards the stable focus point P_2 as a function of time. The test particle rapidly loses its initial energy and rapidly aligns its momentum to the magnetic field direction in approximately 50 ms. After that, the test particle gradually gains energy and pitch angle in a few hundreds of milliseconds.

The test particle showed in figure 6.6 moves along a trajectory in a stationary E-μ space, but if the plasma characteristics that determine the E-μ space change in time, the space should adjust accordingly.

In the test particle model, there are several input parameters that determine the E-μ space, namely the magnetic field intensity B_0, the radial position of the test particle R_0, the electron density n_e, the loop voltage V_{loop} the atomic number of the background plasma species Z and the Coulomb logarithm $\log \Lambda$. All of them could potentially change throughout the RE phase of the discharge. The test particle model was adjusted to simulate the test particle trajectory in a time-dependent momentum space by including the time evolution of these input parameters.

Figure 6.7 presents a comparison between the maximum runaway energy E^*_{RE} and the expected value computed using the test particle model for AUG discharge #35889. The initial coordinates of the test particle are $E_0 = 7.944$ MeV and $\mu_0 = +0.5$, where $E_0 = E^*_{RE}$. The E-μ space is computed from the measured AUG plasma parameters with a time resolution of 0.1 ms. The radial position of the magnetic axis is used as a proxy for the radial position of the test particle.

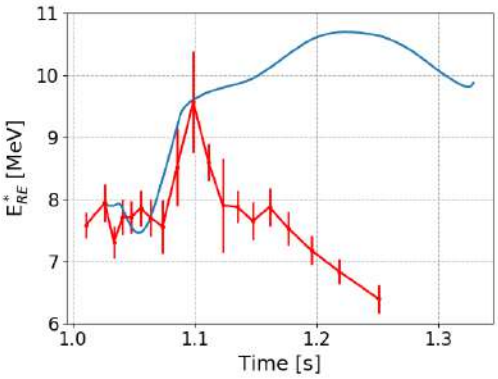

FIGURE 6.7: A comparison between the measured E^*_{RE} (red) and the relative test particle model (blue) for AUG discharge #35889.

Initially, the test particle energy is in good agreement with the measured E^*_{RE}. After t = 1.1 s the two curves diverge, with the test particle energy slowly increasing up to almost 11 MeV and the measured E^*_{RE} decreasing to approximately 6.5 MeV.

Similar results with a partial agreement between the two curves were achieved also for the other AUG discharges. This indicates that this simple test particle model presents some limitations. The discrepancy in the two curves of figure 6.7 could be explained by the fact that E^*_{RE} refers to the runaway electron distribution and therefore is subject to source and sink terms that are not included in the simple test particle model. Further development is needed to address the current limitations and improve the agreement between the measured data and the model predictions.

Chapter 7

Runaway Electrons at the Joint European Torus

7.1 Experiments Overview

Several experiments were conducted throughout the years at the Joint European Torus (JET) to study different aspects of the runaway electron physics. The results presented in this chapter refer to 2019 discharges of the M18-36 experiment: Runaway suppression with the SPI.

In this experiment the use of the shattered pellet injection (SPI) is investigated as RE suppression technique [17, 18, 19]. The working principle of this technique is analogous to the massive gas injection (MGI) [12, 13, 14, 15, 16]: a fast increase of the electron density of the post disruption plasma is used to suppress the RE beam through collisional drag forces [11]. In both techniques, this is achieved by introducing a very large quantity of additional target material in the post-disruption plasma. High-Z materials, such as argon or neon, are preferred for the higher number of electrons per atom. Low-Z materials, such as deuterium, are also considered to avoid the introduction of high Z impurities in the machine that are usually hard to extract after the RE suppression and can pollute the vessel.

MGI delivers the target material by puffing a large quantity of gas into the background plasma. A poor gas mixing efficiency can cause an inefficient penetration of the target material into the inner part of the background plasma. To avoid this problem the shatter pellet injection technique was designed. SPI launches the target material as a solid cryogenic pellet directly into the background plasma core increasing the target material penetration. The pellet is shattered right before entering the vacuum vessel to increase the assimilation of the fragments and to avoid damage to the in-vessel components. This mitigation technique is currently the primary injection scheme for the ITER Disruption Mitigation System [20].

The main goals of the M18-36 experiments are to study the efficacy of SPI to suppress a fully-developed runaway electron beam, to estimate the dependence of the SPI efficiency on background plasma characteristics and on the beam position with respect to the shard plume geometry, to measure the ablation and penetration of

SPI shards into RE beams in the runaway plateau and to characterize the suppression efficacy as a function of SPI injection species and quantity.

Bremsstrahlung radiation emitted by runaway electrons during the M18-36 experiments was measured using the two HXR spectrometers KM6S1 and KM6T. The two identical detectors are made by a large 3" x 6" $LaBr_3$:Ce scintillator crystal coupled with a PMT [84, 85]. KM6S1 is placed along a radial vertical line of sight that passes through the centre of the vacuum vessel. KM6T is placed along a tangential view line, near the machine mid-plane.

7.1.1 Discharge List

Table 7.1 presents a list of the M18-36 discharges analyzed using the Tikhonov Regularization method. A summary of the analysis results is given in section 7.2.

JET discharge #95125 is the reference shot. A runaway beam of approximately 750 kA was generated at t = 48.8 s by an Ar MGI. No secondary injection was used to terminate the beam. As a consequence, the total duration of the RE phase was approximately 1 s. In the other discharges listed in table 7.1 a secondary injection was used to suppress the RE beam. In table 7.1 MGIs are indicated by a single asterisk (*) while SPIs by a double asterisk (**). Three main target species were investigated during these experiments: deuterium, argon and neon. In JET discharges #95727 and #95729 a third injection of a cryogenic neon pellet was employed right after the deuterium SPI. Finally, in discharge #95776 a cryogenic deuterium pellet containing 20% neon was used to suppress the RE beam.

JET Discharge #	Trigger Injection		Second Injection		Third Injection	
	Species	Timing [s]	Species	Timing [s]	Species	Timing [s]
95125	Ar*	48.0	-	-	-	-
95131	Ar*	48.0	Ar**	48.4	-	-
95132	Ar*	48.0	Ar**	48.4	-	-
95133	Ar*	48.0	Ar**	48.4	-	-
95134	Ar*	48.0	Ar*	48.4	-	-
95135	Ar*	48.0	D2**	48.4	-	-
95136	Ar*	48.0	Ne**	48.4	-	-
95727	Ar*	48.0	D2**	48.4	Ne**	48.5
95729	Ar*	48.0	D2**	48.4	Ne**	48.5
95733	Ar*	48.0	D2**	48.4	-	-
95774	Ar*	48.0	D2**	48.05	-	-
95776	Ar*	48.0	D2+20%Ne**	48.4	-	-

TABLE 7.1: A list of the M18-36 JET discharges analyzed. A single asterisk (*) near the target species indicates a MGI while a double asterisk (**) an SPI.

7.2 Analysis of the JET RE Experiments

7.2.1 Reconstruction of the RE Energy Distribution Function

JET discharge #95125 was used as a reference case for the SPI experiments. After the initial argon MGI at t = 48.0 s used to trigger the disruption no additional injection was made. This unsuppressed RE beam lasted approximately 1 s. Tikhonov regularization was used to recover the RE energy distribution from the measured HXR spectra. In figure 7.1 the average RE energy $< E_{RE} >$ (panels (A) and (B) and the RE maximum energy E^*_{RE} (panels (C) and (D)) are plotted as function of time. Left side panels (A) and (C) refer to the data collected with the vertical spectrometer KM6S1 while (B) and (D) present the results obtained from the tangential KM6T detector.

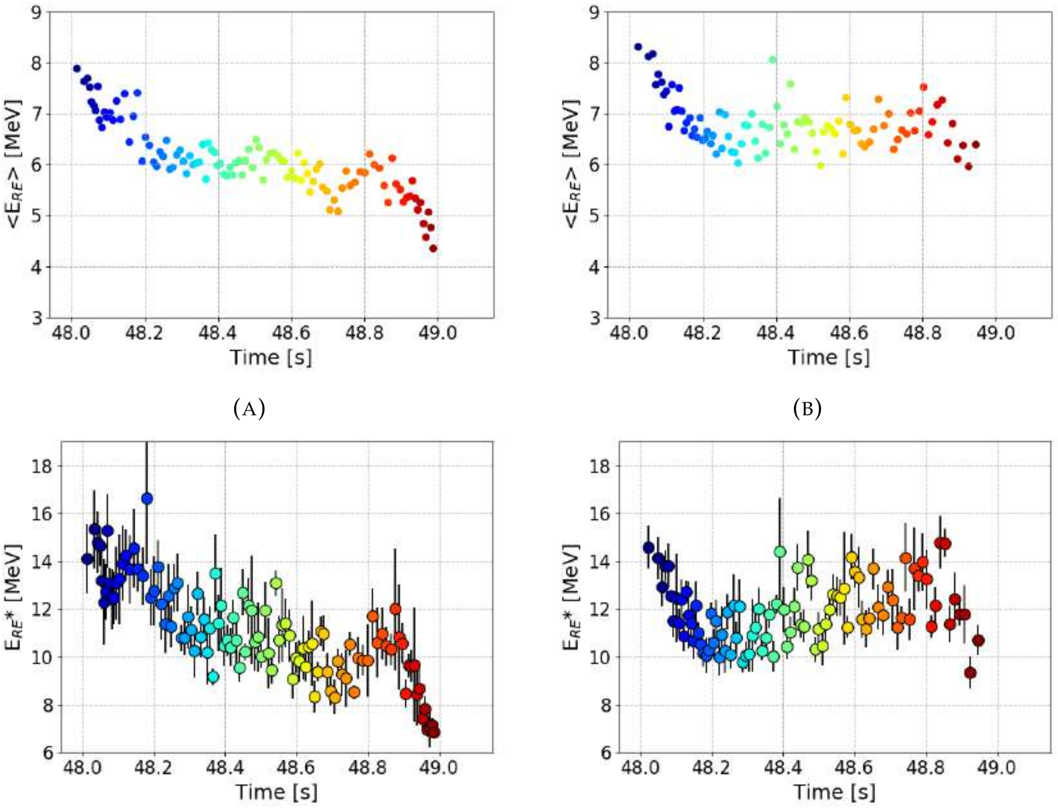

(A)

(B)

(C)

(D)

FIGURE 7.1: Average RE energy of the reconstructed RE energy distribution function of JET discharge #95125 for the vertical KM6S1 spectrometer (A) and the tangential KM6T spectrometer (B). Maximum RE energy of the reconstructed RE energy distribution function for the vertical KM6S1 spectrometer (C) and the tangential KM6T spectrometer (D).

At the beginning of the RE phase, the average RE energy reconstructed for both spectrometers has a similar behaviour. The initial value of 8 MeV rapidly decreased in the span of approximately 200 ms reaching a plateau value of approximately 6 MeV for KM6S1 and 6.5 MeV for KM6T. The RE beam kept this plateau value for approximately 600 ms. At the end of the discharge, the energy rapidly drops to 4

MeV in approximately 200 ms before the RE beam is lost for the KM6S1 detector. On the other hand, the average energy measured by the KM6T spectrometer seems to slightly increase before starting to fall down. The RE beam moved out of the tangential line of sight earlier than the vertical one and therefore the very last points of the average energy are missing for detector KM6T.

The time trace of the maximum energy E^*_{RE} computed for both spectrometers closely resemble the shape of the respective average energy. The initial value of E^*_{RE} at the RE beam creation is approximately 14 MeV for both spectrometers. The plateau maximum energy is approximately 11 MeV. The energy increase measured by the KM6T spectrometer is more gradual for E^*_{RE} rather than for $< E_{RE} >$. At the end of the RE phase, the maximum energy of the KM6S1 spectrometer rapidly decreases to approximately 5 MeV.

The difference in the reconstructed RE energy time traces for the two spectrometers can be ascribed to the sampling of different regions of the runaway beam. A discussion on the implication of these geometry effects can be found in the next subsection 7.2.2.

One of the most noticeable effects of a second injection of deuterium is to drastically reduce the plasma Z_{eff} and causing a significant reduction of the bremsstrahlung emission. This effect is evident in JET discharge #95135 where a deuterium SPI was launched in the Ar post-disruption plasma at t = 48.4 s to suppress the RE beam. After the second injection, the RE beam lasted up to approximately t = 48.65 s.

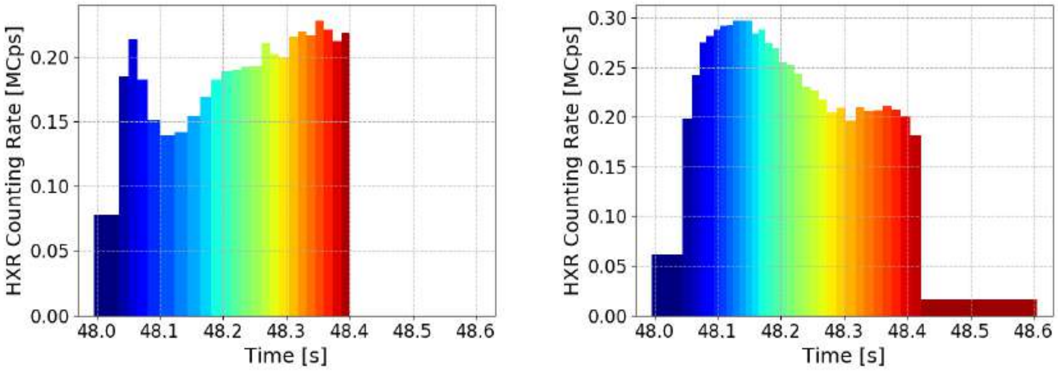

(A) (B)

FIGURE 7.2: HXR counting rates for JET discharge #95135 measured by the vertical KM6S1 (A) and the tangential KM6T (B) spectrometers. Each bin contains 3000 HXR counts.

Figure 7.2 shows the HXR counting rate during the RE phase of discharge #95135 for the vertical KM6S1 (A) and the tangential KM6T (B) spectrometers. In the first part of the RE phase, the RE beam is interacting with the argon background plasma. The resulting background emission is sufficiently high and a moderate HXR counting rate in the order of approximately 200 kCps can be appreciated in both spectrometers. After the deuterium SPI the HXR counting rate is drastically reduced by one order of magnitude.

The system time resolution is intrinsically determined by the HXR count statistics. To study the time evolution of the RE energy distribution function, the HXR events collected during the discharges are divided in different time intervals. The events contained in each interval are integrated and the RE energy distribution function is reconstructed by the resulting HXR spectrum. In this analysis, the time steps of these time intervals are chosen so that each bin contains the same number of HXR events. Figure 7.2 shows the time intervals for JET discharge #95135. At is clearly visible the decrease in HXR counting rates caused by the deuterium purge significantly affects the event statistics. After the deuterium SPI there are barely enough counts for a single reconstruction for the KM6T spectrometer and not enough for the KM6S1.

Figure 7.3 shows the average and maximum RE energies computed from the reconstructed energy distribution functions. The lack of events after the deuterium SPI hinder the ability to reconstruct the RE beam behaviour.

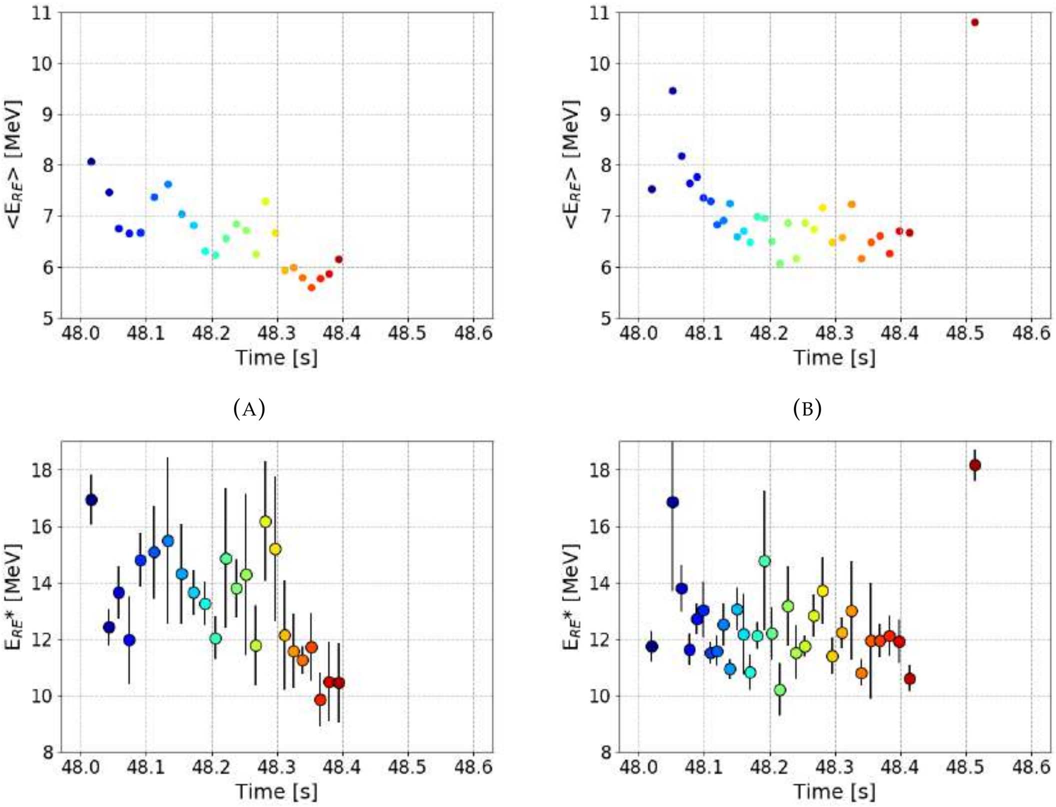

(A)

(B)

(C)

(D)

FIGURE 7.3: Average RE energy of the reconstructed RE energy distribution function of JET discharge #95135 for the vertical KM6S1 spectrometer (A) and the tangential KM6T spectrometer (B). Maximum RE energy of the reconstructed RE energy distribution function for the vertical KM6S1 spectrometer (C) and the tangential KM6T spectrometer (D).

7.2.2 Reconstruction of the RE Current

The electrical current carried by the runaway electrons, I_{RE}, is a useful parameter to describe the beam dynamics. The runaway current can be expressed as

$$I_{RE} = \int \boldsymbol{j_{RE}} \cdot \boldsymbol{\hat{n}} \, dA = < j_{RE} > A_{RE} \tag{7.1}$$

where j_{RE} is the runaway electron current density, dA is the unit area, $\hat{n}$ is the unit area normal, $< j_{RE} >$ is the average runaway electron current density and A_{RE} is the cross-section area of the RE beam. The RE current density is given by

$$\boldsymbol{j_{RE}} = q_e \int \boldsymbol{v} \, f_{RE}(\boldsymbol{v}) \, d^3v = q_e \, n_{RE} \int \boldsymbol{v} \, \hat{f}_{RE}(\boldsymbol{v}) \, d^3v \tag{7.2}$$

where q_e is the electron charge, v is the velocity and $f_{RE}(v)$ is the RE distribution function in the velocity space. $\hat{f}_{RE}(v)$ represents the normalized distribution function and n_{RE} the runaway electron density defined as

$$n_{RE} = \int f_{RE}(\boldsymbol{v}) \, d^3v \tag{7.3}$$

Under the assumption of strongly passing RE electrons, j_{RE} can be expressed as

$$j_{RE} = q_e \, n_{RE} \int c \, \frac{\sqrt{E^2 + 2m_e c^2 E}}{E + m_e c^2} \, \hat{f}_{RE}(E) \, dE \tag{7.4}$$

where c is the speed of light in vacuum, m_e is the electron rest mass and $\hat{f}_{RE}(E)$ is the normalised runaway electron energy distribution function. The runaway current can be computed from the energy distribution function as

$$I_{RE} = q_e \, n_{RE} \, A_{RE} \int c \, \frac{\sqrt{E^2 + 2m_e c^2 E}}{E + m_e c^2} \, \hat{f}_{RE}(E) \, dE. \tag{7.5}$$

The recovered runaway electron energy distribution function can be used in 7.5 to compute the runaway electron current. As explained in section 5.2.1, the runaway electron energy distribution function reconstructed using the inversion techniques is normalized by the target density and the solid angle of the view line. As a result, equation 7.5 takes the discretized form

$$I_{RE} = q_e \, n_{RE} \, n_T \, A_{RE} \, d\Omega \, \frac{1}{\Delta t} \sum_{i=1}^{N} c \, \frac{\sqrt{E_i^2 + 2m_e c^2 E_i}}{E_i + m_e c^2} \, \hat{F}_{RE}(E_i) \, \Delta E. \tag{7.6}$$

where n_T is the target density, $d\Omega$ the solid angle, Δt is the spectrum integration time, i is the energy bin index and ΔE is the energy bin step. Equation 7.6 can be rewritten as

$$I_{RE} = K \, \frac{\Delta E}{\Delta t} \sum_{i=1}^{N} \frac{\sqrt{E_i^2 + 2m_e c^2 E_i}}{E_i + m_e c^2} \, \hat{F}_{RE}(E_i) \tag{7.7}$$

where $K = (q_e\, c\, d\Omega)\,(n_{RE}\, n_T\, A_{RE})$. The terms in the first parenthesis of K are constants specific to each detector while the terms in the second parenthesis are related to the RE physics and can change throughout the discharge.

The expected RE current was computed using the reconstructed energy distribution spectra for the discharges listed in table 7.1. Since the measurement of the target density n_T is difficult during the post-disruption phase of the discharge, the K parameter was chosen so that the maximum of the reconstructed runaway current would match the runaway current measured by the continuous external Rogowski coils and then kept constant throughout the discharge.

Figure 7.4 shows the RE current reconstructed for the reference discharge #95125. The left panels (A) and (C) shows the HXR counting rate of the vertical spectrometer (KM6S1) and of the tangential one (KM6T) respectively. The right side panels (B) and (D) shows a comparison between the measured RE current (blue) and the one obtained from the reconstructed RE energy distribution spectra (red).

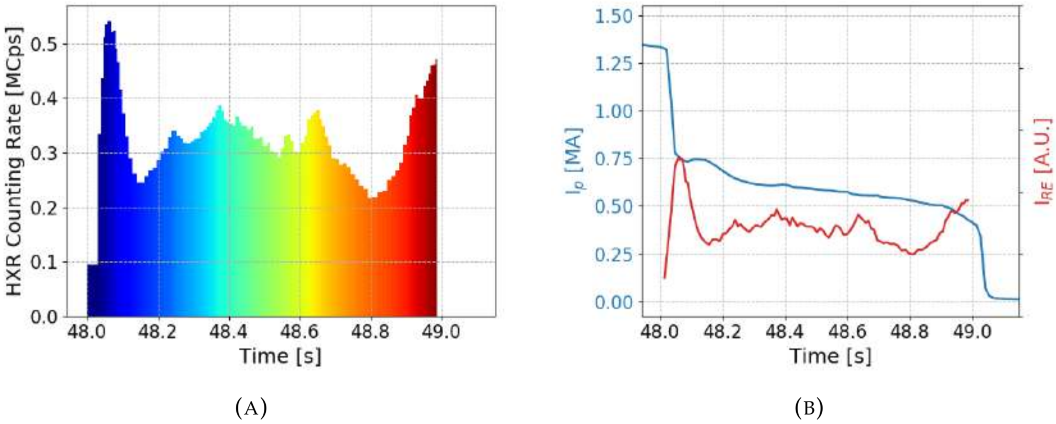

(A) (B)

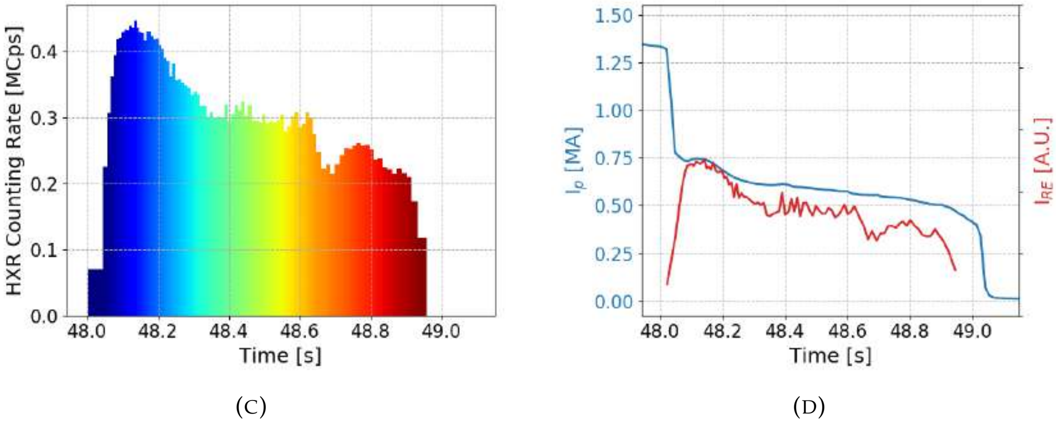

(C) (D)

FIGURE 7.4: Data collected from the JET discharge #95125. Panels (A) and (C) present, respectively, the HXR counting rate for the vertical KM6S and the tangential KM6T spectrometers. The left panels present a comparison between the measured RE current (blue) and the RE current reconstructed from the RE energy distribution function (red) for the vertical (B) and tangential spectrometer (D).

The runaway electron current reconstructed from the measured HXR spectrum is largely influenced by the HXR counting rate. A correlation between the left side graphs and the reconstructed RE current is clearly visible. The RE current reconstructed from the data collected by the tangential KM6T spectrometer has a reasonable agreement with the measured RE current. The RE current obtained from the vertical KM6S1 detector has a worse agreement with the experimental data. This effect can be explained with the geometrical shift of the RE beam relative to the spectrometers line of sights.

Figure 7.5 shows the position of the magnetic axis during the discharge. The magnetic axis position is here used as a proxy for the RE beam centre. The magnetic axis position along the JET poloidal cross-section is plotted in the left panel. The colour of the dots represents the time coordinate. The dotted lines roughly represent the vertical and tangential detector view lines. The black "x" indicates the machine major radius position. The top right graph represents the radial position of the magnetic axis as a function of time. The dotted lines indicate the vertical KM6S1 detector view line and the solid line the machine major axis. The bottom right panel shows the vertical position of the magnetic axis as a function of time. The dotted lines represent the tangential KM6S1 detector view line and the solid line the machine mid-plane position. The same colour coding is used in all images.

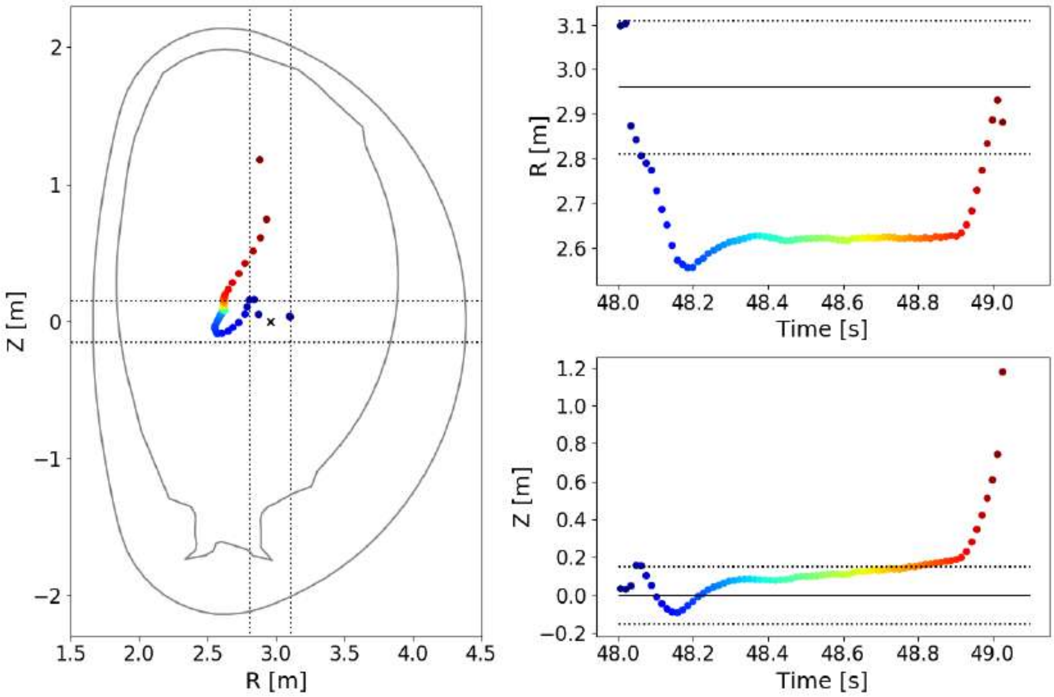

FIGURE 7.5: Position of the magnetic axis during the RE phase of discharge #95125. The color coding represent the time coordinate. Spectrometers line of sights are indicated by dotted lines.

As shown in figure 7.5, right after its generation the RE beam moves towards the high field side of the machine. This is caused by a deliberate increase of the P4 PF coil current aimed at providing additional flux to the RE beam. As a result of the shift the beam partially moves out of the vertical line of sight. On the other hand, the RE beam remains inside the tangential line of sight for almost the entire duration of the discharge. This behaviour is most evident in the sharp decrease of HXR counting rate observed by the vertical spectrometer in the first 200 ms of the RE phase that is not present in the tangential spectrometer data. This initial reduction of the HXR counting rate is reflected also in the RE current reconstructed from the vertical spectrometer data. This feature is present in all of the discharges presented in table 7.1 and it is always linked with an initial inward shift of the runaway beam towards the high field side.

It is clear that geometrical effects can hinder the reconstruction of the runaway current due to a partial sampling of the beam cross-section. To this end, RE data collected by the JET Gamma Camera Upgrade with its higher spatial resolution can offer a significant improvement. With its 19 lines of sights covering uniformly the machine poloidal cross-section, the GCU allows for a more complete sampling of the RE beam and therefore a better reconstruction of the current profile. Moreover, combining inversion techniques with tomographic methods, a spatial reconstruction of the RE energy distribution function could be possible. Analysis of the GCU RE experiments data is currently underway and preliminary results are encouraging.

The same analysis presented for JET discharge #95125 was also conducted for the remaining pulses listed in table 7.1. The results obtained for these discharges are similar to the ones of JET discharge #95132. This pulse is presented here to showcase the effectiveness and limitations of this analysis method.

Figure 7.6 shows the results obtained for JET discharge #95132. The left side panels show the HXR counting rates for the vertical KM6S1 (A) and for the tangential KM6T (C) spectrometers. The right side panels show a comparison between the measured runaway electron current and the one reconstructed from the RE energy distribution functions for the vertical KM6S1 (B) and the tangential KM6T (D) spectrometers. The dashed black line indicates the time of the second injection, in this case, an Ar SPI.

As seen in JET discharge #95125, right after its generation the RE beam moves towards the high field side and partially moves out from the vertical spectrometer line of sight. This causes the reduction of HXR counts in the first 200 ms of the RE phase visible in 7.6 (A). This reduction is also reflected in the reconstructed RE current shown in figure 7.6 (B). The initial inward dynamic of the RE beam can be appreciated in figure 7.7 where the magnetic axis position is plotted as a proxy of the RE beam centre position. On the other hand, data collected from the tangential KM6T spectrometer allows for a good reconstruction of the RE plasma current with good agreement with the experimental data.

Figures 7.6 (B) and (D) show the reconstructed RE current from the RE beam generation up to the Ar SPI injection. As previously discussed, in this analysis the K parameter in equation 7.7 is kept constant throughout the discharge. This assumes that the target density n_T, the runaway electron density n_{RE} and the RE beam

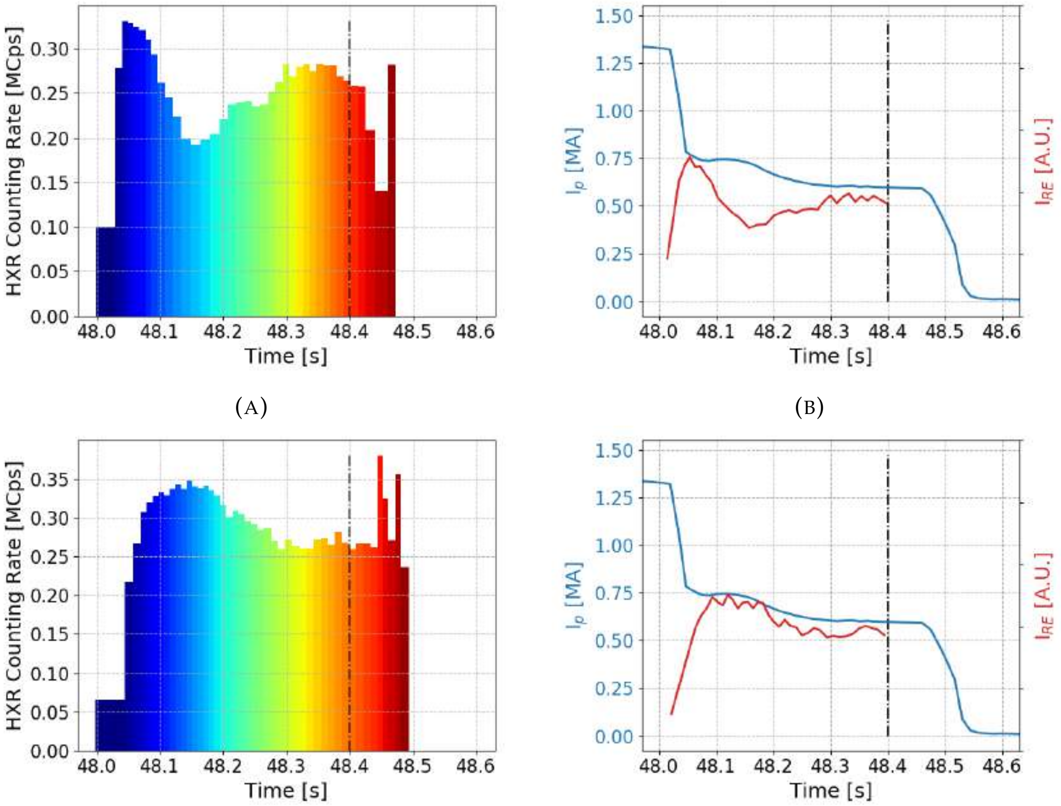

(A) (B)

(C) (D)

FIGURE 7.6: Data collected from the JET discharge #95132. Panels (A) and (C) present respectively the HXR counting rate for the vertical KM6S and the tangential KM6T spectrometers. The left panels present a comparison between the measured RE current (blue) and the RE current reconstructed from the RE energy distribution function (red) for the vertical (B) and tangential spectrometer (D). The dashed line represent the time of the Ar SPI.

cross-sectional area A_{RE} are constant for the entire duration of the RE phase. This assumption is clearly broken when a massive quantity of additional gas is injected in the post disruption plasma trough an MGI or an SPI. The fast evolution of K after the second injection makes the reconstruction of the RE current unreliable.

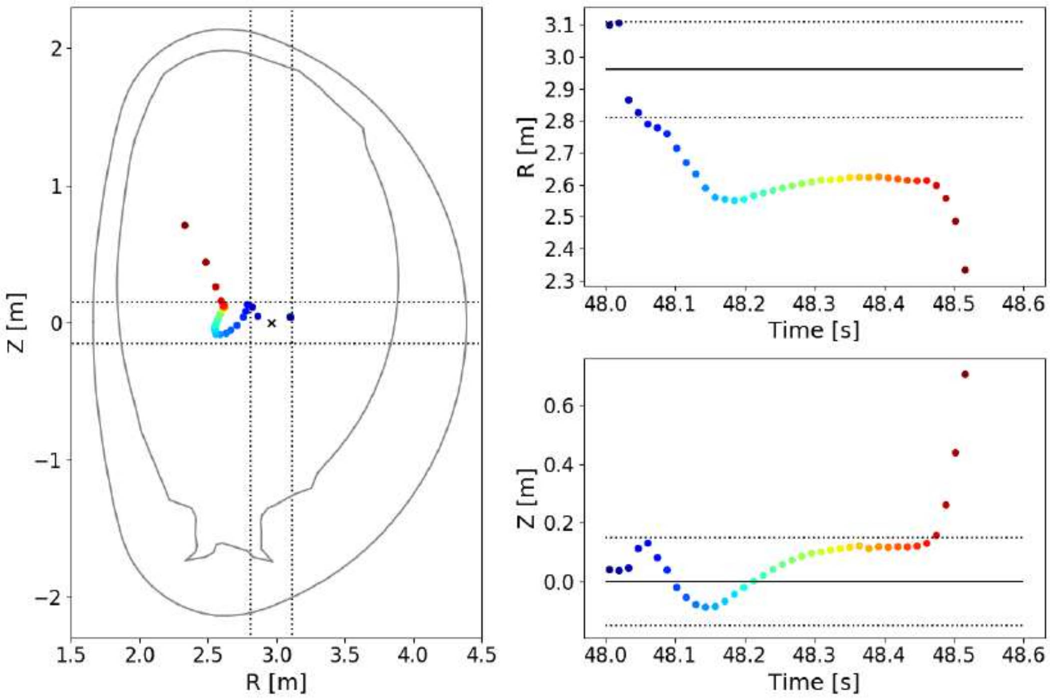

FIGURE 7.7: Position of the magnetic axis during the RE phase of discharge #95132. The color coding represent the time coordinate. Spectrometers line of sights are indicated by dotted lines.

Conclusions

The generation of uncontrolled runaway electron beams is a major threat to the success of next-generation high-current large tokamaks, such as ITER. A thorough understanding of runaway electron physics is the cornerstone of any successful prediction, avoidance or mitigation technique. To this end, experimental results are crucial to validate current models and further understating of this phenomenon.

The post-disruption phase of a plasma is characterized by a fast and drastic evolution of many of its key parameters. Plasma degree of ionization, temperature, density, current, size and position inside the vessel can rapidly change in few milliseconds. In addition, mitigation techniques such as massive gas injection and shattered pellet injection can accentuate the evolution of these parameters and drastically change the plasma composition. Quantitative measures of these rapidly evolving systems are extremely challenging, but recent development in both diagnostic capabilities and data analysis techniques opened unprecedented opportunities in the characterization of the post-disruption runaway electron generation.

When runaway electrons interact with the post-disruption plasma, bremsstrahlung is emitted. This radiation carries valuable information on the runaway electron energy distribution function. Accessing this data is crucial to assess the efficacy of mitigation techniques, to validate predictive models and to design tokamak in-vessel components. In the current quench phase of the disruption, runaway electrons can be accelerated to relativistic energies. As a consequence, bremsstrahlung radiation can be emitted in a very broad energy range, up to several MeV, in the hard X-Ray region. Measurement of the runaway electron bremsstrahlung in medium and large-sized tokamaks is challenging. This is caused by the extreme HXR fluxes, rapidly evolving behaviour and broad energy emission range typically associated with this radiation.

This thesis has contributed to the development of hard X-ray diagnostics optimized for runaway electron bremsstrahlung measurements.

A compact LYSO:Ce spectrometer with counting rate capabilities in excess of 1 MCps was developed to expand the detection range of the tokamak DIII-D Gamma Ray Imager system to include unquenched runaway electron scenarios. A silicon photomultiplier was chosen for this application to ensure a compact design suitable for the existing array configuration of the GSI system and to allow optimal operation under the strong magnetic fields caused by the close proximity to the tokamak. The prototype achieved a wide dynamic range in excess of 25 MeV and an energy resolution of approximately 9% at 661.7 keV, appropriate for runaway electron bremsstrahlung measurement. The LYSO:Ce prototype was tested at the DIII-D tokamak and proved to be 1000 times faster than the existent GRI BGO detector, expanding the diagnostic counting rate capability of approximately 3 orders of magnitude. The improved diagnostic capabilities contributed to the observation of novel correlations between the RE energy and the insurgence of kinetic instabilities during the current quench phase of a disruption.

The enhanced counting rates capabilities provided by the LYSO:Ce detector allowed to gather valuable information on the physics of the runaway electrons. Unfortunately, the HXR fluxes experienced by the detector at the GRI location proved in many cases to be too extreme even for this fast diagnostic. A new compact HXR spectrometer was developed to allow the GRI to sustain severe HXR fluxes up to one order of magnitude higher than the previous prototype. The new design was based on a smaller YAP:Ce scintillator crystal coupled with a silicon photomultiplier. The detector has a wide dynamic range in excess of 20 MeV, an energy resolution of approximately 9% at 661.7 keV and a counting rate capability in excess of 1 MCps. During testing, the detector showed promising results and it is now scheduled to be tested at the DIII-D tokamak in the next few months.

As part of this thesis, another novel hard X-ray spectrometer optimized for RE bremsstrahlung measurement was developed. The Runaway Electron GAmma-Ray Detection System (REGARDS) is a portable system designed to be deployed at different medium-sized tokamak for RE bremsstrahlung measurement. The detector is based on a LaBr3:Ce scintillator crystal coupled with a photomultiplier tube. The system offers a wide energy dynamic range for HXR spectroscopy with an upper bound in excess of 20 MeV and an energy resolution of approximately 3% at 661.7 keV. The counting rate capability of the system is in excess of 1 MCps. REGARDS was deployed at the tokamaks AUG and COMPASS during the MST1-T08 experimental campaign. During these experiments REGARDS provided HXR data with previously unavailable quality and allowed for a quantitative description of the bremsstrahlung spectrum during the harsh conditions of the runaway electron phase of the discharges.

This thesis also focuses on the problem of recovering the runaway electron distribution function from the bremsstrahlung measurements. This inversion problem is generally ill-posed, where many solutions could explain the same measured HXR spectrum within the experimental error.

A first-order Tikhonov regularization algorithm was used to reconstruct the runaway energy distribution function from the measurements performed at the tokamaks AUG and JET. The transfer matrix was computed using two numerical codes. GENESIS was used to model of the bremsstrahlung emission of the runaway electron beam interacting with different background plasma species while MCNP was employed to compute the response function of the HXR spectrometers employed at the different facilities. The runaway electron energy distribution functions obtained from the measured HXR spectra allow for a quantitative description of the runaway electron beam evolution throughout the discharges, providing valuable information to validate first-principle models and to evaluate the effectiveness of different runaway electron mitigation techniques such as massive gas injection, shattered pellet injection and magnetic resonant perturbation. A thorough analysis of the data collected at AUG and JET is near completion.

A test particle model was implemented to compare the evolution of the reconstructed RE energy to the expected value computed form the post-disruption plasma parameters. This model showed some partial agreement with the data and some limitations. In general, this simple model fails to accurately predict the behaviour of the reconstructed runaway electron energy. The complexity of the model should be increased to achieve a better agreement with experimental data.

A lot of progress was made within this work and a lot of progress still has to be done. REGARDS is going to be deployed again at AUG and COMPASS for future MST1-T08 experiments and it will continue to provide valuable information on runaway electron physics.

The new YAP:Ce prototype is now close to being tested at the DIII-D tokamak. Its greater capability in sustaining higher HXR fluxes could substantially expand the GRI ability to perform quantitative measurement for RE scenarios that were previously inaccessible for the old slower detectors. This could potentially further expand the investigation in the interplay between runaway electrons and kinetic instabilities.

JET experiments highlighted the importance that RE beam position during the discharge plays for the measured HXR spectra, especially when the beam is only partially visible by the detector collimated line of sight. To this end, array configurations of HXR spectrometers, such as the GRI or the GCU, potentially offer a more complete sampling of the runaway beam geometry and could improve the quality of the reconstructions. Moreover, spatially resolved runaway electron energy distribution functions could be reconstructed using these new array systems paired with tomographic techniques.

The test particle model could be modified into a Monte Carlo simulation of the entire runaway electron distribution. Moreover, source and drain components could be included to represent runaway electron generation and losses, with the goal to achieve a simple but reliable model of the evolution of the runaway beam energy throughout the discharge.

Finally, a thorough analysis of the data collected at AUG and JET with the analysis techniques described in this thesis is on its way to completion. Results from this analysis will foster the understanding of the efficacy of mitigation techniques and will contribute to guide the direction of further research.

"The Road goes ever on and on
Down from the door where it began.
Now far ahead the Road has gone,
And I must follow, if I can,
Pursuing it with eager feet,
Until it joins some larger way
Where many paths and errands meet.
And whither then? I cannot say."

J.R.R. Tolkien

Part IV

Papers

REVIEW OF SCIENTIFIC INSTRUMENTS **89**, 10I134 (2018)

Development of a new compact gamma-ray spectrometer optimised for runaway electron measurements

A. Dal Molin,[1,a)] L. Martinelli,[1] M. Nocente,[1,2] D. Rigamonti,[2] A. Abba,[3] L. Giacomelli,[2]
G. Gorini,[1,2] A. Lvovskiy,[4] A. Muraro,[2] M. Tardocchi,[2] and JET Contributors[5,b)]
[1]*Dipartimento di Fisica "G. Occhialini," Università degli Studi di Milano-Bicocca, Milano, Italy*
[2]*Istituto di Fisica del Plasma "P. Caldirola," CNR, Milano, Italy*
[3]*Nuclear Instruments, Lambrugo, Italy*
[4]*Oak Ridge Associated Universities, Oak Ridge, Tennessee 37831, USA*
[5]*EUROfusion Consortium, JET, Culham Science Centre, Abingdon, United Kingdom*

(Presented 19 April 2018; received 5 May 2018; accepted 25 June 2018;
published online 12 October 2018)

A new compact gamma-ray spectrometer was developed in order to optimise the measurement of bremsstrahlung radiation emitted from runaway electrons in the MeV range. The detector is based on a cerium doped lutetium-yttrium oxyorthosilicate (LYSO:Ce) scintillator coupled to a silicon photomultiplier and is insensitive to magnetic fields. A dedicated electronic board was developed to optimise the signal readout as well as for online control of the device. The detector combines a dynamic range up to 10 MeV with moderate energy non-linearity, counting rate capabilities in excess of 1 MHz, and an energy resolution that extrapolates to a few % in the MeV range, thus meeting the requirements for its application to runaway electron studies by bremsstrahlung measurements in the gamma-ray energy range. https://doi.org/10.1063/1.5038803

I. INTRODUCTION

The ITER project is one of the most ambitious international endeavors of this century. It aims to demonstrate the production of fusion power with a ten-fold gain. ITER will also try to prove that high performance plasma operation can be reliably and safely achieved. A major obstacle in this effort could be represented by the damage caused to the first wall materials by uncontrolled runaway electron beams. As a result, the study and characterization of the runaway electron population during plasma discharges have become one of the most prominent topics of the fusion research field.[1–3]

Gamma-ray spectroscopy, which is among the primary tools to investigate fast ion physics,[4–8] has also been recently applied to studies of runaway electrons in high temperature plasmas,[3,9–11] also in view of ITER.[12] Gamma-rays are produced from bremsstrahlung emission when the runaway electron population interacts either with the plasma bulk or with the tokamak plasma facing components. By measuring the bremsstrahlung emission, it is possible to infer information on the runaway electrons. These types of measurements pose several requirements and restrictions to the detector. First of all, the spectrometer must have a high counting rate capability (>1 MHz) to withstand the intense photon flux of runaway electron bremsstrahlung emission. The spectrometer should also be able to detect gamma-rays in a wide range of energies, up to several MeV. Moreover, the intense magnetic fields of a tokamak prevent the use of traditional photodetectors such as photomultiplier tubes (PMTs). Finally, the detector has to be compact to allow the implementation of the detector array configuration required for the tomographic reconstruction of the runaway electron spatial distribution.

These requirements dictate the development of a specific gamma-ray spectrometer optimised for the study of runaway electron bremsstrahlung emission, which is discussed in this paper.

II. THE DETECTOR

The detector is based on a cerium doped lutetium-yttrium oxyorthosilicate (LYSO:Ce) scintillator crystal coupled with a silicon photomultiplier (SiPM). The crystal is a rectangular parallelepiped 13 mm × 13 mm × 50 mm long manufactured by Saint-Gobain.

The LYSO scintillator is commonly used in both high energy physics and nuclear medicine applications.[13] Its properties can also be useful for measurements of gamma-ray emission from fusion plasmas. In particular, the material shows high stopping power due to its high density (88% of 1 MeV gammas are absorbed in 45.6 mm of material), good light yield, and high detection efficiency in the gamma-ray range.[14] Moreover, its fast scintillation decay time (∼36 ns) makes this scintillator suitable for high flux scenarios where high counting rate capability is necessary. Due to the presence of ^{176}Lu, a beta emitter, LYSO crystals display a characteristic intrinsic background radioactivity at a typical counting rate of 39 cps/g. The energy range of these events covers an interval between 88 keV and 1.2 MeV. This intrinsic background radiation does not interfere with the measurement of high rate events but can be used to verify the detector stability between two plasma discharges. Finally, LYSO crystals are

---

Note: Paper published as part of the Proceedings of the 22nd Topical Conference on High-Temperature Plasma Diagnostics, San Diego, California, April 2018.

a) Author to whom correspondence should be addressed: a.dalmolin@campus.unimib.it

b) See the author's list of X. Litaudon *et al.*, Nucl. Fusion **57**, 102001 (2017).

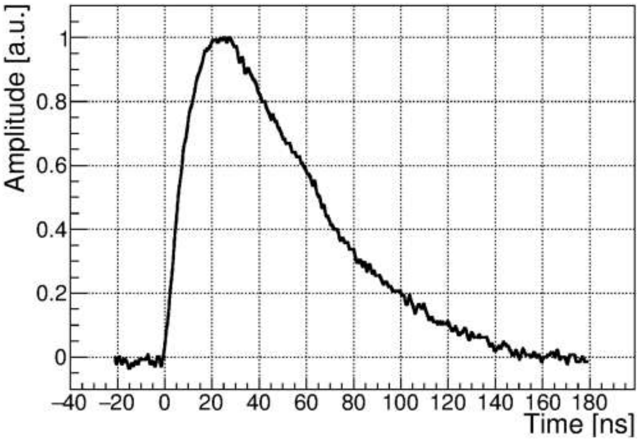

FIG. 1. Output signal of the LYSO crystal coupled with the SiPM and the dedicated readout electronics.

radiation hard and non-hygroscopic, making them practical to handle.

The LYSO crystal is coupled to the silicon photo-multiplier (model S13361-3050NE-04 by Hamamatsu[15]) along one of its square faces. SiPMs[16] are solid state photodetectors made up by arrays of avalanche photodiodes (APDs) operating in Geiger mode. This relatively new type of light detector offers several advantages with respect to the more standard photo-multiplier tube (PMT). First of all, the gain of a SiPM detector is comparable to PMT typical values with the advantage of being insensitive to magnetic fields. This feature is of extreme importance for detectors positioned close to the tokamak intense magnetic fields. Other positive characteristics of these devices are their compactness, their relative low bias operation voltage (~55 V), and their robustness to radiation damage.[17] Despite the continuous progress made in this technology, SiPMs still show gain shifts due to temperature changes and limited energy linearity due to their finite number of APDs. Fortunately, both limitations can be corrected for with dedicated procedures.

Finally, a dedicated electronic readout circuit was developed for this detector. The original design, proposed in Ref. 15 and subsequently improved in Refs. 18–20, was implemented to achieve fast signals (see Fig. 1) in order to reach high counting rate capability and minimize pile-up events. The electronic board was further improved by adding active components to provide signal amplification and an on-line correction of gain shifts caused by temperature fluctuations.

Data presented in this work were collected using a digitizer with 14 bit resolution and a sampling rate of 500 MS/s (model DT5730 by CAEN). The pulse height was determined by measuring the area of the signal from the detector without any intermediate amplification stage.

The characterization of this detector was aimed to assess three major aspects: the energy resolution, the counting rate capability, and the non-linearity of the device.

III. ENERGY RESOLUTION

Energy resolution was measured using two radioactive sources, ^{60}Co (E_γ = 1173 keV and 1332 keV) and ^{137}Cs (E_γ = 661.7 keV), and two detectors, a LYSO crystal coupled with a PMT (model R9420-100-10 by Hamamatsu) and an identical LYSO crystal coupled with the SiPM and the dedicated readout electronics. The purpose of this procedure is to compare the performance of the proposed detector against a more traditional acquisition chain. The results of these measurements are summarized in Fig. 2 in terms of energy resolution, i.e., the ratio of the full width at half maximum and the peak position of the measured photo-peak.

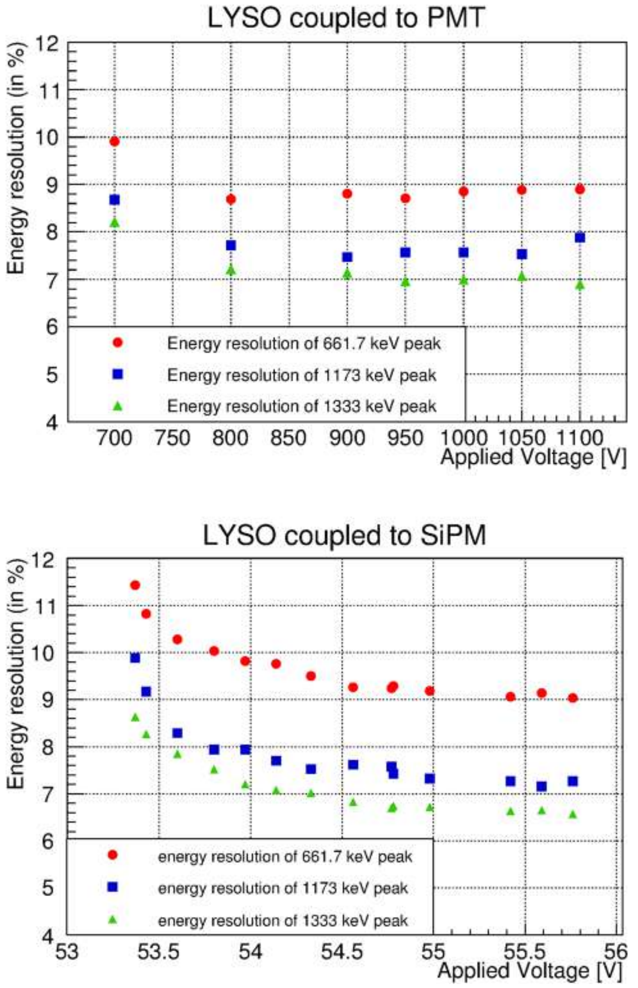

FIG. 2. Energy resolution of a LYSO crystal coupled to a PMT (top) and to a SiPM (bottom). Error bars are smaller than the size of the symbols.

There is an optimal operation voltage for both detectors at which the energy resolution is maximized. When the optimum is reached, the energy resolution is comparable and has a value of about 9% at 661.7 keV, as quoted by the crystal manufacturer.[14] Hence, with the SiPM coupling, we can obtain the same energy resolution results of a traditional PMT based acquisition chain, with the additional advantages of having a lower operating voltage and a more compact device insensitive to magnetic fields.

IV. MHZ COUNTING RATE CAPABILITY

At high counting rates, the signal current generated by the large amount of the SiPM ADP cells that are activated by gamma-ray detection can become significant. This relative large current generates a drop in the SiPM overvoltage and a consequent reduction in the detector gain, which produces a shift of the spectrum toward lower energies.[19]

A similar setup to the one described in Ref. 21 was used to measure the effect of these currents on the detector gain. The experimental setup consisted of two blue light-emitting diodes (LEDs) that can be fired independently from each other using a pulser (Keysight model 81150A). One LED was set to mock the light emission of the scintillation produced by a 3 MeV photon absorbed by the LYSO crystal. This LED was fired at a constant rate of 10 kHz and used as a reference signal. The other LED was set to mock the light emission produced by a lower energy photon interacting with the LYSO crystal. This LED was fired at different rates scanning an interval up to 1.25 MHz and used as perturbation. The SiPM was illuminated with the light coming from both LEDs using optical fibers.

In a typical measurement, data were collected over three time windows of ~6 s each. In the first window, only the reference LED is on. In the second time window, the perturbation LED is switched on at a set constant rate, causing an increase in the SiPM signal current and the downshift of the reference LED energy peak in the measured spectrum due to the gain drop. In the last time window, the perturbation LED is switched off and the reference LED energy peak returns to its original position in the spectrum. These measurements were repeated using two different gamma-ray equivalent energies for the perturbation LED, namely, 600 keV and 1.1 MeV. The results of these measurements are shown in Fig. 3.

The relative shift of the reference peak increases in a non-linear way with the rate of the perturbation. Moreover, the shift tends to be more significant if the SiPM applied voltage is increased. By almost doubling the equivalent energy of the perturbation signals, the relative shifts of the reference peak increases accordingly, thus confirming that this shift is indeed caused by the output currents. For a perturbation of approximately 600 keV and a rate of 500 kHz, the shift of the reference peak is below 1.5% showing a better performance than a previous detector based on coupling a SiPM with a LaBr$_3$ crystal.[18,19]

V. NON-LINEARITY

As the number of scintillation photons impinging on the SiPM approaches the total number of APD cells contained in the device, the probability that two individual photons interact with the same active pixel can be non-negligible. As a consequence, the second photon is not detected by the instrument, resulting in a non-proportionality of the output signal amplitude to the energy deposited in the crystal by the gamma-rays. This effect is the main cause of the photodetector non-linearity.

A dedicated experimental setup was designed to measure this effect. The operating parameters of a blue LED were set to mock up the scintillation of a LYSO crystal. The amplitude of the LED emission was changed to simulate different equivalent gamma-ray energies. The light emitted by the LED was split into two branches using optical fibers: One branch illuminated the LYSO crystal coupled with the SiPM, while the other carried light to an identical LYSO crystal coupled with a PMT. ^{60}Co and ^{137}Cs sources were used to calibrate the energy spectrum measured by the LYSO + SiPM detector, while ^{22}Na (E_γ = 511.0 keV and 1274.5 keV) was used to calibrate the LYSO + PMT spectrum. The LED emission amplitude was changed to mock up gamma-rays at different

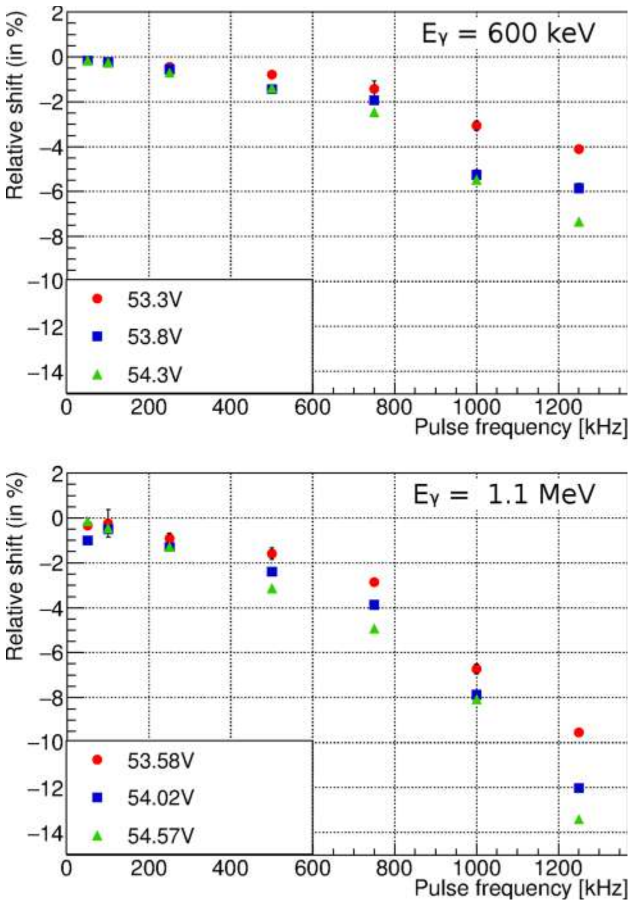

FIG. 3. Relative shift in the reference peak position due to high rate perturbation events. The top figure shows the shift caused by LED events at an equivalent gamma-ray energy of 600 keV. The shift caused by 1.1 MeV equivalent events is shown in the bottom figure. Different markers represent the different applied voltages.

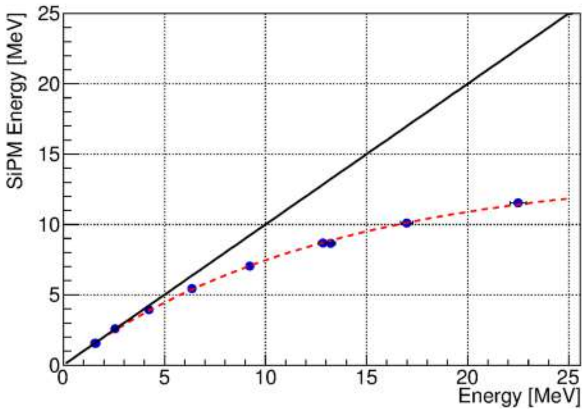

FIG. 4. Illustration of the non-linearity of the SiPM. The experimental points are represented by dots and are determined by measuring the peak position from an LED source at known equivalent energy with a LYSO coupled to a PMT and to a SiPM. The solid line indicates the expected results for a perfectly linear system. The dashed line is a fit of the experimental points.

energies within the interval of the PMT linear response. The SiPM non-linearity was computed by confronting the energies measured by the two different detectors after correcting the spectra for the optical factors introduced by the two different fibers.

The results are shown in Fig. 4. As expected, the detector behavior is linear at low energies. The detector saturates above 25 MeV for 1.5 V of overvoltage. At 10 MeV, the non-linearity of the detector is ~20%.

VI. CONCLUSIONS

A compact gamma-ray spectrometer based on a LYSO scintillator crystal coupled with a SiPM has been developed. Dedicated readout electronics has been implemented to obtain fast signals and other desirable features such as signal amplification and online temperature shift correction. Laboratory measurements showed good energy resolution of approximately 9% at 661.7 keV. This energy resolution is sufficient to measure the continuous spectrum of runaway electron bremsstrahlung emission in fusion plasmas. The detector showed counting rate capabilities in excess of 1 MHz, with an energy shift smaller than 1.5% for a perturbation of approximately 600 keV and a rate of 500 kHz. The energy non-linearity of the detector was also studied and a value of about 20% at 10 MeV for optimized settings was found, which can be corrected for by offline analysis.

In general, the SiPM based detector combines compact dimensions, insensitivity to magnetic fields, and MHz counting rate capabilities with only a moderate peak shift. It is therefore suitable for applications to runaway electron studies by gamma-ray bremsstrahlung measurements at MHz counting rates, particularly as part of multiple line of sight devices, such as gamma-ray cameras.

ACKNOWLEDGMENTS

This work has been carried out within the framework of the EUROfusion Consortium and has received funding from the Euratom research and training programme 2014-2018 under Grant Agreement No. 633053. The views and opinions expressed herein do not necessarily reflect those of the European Commission.

[1] M. Gobbin *et al.*, Plasma Phys. Controlled Fusion **60**, 014036 (2017).
[2] G. Pautasso *et al.*, Plasma Phys. Controlled Fusion **59**, 014046 (2016).
[3] C. Paz-Soldan *et al.*, Phys. Rev. Lett. **118**, 255002 (2017).
[4] M. Nocente, J. Källne, M. Salewski, M. Tardocchi, and G. Gorini, Nucl. Fusion **55**, 123009 (2015).
[5] M. Salewski *et al.*, Nucl. Fusion **55**, 093029 (2015).
[6] Ye. O. Kazakov *et al.*, Nat. Phys. **13**, 973–978 (2017).
[7] M. Salewski *et al.*, Nucl. Fusion **57**, 056001 (2017).
[8] M. Tardocchi, M. Nocente, and G. Gorini, Plasma Phys. Controlled Fusion **55**, 074014 (2013).
[9] A. E. Shevelev *et al.*, Nucl. Fusion **58**, 016034 (2018).
[10] M. Nocente *et al.*, Rev. Sci. Instrum. **89**, 10I124 (2018).
[11] D. C. Pace, C. M. Cooper, D. Taussig, N. W. Eidietis, E. M. Hollmann, V. Riso, M. A. Van Zeeland, and M. Watkins, Rev. Sci. Instrum. **87**, 043507 (2016).
[12] M. Nocente *et al.*, Nucl. Fusion **57**, 076016 (2017).
[13] R. Mao, L. Zhang, and R. Y. Zhu, J. Phys.: Conf. Ser. **293**, 012004 (2011).
[14] See https://www.crystals.saint-gobain.com/products/prelude-420-LYSO for information about LYSO:Ce characteristics.
[15] See https://www.hamamatsu.com/eu/en/product/category/3100/4004/4114/S13361-3050NE-04/index.html for information about SiPM characteristics.
[16] M. Nocente, A. Fazzi, M. Tardocchi, C. Cazzaniga, M. Lorenzoli, C. Pirovano, M. Rebai, C. Uboldi, V. Varoli, and G. Gorini, Rev. Sci. Instrum. **85**, 11E108 (2014).
[17] D. Rigamonti *et al.*, J. Instrum. **12**, C10007 (2017).
[18] D. Rigamonti *et al.*, Rev. Sci. Instrum. **87**, 11E717 (2016).
[19] M. Nocente *et al.*, Rev. Sci. Instrum. **87**, 11E714 (2016).
[20] D. Rigamonti *et al.*, Rev. Sci. Instrum. **89**, 10I116 (2018).
[21] M. Tardocchi *et al.*, Rev. Sci. Instrum. **79**, 10E524 (2008).

Development of gamma-ray spectrometers optimized for runaway electron bremsstrahlung emission in fusion devices

A. Dal Molin[1], M. Nocente[1], E. Panontin[1], D. Rigamonti[2], M. Tardocchi[2], A. Shevelev[3], E. Khilkevitch[3], M. Iliasova[3], L. Giacomelli[2], G. Gorini[1], G. Pautasso[4], G. Papp[4], G. Tardini[4], the EUROfusion MST1 Team[5] and the ASDEX Upgrade Team[6].

[1] *Dipartimento di Fisica Università degli Studi di Milano-Bicocca, Milan, Italy*
[2] *Istituto per la Scienza e Tecnologia dei Plasmi, CNR, Milan, Italy*
[3] *IOFFE Physical Technical Institute, Saint Petersburg, Russia*
[4] *Max-Planck-Intitut für Plasmaphysik, Garching bei München, Germany*
[5] *See the author list of "B. Labit et al 2019 Nucl. Fusion 59 086020"*
[6] *See the author list of "H. Meyer et.al. 2019 Nucl. Fusion accepted (https://doi.org/10.1088/1741-4326/ab18b8)"*

Electronic mail: a.dalmolin@campus.unimib.it

ABSTRACT

An optimized hard X-ray (HRX) spectrometer was designed to collect information from Bremsstrahlung emission in the MeV range runaway electrons (RE) generated during disruptions. The detector is based on a cerium doped lanthanum bromide scintillator crystal (LaBr3:Ce) coupled with a photomultiplier tube. The diagnostic allows for measurements of high hard X-ray fluxes in excess of 1 MHz with a wide dynamic range up to 20 MeV. The diagnostic was tested at the tokamak ASDEX Upgrade. The results achieved are promising and suggest the possibility of inferring information on the runaway electron energy distribution in tokamaks using deconvolution techniques.

INTRODUCTION

The production of relativistic REs during disruptions can potentially compromise the integrity of plasma-facing-components in large tokamaks and hinder operations [1]. Runaway electron production, control and mitigation are therefore currently one of the main topics studied in midsize and large-scale tokamaks. Information on the runaway electron energy distribution can be extracted by measuring the bremsstrahlung radiation emitted by the interaction between the beam and the post disruption plasma. In this work, we discuss the design of a custom hard X-ray spectrometer that can reliably measure the bremsstrahlung spectrum up to tenths of MeV with a high rate capability (> 1 MCps): the Runaway Electron GAmma-Ray Detection System (REGARDS).

EXPERIMENTAL SETUP

The REGARDS system can be divided into three distinct components: the hard X-ray (HXR) detector, the gain control system and the acquisition system. A schematic representation of the diagnostic can be found in figure 1.

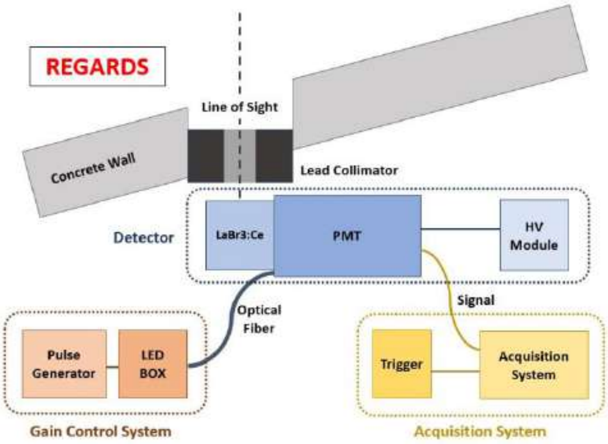

Fig. 1: A schematic representation of the REGARDS diagnostic.

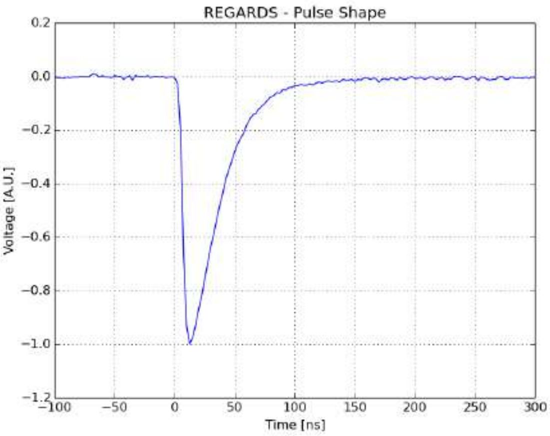

Fig. 2: A typical HXR signal from the REGARDS detector.

The HXR detector is made by a cerium doped lanthanum bromide (LaBr3:Ce) scintillator crystal coupled to a photomultiplier tube (PMT). The cylindrical scintillator measures 1 inch in diameter and 1 inch in length and it was manufactured by Saint-Gobain. The PMT used was manufactured by Hamamatsu (model R9420-100-10).

PMTs performances can be influenced by the presence of strong evolving magnetic fields. The detector was embedded in two layers of magnetic shielding to mitigate the influence of the external tokamak magnetic fields. The first layer is composed by a magnetic shield case by Hamamatsu (model E989-03) that covers the PMT. The second layer is a custom-made soft iron pipe that surrounds the whole detector and provides further shielding. Furthermore, the detector gain was monitored during the plasma discharge. This is achieved using a gain control system. The gain control system is composed by an electrical pulse generator, a blue LED and an optical fiber. The pulse generator (model 577 by Berkeley Nucleonics) is used to fire the blue LED (model NSPB500AS by Nichia) at a constant rate of 10 kHz. The light emitted by the LED is collected by an optical fiber and guided to the photocathode of the PMT. The gain control system was designed to mock the scintillation of a high energy photon of approximately 14 MeV interacting with the LaBr3:Ce crystal. During off-line analysis the gain stability of the detector can be assessed by retrieving the LED pulses by pulse shape discrimination techniques and monitoring their relative magnitude. This system can be also used to correct small gain shifts. In REGARDS the signal generated by the PMT is directly digitized by the ADC. The acquisition system (ADC model NI5772 with PXIe-7976 FlexRIO module by National Instruments) allows for continuous data collection at a 400 MHz sampling rate for more than 10 s. This is crucial to allow pile-up detection and recovery under high HXR fluxes.

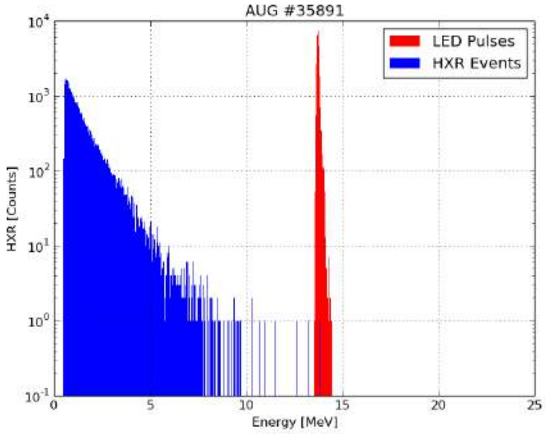

Fig. 3: Typical HXR spectrum measured during a disruption with RE formation at AUG.

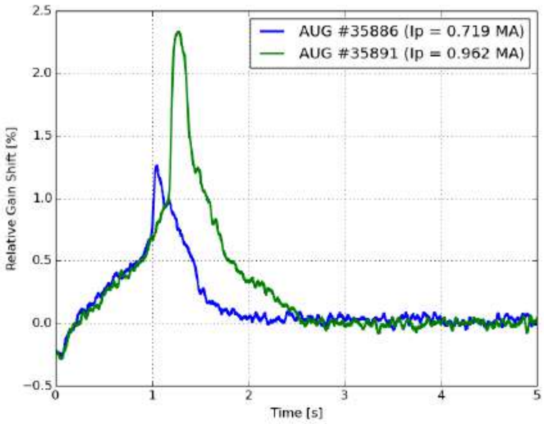

Fig. 4: Time trace of the detector relative gain shift during the discharge.

RESULTS

The REGARDS system was installed and tested at the tokamak ASDEX Upgrade during the 2019 MST1 T08-AUG campaign. The detector was placed in front of a radial view line of the machine, outside of the torus hall. A custom-made cylindrical lead collimator was used to reduce the incoming HXR flux. The PMT was operated at a relatively low supply voltage of -570 V to achieve a broad dynamical range of 20 MeV and to reduce the gain shift at high counting rates.

A typical HXR spectrum collected during a RE event is shown in figure 3. The energy of the RE bremsstrahlung emission (in blue) is mostly exponential with maximum HXR energies in the order of 10 MeV. In figure 3 the LED pulses used as reference are marked in red. The relative gain shift for two RE discharges obtained by monitoring the LED pulses is plotted in figure 4. Before the disruption is triggered (at t = 1.008 s for discharge #35886 and at t = 1.186 s for discharge #35891) there is a steady shift in the detector's gain due to the magnetic field ramp-up. This effect is proportional to the magnetic field intensity (Ip before the disruption is 0.719 MA for discharge #35886 and 0.962 MA for discharge #35891) and it counts for about 1%. After the disruption is triggered a sudden increase in the gain shift is caused by the high HXR flux. This effect is responsible for an additional 1.5% in the gain shift. The total gain shift for the REGARDS system is under 3% even in conditions of high HXR fluxes in excess of 1 MCps.

DISCUSSION AND CONCLUSION

During the tests performed at ASDEX Upgrade REGARDS proved to be a stable and reliable spectrometer even under high HXR flux. The capability of accurately measuring the RE bremsstrahlung emission in the MeV range opens the possibility of reconstructing the RE energy distribution using deconvolution techniques such as Tikhonov Regularization, Single Value Decomposition or Richardson Lucy Algorithm [2]. This information is of a great importance to understand RE beam formation, to assess the effectiveness of different RE mitigation techniques such as massive gas injection (MGI), shattered pellet injection (SPI) and magnetic resonant perturbation (RMP) and to validate first principle calculations.

ACKNOWLEDGMENT

This work has been carried out within the framework of the EUROfusion Consortium and has received funding from the Euratom research and training programme 2014-2018 and 2019-2020 under grant agreement No 633053. The views and opinions expressed herein do not necessarily reflect those of the European Commission.

REFERENCES

[1] Hender TC, Wesley JC et al., Nuclear Fusion **47** (2007) S128-S202.

[2] E. Panontin et al. "Development of Nuclear Radiation Based Tomography Methods for Runaway Electrons in Fusion Plasmas: First Results and Prospects" these proceedings.

IOP Publishing Measurement Science and Technology

Journal **XX** (XXXX) XXXXXX https://doi.org/XXXX/XXXX

A new hard X-ray spectrometer for runaway electron measurements in tokamaks

A. Dal Molin [1], M. Nocente [1], E. Panontin [1], D. Rigamonti [2], M. Tardocchi [2], A. Shevelev [3], E. Khilkevitch [3], M. Iliasova [3], L. Giacomelli [2], G. Gorini [1], E. Perelli [2], F. D'Isa [4], G. Pautasso [4], G. Papp [4], G. Tardini [4], COMPASS TEAM , the EUROfusion MST1 Team [5], the ASDEX Upgrade Team [4] and the COMPASS Team

[1] Dipartimento di Fisica Università degli Studi di Milano-Bicocca, Milano, Italy
[2] Istituto per la Scienza e Tecnologia dei Plasmi, CNR, Milan, Italy
[3] IOFFE Physical Technical Institute, Saint Petersburg, Russia
[4] Max-Planck-Intitut für Plasmaphysik, Garching bei München, Germany
[5] See the author list of H. Meyer et al., Nucl. Fusion 57 (2017) 102014

E-mail: a.dalmolin@campus.unimib.it

Received xxxxxx
Accepted for publication xxxxxx
Published xxxxxx

Abstract

In this work we present REGARDS, a novel hard X-ray detector system optimised for runaway electron bremsstrahlung radiation measurement. The detector is based on a 1"x1" LaBR3:Ce scintillator crystal coupled with a photomultiplier tube. The system has a dynamic range greater than 20 MeV, an energy resolution of 3% at 661.7 keV. The detector gain is very stable even under the severe HXR fluxes associated with runaway bremsstrahlung emission with a relative gain shift less than 3% at HXR counting rates in excess of 1 MCps. REGARDS performance allows for unprecedented studies of the time-evolving runaway electron energy distribution function. Here we present results obtained the tokamaks Asdex Upgrade and COMPASS during the 2019 runaway electron campaign of the Medium-Size Tokamaks programme (MST1).

Keywords: fusion, runaway electrons, hard X-Ray spectroscopy, plasma diagnostic, fast detector

1. Introduction

Runaway electron generation remains one of the major challenges to the success of large-size tokamak operation. During a disruption, a significantly large portion of the energy stored in the internal magnetic field can be efficiently transferred to the runaway electron beam. Once confinement is lost, these highly energetic particles can impact and damage plasma-facing components, hindering operation. On severe cases, the damage to the machine vessel can be significant enough to cause a long shutdown period for repairs of several months.

To avoid these extreme scenarios, extensive research is currently being carried out by the tokamak community. A large portion of this fundamental study is carried on the medium-size tokamaks Asdex Upgrade (AUG) and COMPASS where runaway electron beams are purposely generated to study the phenomenon.

During the generation process, runaway electrons can be accelerated to energies in the order of several MeV. These relativistic particles interact with the post-disruption plasma and emit bremsstrahlung radiation up to several MeV in hard X-ray energy range. Information on the runaway electron energy distribution function can be extracted measuring this

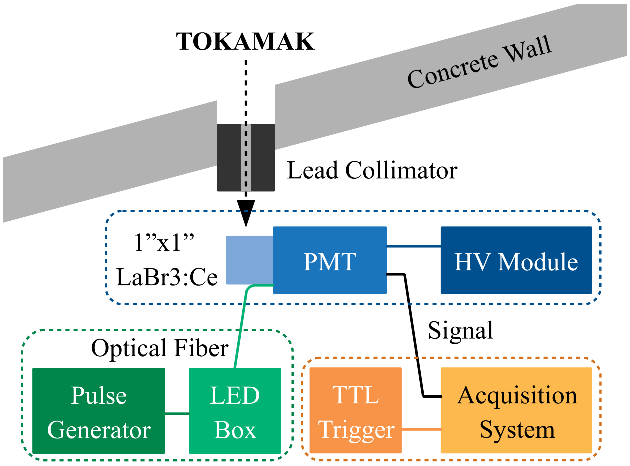

Figure 1. A schematic representation of the REGARDS system. The dotted boxes group the three main components of REGARDS: the HXR detector (in blue), the gain control system (in green) and the acquisition system (in orange).

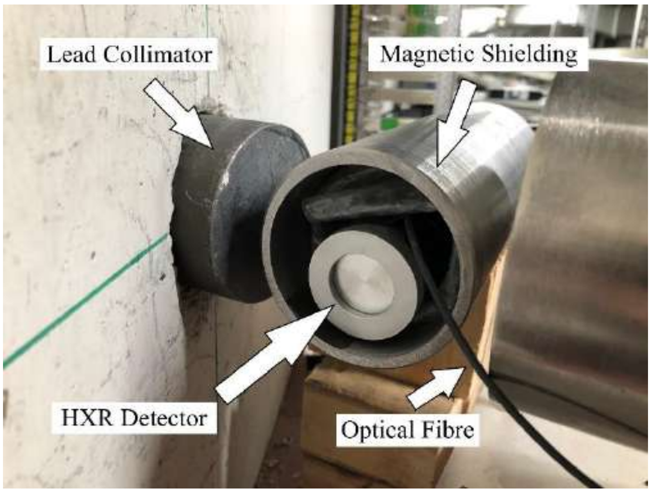

Figure 2. A picture of the REGARDS HXR detector installed at the Asdex Upgrade tokamak. The spectrometer is visible in its aluminium casing inside of the magnetic shielding soft iron pipe. On the left side of the picture the lead collimator is placed inside of the line of sight.

hard X-ray emission. In particular, this information is crucial to understand runaway electron formation, to validate first-principle models and to evaluate the effectiveness of different runaway electron mitigation techniques such as massive gas injection (MGI), shattered pellet injection (SPI) and magnetic resonant perturbation (RMP).

The measurement of the runaway bremsstrahlung radiation is challenging. When a runaway electron event is triggered in a medium-size or a large-scale tokamak the resulting bremsstrahlung radiation usually covers a large range of energies up to a few tens of MeV. Moreover, this radiation is usually emitted with very high photon fluxes of the order of several million photons per square centimetre per second even when measured at several meters from the tokamak. Finally, the evolution of the runaway electron distribution function is fast, in the order of few milliseconds. The challenging nature of runaway electron bremsstrahlung measurement requires for a fast diagnostic specifically designed for this task.

In this work, we present a new hard X-ray spectrometer optimised for runaway electron bremsstrahlung measurements: the Runaway Electron GAmma-Ray Detection System (REGARDS).

2. The Runaway Electron GAmma-Ray Detection System

The Runaway Electron GAmma-Ray Detection System (REGARDS) is a new portable hard X-ray spectrometer specifically designed to measure the bremsstrahlung radiation emitted by the interaction of the runaway electron beam with the post-disruption plasma. REGARDS has a dynamic range greater than 20 MeV and an energy resolution of approximately 3% at 661.7 keV. The variation of the system response is limited to few % for most operational scenarios, see section 3 for details.

This system was deployed during the 2019 MST1 runaway electron experimental campaign at the medium-size tokamaks AUG and COMPASS. Diagnostic performance and early physics results will be discussed in the following sections.

The strict requirements posed by the challenging nature of the runaway electron bremsstrahlung radiation were carefully addressed in the detector design. To facilitate the overview of REGARDS we can identify three main components of the system: the hard X-ray (HXR) detector, the gain control system and the acquisition system. Each of them will be discussed in a separate subsection. A schematic representation of the diagnostic can be found in figure 1. In this picture the dashed arrow represents the collimated line of sight coming from the tokamak to the HXR spectrometer. The blue dotted box encompasses the HXR detector while the green and the orange ones contain the gain control system and the acquisition system respectively.

2.1 The HXR detector

REGARDS employs a cerium doped lanthanum bromide (LaBr3:Ce) scintillator crystal coupled to a photomultiplier tube (PMT) as HXR detector. Lanthanum bromide was chosen as scintillator material for its fast primary scintillation decay time of approximately 25 ns. This ensures a very fast signal necessary for high counting rate operation. REGARDS uses a cylindrical crystal of 1 inch in diameter by 1 inch in length manufactured by Saint-Gobain.

The REGARDS PMT was manufactured by Hamamatsu (model R9420-100-10). It is usually operated at a low bias voltage of approximately -570 V to ensure a high dynamic

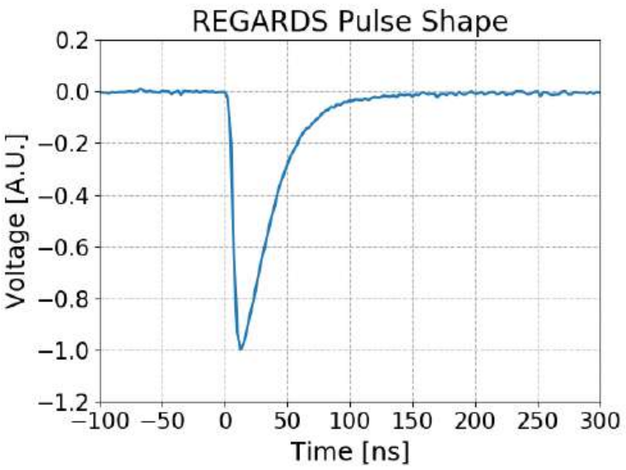

Figure 3. A typical REGARDS HXR signal. The fast pulse shape (FWHM ≈ 30 ns) is essential to reduce events pile-up and to allow operation with high counting rates.

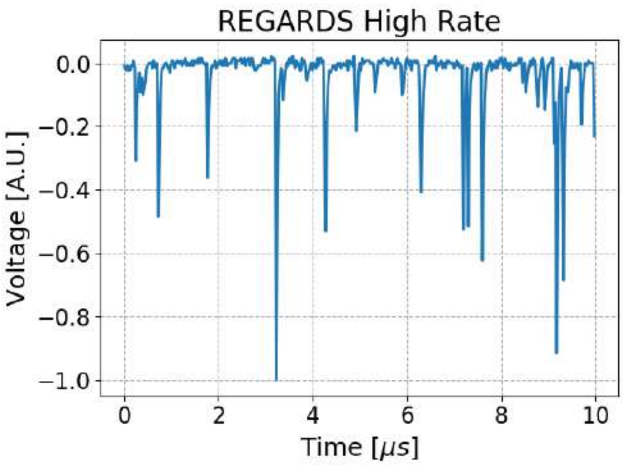

Figure 4. A typical signal time trace recorded during a high counting rate (> 1 MCps) phase of a plasma discharge. A limited number of pile-up events are visible and all signals are still recoverable using pile-up recovery algorithms.

range in excess of 20 MeV and to limit the relative gain shift at high counting rates to less than a few percent.

Tokamaks use intense magnetic fields to confine the plasma. These strong and evolving fields can perturb the behaviour of photomultiplier tubes, which are very sensitive to this kind of disturbance. To mitigate this effect the detector was embedded in two layers of magnetic shielding. The first layer is a μ-metal magnetic shield case by Hamamatsu (model E989-03) that completely envelops the PMT. The second and most external layer is provided by a custom-made soft iron pipe that surrounds the entire detector and provides further shielding.

A picture of REGARDS HXR detector assembled at the tokamak AUG can be found in figure 2. The tokamak is behind the wall on the left side of the picture. A lead collimator used to further reduce the HXR flux can be seen on the left side of the picture. The detector is visible in the centre of the image in its aluminium casing. The soft iron magnetic shielding pipe surrounds the detector. Finally, a black optical fibre can be seen in the lower right part of the picture. This optical fibre is part of the gain control system, as will be discussed in the next subsection.

The detector energy calibration is performed using radioactive gamma-ray sources of known emitted energy. For the calibration of this detector, ^{60}Co and ^{137}Cs were used. The energy resolution of REGARDS HXR detector is approximately 3% at 661.7 keV.

In figure 3 a typical HXR signal pulse shape measured by REGARDS is presented. The use of a fast inorganic scintillator in conjunction with a PMT allows for a very fast signal of approximately 100 ns. The full width at half-maximum of the signal is approximately 30 ns. This fast detector reduces the effects of pile-up and allows for HXR spectroscopy even at the high counting rates (up to a few MCps) in runaway electron discharges. Figure 4 shows a signal time trace recorded during a plasma discharge with counting rates greater than 1 MCps. As visible from the picture, due to the fast pulse shape only few pulses suffer from pile-up caused by the high HXR counting rate. Moreover, even when in pile-up, the individual pulses are still easily recognizable and they can be recovered using dedicated pile-up recovery algorithms.

2.2 The gain control system

There are two main effects that can modify the detector gain during runaway electron bremsstrahlung measurements. The first one is caused by the residual unshielded tokamak magnetic field interacting with the PMT and interfering with its multiplication stage. The second effect is caused by the PMT non-linear response as the current from the signal approaches the bias current. This last effect can become not negligible for runaway electron scenarios with high counting rates.

An external control system was developed to monitor the detector gain during the plasma discharge. This system is made of a blue light-emitting diode (model NSPB500AS by Nichia) mounted in a light-tight box, an electrical pulse generator (model 577 by Berkeley Nucleonics) and an optical fibre. The pulse generator is used to pilot the LED which is periodically fired at constant bias voltage. The light emitted by the LED is then transported to the PMT photocathode by the optical fibre. The parameters of the electrical pulse generator are adjusted such that the light emitted by the LED mocks the scintillation of a high energy photon interacting with the LaBr3:Ce crystal. For these experiments, we chose to fire the LED at a constant

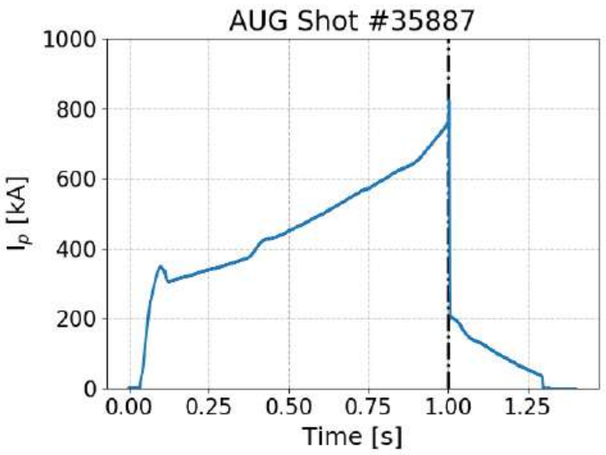

Figure 5. AUG plasma current during a runaway experiment. After the disruption triggered by a massive Ar gas injection at t = 1 s a 200 kA runaway beam is formed. The duration of the runaway electron beam is close to 300 ms.

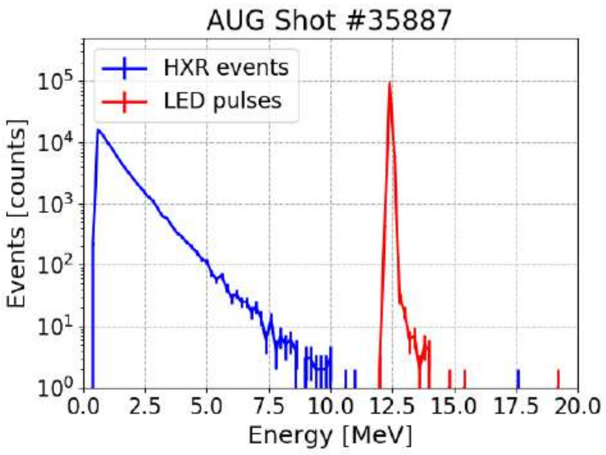

Figure 6. A RE bremsstrahlung spectrum measured at AUG using REGARDS (blue). The exponential spectrum reaches energies up to 10 MeV. The gain control system LED pulses collected during the discharge form the red peak at 12.5 MeV.

rate of 10 kHz with an equivalent HXR energy of approximately 12.5 MeV.

These LED pulses are acquired at the same time of the plasma discharge and then separated from the HXR signals using pulse shape discrimination techniques during off-line analysis. By comparing the amplitude of the LED pulses during the time of the discharge it is possible to quantify the gain shift of the diagnostic. If needed, this information can be used to perform offline corrections for small gain shifts below 10%.

2.3 The acquisition system

A crucial role in REGARDS performance is played by the acquisition system. Due to the very high rate of the HXR events associated with runaway electron bremsstrahlung, it is not preferable to operate with a triggered acquisition mode but to acquire all the data in a continuous stream. This mode prevents loss of data due to the acquisition dead time and facilitates pile-up detection and recovery under high HXR fluxes.

The PMT output signal is directly digitized by the ADC. The acquisition system for REGARDS is an ADC model NI5772 with PXIe-7976 FlexRIO module by National Instruments. This system allows for continuous data collection at a 400 MHz sampling rate for more than 10 seconds, which exceeds the duration of the heating phase in tokamaks without superconducting magnets.

The data acquisition is started with an external TTL trigger to ensure synchronisation with the plasma discharge and other diagnostics. Data is stored in non-volatile memory in the time between two plasma discharges, that are usually tens of minutes apart. This process takes a few minutes.

3. Diagnostic performance

REGARDS was first employed during the 2019 MST1 AUG runaway electron experimental campaign. The detector was installed along a radial line of sight of the tokamak, outside the torus hall, as shown in figure 1 and figure 2. The AUG torus hall wall is made of concrete and is 2 meters thick, providing good shielding from background radiation. The distance between the detector and the magnetic axis of the machine is approximately 11 meters. The line of sight is defined by a lead collimator inside the torus hall. To further limit the HXR flux on the detector an additional lead collimator with a cylindrical aperture of 1 cm in diameter and 10 cm thick was placed in front of the detector as shown in figure 2.

3.1 Runaway electron bremsstrahlung radiation

During a typical 2019 AUG runaway electron discharge the REGARDS acquisition time was set to 10 seconds, starting at the very beginning of the plasma discharge (t = 0 s). The runaway electron event was usually triggered approximately at t = 1 s through a massive gas injection. The generated runaway beam typically lasted for a few hundreds of milliseconds before confinement was lost. Figure 5 shows the plasma current measured during one of these experiments, AUG shot #35887. In the first part of the discharge the plasma current was steadily increased up to a desired value of 760 kA. At t = 1 s a plasma disruption was triggered using a massive gas injection of argon. In a plasma termination caused by a disruption but with no runaway electron formation, the measured current inside the plasma rapidly to drop to zero in a few tens of milliseconds. When a runaway electron beam is generated the current measured inside the plasma after the disruption does not drop to zero but matches the electric

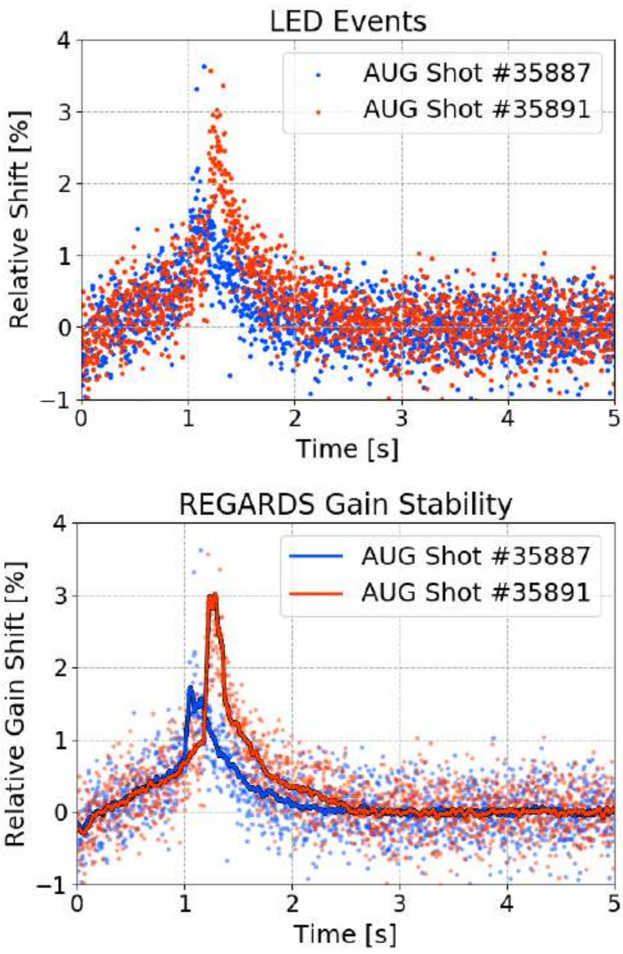

Figure 7. (a) The LED pulses collected during the plasma discharge presented as the relative shift from the unperturbed reference value for two different AUG discharges. (b) A Savitzky-Golay filter is applied to the same datasets to highlight the detector gain shift. Before the massive gas injection (at t = 1.008 s and at t = 1.186 s for discharges #35887 and #35891 respectively) a linear increase in the detector gain is caused by the increasing tokamak magnetic field. The great spike in the detector gain shift after the MGI is caused by the PMT non-linearity at high HXR counting rate. A slow recovery of the gain can be appreciated after the RE phase. The gain shift is < 3% at counting rates in excess of 1 MCps.

current carried by the beam. In figure 5 the current measured after the plasma disruption (t = 1 s) represent the runaway electron beam current.

After the massive gas injection, the runaway electron beam interacts with the post disruption plasma emitting radiation. The HXR spectrum of the runaway electron bremsstrahlung radiation collected during the entire time of the discharge is shown in figure 6 (in blue). The bin energy step is 100 keV. Bremsstrahlung has a continuous spectrum with a shape that is mostly exponential and reaches energies up to 10 MeV. Due to the nature of bremsstrahlung emission this suggests that a fraction of the runaway electrons in the beam in shot #35887 had energies greater than 10 MeV.

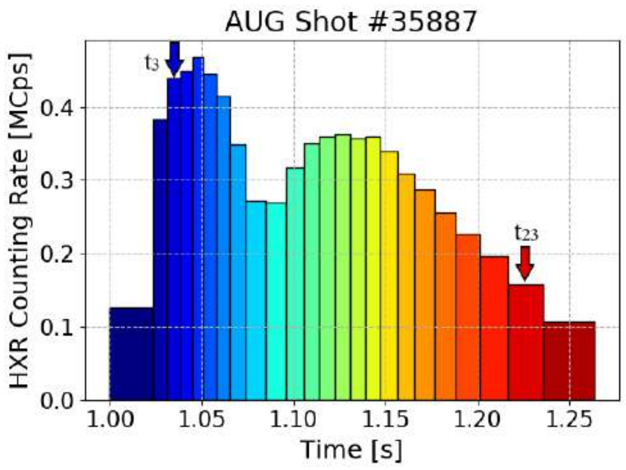

Figure 8. The HXR counting rate during discharge #35887 at AUG. Each bin contains 3000 events. The arrows indicate the two time windows selected to showcase a typical analysis of the shot in section 5.

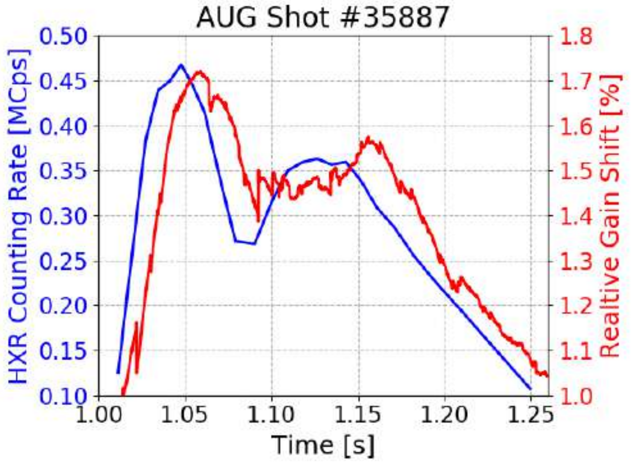

Figure 9. A comparison between the HXR counting rate (in blue) and the detector relative gain shift (in red) after the massive gas injection in shot #35887. A clear correlation between the two curves is visible, highlighting the effect of high counting rates on the detector stability and the importance of REGARDS gain control system for these high counting rate measurements.

A more detailed analysis of this HXR spectrum with examples of information that is possible extract from it will be presented in section 4.

3.2 Detector stability

During off-line analysis we can separate the HXR events from the LED pulses of the control monitor system using pulse shape algorithms. By studying the behaviour of the LED pulses during the discharge we can infer the detector gain stability. The total duration of a runaway experiment discharge at AUG was below 2 seconds. After t = 5 s we can assume the PMT gain to be stable since by that time no residual tokamak magnetic field or HXR radiation impinging on the detector are

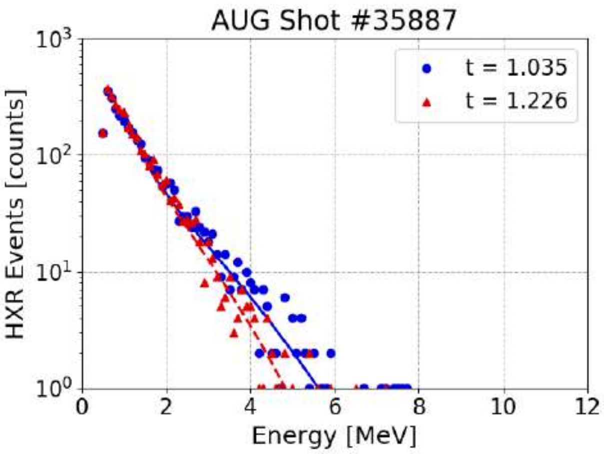

Figure 10. HXR spectra at two different stages of the RE beam evolution. The bin energy step is 100 keV. Each spectrum contains a total HXR 3000 counts. At the beginning of the RE phase the bremsstrahlung spectrum (blue dots) is more energetic than the one at the end of the discharge (red triangles) suggesting a similar evolution of RE beam maximum energy.

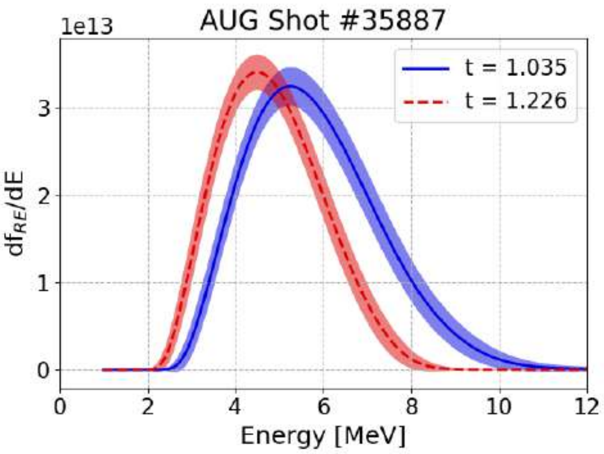

Figure 11. Reconstructed RE energy distribution functions for two different stages of the RE phase in discharge #35887. First-order Tikhonov regularization algorithm was used to recover this information from the two measured HXR spectra in figure 10. The algorithm ensures smooth non-negative solutions.

present. We compute the mean LED energy by averaging LED events over this time window (5 s ≤ t ≤ 10 s) and we use this mean value as a reference for unbiased gain. When not perturbed, the coefficient of variation of the LED events is $\sigma/\mu = 0.34\%$ which correspond to a LED energy resolution of approximately 0.8% at 12.5 MeV. We can estimate the detector gain shift by looking at the relative deviation of LED events from the reference value during the plasma discharge.

In figure 7 (a) the LED events during the plasma discharge are shown as the relative deviation from this computed mean for AUG discharges #35887 and #35891. In figure 7 (b) a Savitzky-Golay filter is applied to the data to highlight the behaviour of the detector gain (solid line). At the beginning of the discharges, from t = 0 s up to t ≈ 1 s we can see a linear increase in the gain shift. This effect is caused by the steady build-up of the plasma current and thus of the tokamak magnetic field in the initial phase of the discharge. After this initial phase, a sudden increase in the gain shift is clearly visible in correspondence of the runaway electron generation triggered by the massive gas injection, at t = 1.008 s for discharge #35887 and at t = 1.186 s for discharge #35891 respectively. This shift is caused by the PMT non-linearity at high currents caused by the high HXR flux on the detector. The maximum HXR counting rates measured were 0.48 MCps for discharge #35887 and 1.23 MCps for discharge #35891. Finally, after the short runaway electron phase, the system gain returns to the original unperturbed value in a few seconds.

Figure 8 shows the HXR events counting rate for discharge #35887 as a function of time. Each bin of the counting rate time trace contains 3000 HXR events. At t = 1.008 s the runaway event is triggered by the massive gas injection. Figure 9 shows a comparison between the HXR counting rate (in blue) and the relative detector gain shift (in red) during the time of the runaway electron event for discharge #35887. A clear correlation between the two curves is visible. The temporal delay in the relative gain shift of approximately 13 ms is due to the finite response time of the detector to the current changes. This plot exemplifies the effect that high counting rates can have on the data quality and highlights the importance of monitoring the detector gain using the gain control system. A more complete discussion on the high rate limitations of the REGARDs system is presented in section 5.

The data collected during the 2019 MST1 runaway electron campaign at AUG proved REGARDS to be a very stable system under severe HXR fluxes associated with runaway electron emission with a gain shift lower than 3% at high counting rates exceeding 1 MCps.

4. Example of results

REGARDS high performance allows to characterize the runaway electron beam evolution extracting information from the high energy component of the emitted bremsstrahlung radiation. In this section, we present the analysis of AUG shot #35887 to exemplify the analysis technique. A more exhaustive work on the analysis of the MST1 AUG runaway experiments is under way and will be published elsewhere.

To follow the evolution of the runaway electron beam we subdivide the measured HXR events in different time segments. For each time segment we then integrate the HXR events and produce an HXR spectrum of the runaway electron bremsstrahlung radiation. Finally, we analyse each spectrum to extract information on the runaway electron evolution during the discharge.

For this analysis the HXR events collected during the runaway electron phase of discharge were divided into 24 time

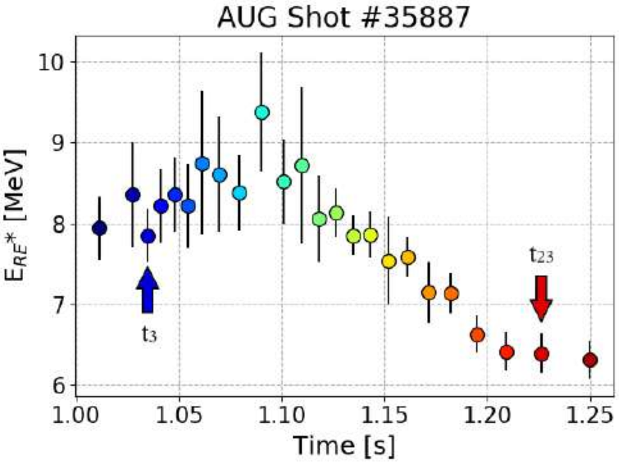

Figure 12. Maximum energy of the runaway electron beam during the discharge. A clear evolution of this parameter is visible. A small increase at the beginning of the RE phase is followed by an almost linear decrease in the maximum energy.

Figure 13. REGARDS detector setup at COMPASS. At the centre of the picture the soft iron pipe form magnetic shielding is visible. At its left, the cylindrical lead collimator and the black optical fibre are visible. Lead bricks were used to shield the detector from the background radiation.

windows, each one containing 3000 events, as shown in figure 8. The bin timesteps were adjusted to ensure a constant event population inside each bin. The bin population was chosen to ensure good HXR spectrum statistics without compromising the time resolution. To facilitate discussion data of each time window will be presented with the same colour coding used in figure 8.

The HXR spectra for time windows t_3 = 1.035 s and t_{23} = 1.226 s are shown in figure 10 (in blue dots and in red triangles respectively). These two spectra refer to different moments in the runaway electron beam evolution. The first one, t_3, is collected during the runaway electron beam formation while the second one, t_{23}, is closer to the end of the beam duration. Information on the runaway electron beam can be already inferred by noticing that the t_3 spectrum has a significantly large number of events at higher energies than t_{23}. This suggests a more energetic beam at t = t_3 and a less energetic beam a t = t_{23}.

More detailed information could be obtained by modelling the detector response and the RE bremsstrahlung emission and using deconvolution techniques to infer the underlying runaway electron energy distribution function from the measured HXR spectrum. This process is in practice an ill-posed problem, i.e. several different runaway energy distribution functions could explain the same measured HXR spectrum in the bounds of the experimental error. A common technique to address this problem is to use deconvolution algorithms such as Tikhonov regularization, Single Value Decomposition or Richardson-Lucy deconvolution to guide the selection of the solution with some prior knowledge of its features, such as smoothness or non-negativity. For a detailed analysis of the performance of these algorithms on this specific problem see [REF ENRICO].

First-order Tikhonov reconstruction was applied to the data of each of the 24 time windows to ensure a smooth and non-negative solution. Figure 11 shows the calculated runaway electron energy distribution functions for t = t_3 and t = t_{23}. The shaded area represents a 1-σ confidence interval in the reconstruction. We can notice that the runaway energy distribution at t = t_3 has higher average energy than the distribution at t = t_{23}. Moreover, the high energy tail of the t = t_3 distribution is significantly more populated than the t = t_{23} one. This confirms in a more quantitative way the previous observation on the runaway electron energy evolution we made directly from the HXR spectra.

Another parameter that can be extracted from these reconstructed RE energy distributions, and that is of great interest to describe the runaway electron evolution, is represented by the maximum energy of the beam. This parameter, referred here as E_{RE}^*, is the energy value at which the cumulative runaway electron energy distribution is equal to 90%. Figure 12 shows the time evolution of E_{RE}^* during the AUG plasma discharge #35887. A clear evolution of the runaway electron beam maximum energy is visible, with an initial increase of the beam maximum energy at the early stages of the beam formation and a subsequent and almost linear fall in the second half of the beam duration.

Information like the one presented in figure 12 is crucial to establish the behaviour of the runaway electron beam in different plasma scenarios and to establish the effectiveness of runaway electron mitigation techniques.

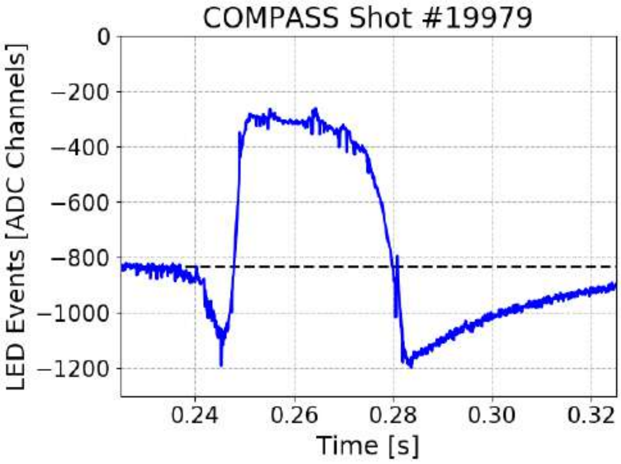

Figure 14. Time trace of the digitized LED pulses during COMPASS the discharge #19979. Only the maximum amplitude of each individual LED pulse is shown as a blue point on the graph. The average value of the unperturbed digitised LED events is shown in as a black dashed line. A clear deviation from the unperturbed value is visible during the runaway electron phase of the discharge,

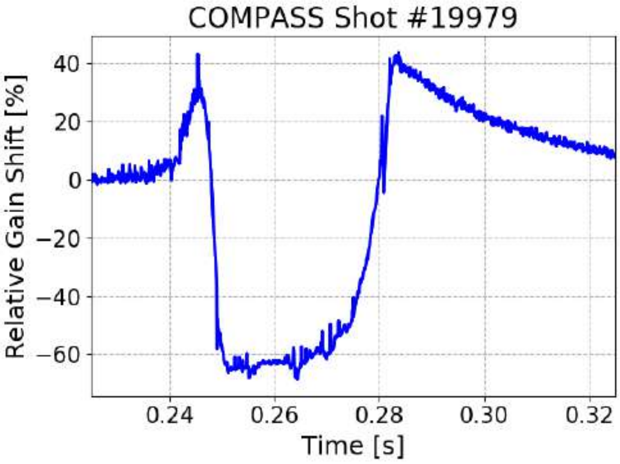

Figure 15. Detector relative gain for COMPASS discharge #19979. In the first phase of discharge the detector gain increases under the influence of the magnetic field and the HXR high flux up to +40 % at t = 0.245 s. Later the detector gain sharply dropped below a value of -60% under an estimated HXR rate in excess of 10 MCps. Detector gain recovery is visible after the termination of the runaway electron phase at t = 0.283 s.

5. COMPASS

One of the main characteristics of REGARDS is portability. The entire system was designed to be compact and easily transferrable to be installed and used at different MST1 facilities. In January 2020 REGARDS was installed at the medium-size tokamak COMPASS to collect preliminary data and test the detector performance at extremely high HXR fluxes. Extremely high fluxes were expected at COMPASS due to the proximity of the detector to the machine and the lack of an already existing collimated line of sight. The detector was shielded on site against background radiation using multiple lead blocks as show in figure 13.

The tests performed at COMPASS were useful to study the behaviour of REGARDS, and more in particular the robustness of the gain control system, under extreme high rates. A good example to highlight the behaviour of REGARDS under these challenging conditions is discharge #19979. During this shot REGARDS measured high HXR fluxes, with counting rates exceeding 10 MCps. Figure 14 shows the time trace of the digitized LED pulses during the discharge. To enhance readability, only the maximum amplitude of each individual LED pulse is shown. If no gain shift occurs, we expect the LED pulse amplitude to be constant in time within the statistical deviation presented in paragraph 3.2. The average value of the unperturbed digitised LED events corresponds to approximately - 830 ADC channels and it is shown in figure 14 by a black dashed line. A clear deviation of the LED pulse amplitude from the unperturbed value is visible during the discharge. Figure 15 shows the computed relative gain shift from the unperturbed value for the same discharge. In the first phase of discharge #19979, the detector gain increases under the influence of the magnetic field and the HXR high rate. In this initial phase a very high shift in excess of +40% was reached caused by an extreme HXR counting rate of 4 MCps at t = 0.245 s. After this point the HXR flux increased even more resulting in a sharp gain drop. During this second phase, the gain shift dropped below a value of -60% under an estimated HXR rate in excess of 10 MCps. The progressive detector gain recovery is visible only after the termination of the runaway electron phase (t = 0.283 s).

6. Discussion

An important aspect of a diagnostic system aimed at characterizing the time evolution of the runaway electron energy distribution is time resolution. REGARDS time resolution is limited by the HXR event statistics. If too few HXR events are detected during the discharge the integration window timestep must be increased to allow a significant number of counts in the HXR spectrum. This effect, limited to very low energy or extremely short beams, reduces the capability of capturing the fast components in the evolution of the runaway electron distribution function. A careful balance in the design of the detector position and collimation is therefore of extreme importance to allow for a desirable operation range with counting rates from 0.1 MCps to 1 MCps. This careful evaluation was performed for the AUG line of sight with the help of Monte Carlo models. The design of the lead collimator shown in figure 1 and 2 was based on these calculations. The management of the incident HXR flux at

AUG allowed for time resolutions of approximately 10 ms, that we deem sufficient for studying the evolution of the RE energy distribution function.

The tests performed at COMPASS showcase the complexity of RE bremsstrahlung measurements and the importance of the REGARDS gain control system. Severe HXR flux can drastically change the detector gain and behaviour. Without the external LED reference signal it would have been extremely difficult to ascertain if the variations in the measured HXR spectrum during the discharge were caused by a detector gain shift or by a real change in the underlying runaway electron distribution function. Moreover, the gain control system gives an immediate and quantitative measure of the detector stability during the discharge and thus on the data quality. Finally, this example highlights the importance of collimation to reduce the severe runaway electron HXR fluxes and to allow the detector to work in a suitable range of operation.

7. Conclusion

A new fast HXR detector optimised for runaway electron bremsstrahlung measurements was developed: the Runaway Electron GAmma-Ray Detection System. REGARDS was firstly deployed during the 2019 AUG MST1 runaway electron campaign with great success. The system proved to be very fast and very stable even under high HXR. The relative gain shift relative shift is inferior to 3% with HXR counting rates in excess of 1 MCps. The system dynamic range is greater than 20 MeV with an energy resolution of 3% at 661.7 keV. REGARDS is a portable device and it was also tested at COMPASS during the 2019 MST1 runaway electron campaign to ascertain the system limitations under extreme HXR fluxes. These tests proved the importance and the robustness of the REGARDS gain control system, underlying the importance of HXR management in RE bremsstrahlung measurement.

REGARDS allowed reconstruction of the runaway electron distribution function in the AUG MST1 runaway electron campaign with time resolutions of approximately 10 ms. Important quantities, such as the average and maximum energy of the RE beam, can be extracted and evaluated at different times of the discharge. This information is a crucial contribution to first-principle model validation and quantitative assessment of RE mitigation techniques. A more detailed work on the analysis of the 2019 AUG runaway experiments is currently being developed and will be published elsewhere.

REGARDS will continue to contribute in MST1 tokamaks such as AUG and the new COMPASS Upgrade in future runaway electron campaigns.

Acknowledgements

This work has been carried out within the framework of the EUROfusion Consortium and has received funding from the Euratom research and training programme 2014-2018 under grant agreement No 633053. The views and opinions expressed herein do not necessarily reflect those of the European Commission.

References

[1] Surname A, Surname B and Surname C 2015 *Journal Name* **37** 074203

[2] Surname A and Surname B 2009 *Journal Name* **23** 544

Novel compact hard X-ray spectrometer with MCps counting rate capabilities for runaway electron measurements on DIII-D[a]

A. Dal Molin,[1, b] L. Fumagalli,[1] M. Nocente,[1] D. Rigamonti,[2] M. Tardocchi,[2] L. Giacomelli,[2] E. Panontin,[1] A. Lvovskiy,[3] C. Paz-Soldan,[3] N. W. Edietis,[3] and G. Gorini[1]
[1] *Dipartimento di Fisica Università degli Studi di Milano-Bicocca, Milan, Italy.*
[2] *Istituto per la Scienza e Tecnologia dei Plasmi, CNR, Milan, Italy.*
[3] *General Atomics, San Diego, CA, United States of America.*

A novel compact spectrometer optimized for measurements of hard X-rays generated by runaway electrons is presented. The detector is designed to be installed in the fan-shaped collimator of the Gamma-Ray Imager diagnostic at the DIII-D tokamak. The spectrometer is based on a 1 cm x 1 cm cerium doped yttrium aluminium perovskite (YAP:Ce) scintillator crystal coupled with a silicon photomultiplier. The detector dynamic energy range is in excess of 10 MeV, with an energy resolution of approximately 10% at 661.7 keV. The fast detector signal ($\approx$ 70 ns full width at half maximum) allows for operation at counting rates in excess of 1 MCps. The gain stability of the system can be monitored in real-time using a light-emitting diode embedded in the instrument. The detector is expected to be deployed in the forthcoming DIII-D runaway electron experimental campaign.

I. INTRODUCTION

Currently, tokamaks represent one of the most studied and promising designs in fusion research. For this reason, the next generation of large-scale magnetic confinement devices is predominantly based on a high-current tokamak concept, with the ITER project being the prime example. ITER aims to demonstrate the feasibility of fusion as a commercially viable energy source by generating a ten-fold fusion power gain.

To achieve this ambitious goal, ITER will operate with a plasma current reaching up to 15 MA. During a plasma disruption, a large portion of this current can be efficiently converted into a runaway electron beam. An unmitigated impact of these relativistic particles beam could significantly damage first wall materials and cause long repair shutdowns. This scenario represents one of the major risks to the success of the ITER project and of the next generation of high-current tokamaks at large. As a consequence, the study of runaway electron generation, control and mitigation are currently prominent research topics amongst the magnetic confinement fusion community.

Recently, hard X-ray (HXR) spectroscopy techniques were adopted to study runaway electron formation and mitigation in medium and large-scale tokamaks. During their generation phase, runaway electrons can reach relativistic energies in the range of several MeVs. When these energetic particles interact with the post-disruption background plasma, bremsstrahlung radiation is emitted. Due to the high energy of the impinging particles, bremsstrahlung photons can also reach energies of several MeVs, in the range of hard X-ray (HXR) radiation. Useful information on the runaway electron distribution function can be obtained by measuring this hard X-ray bremsstrahlung radiation and adopting inversion techniques, such as Tikhonov regularization (*1–4*).

Spectroscopic measurement of runaway electron bremsstrahlung is challenging and requires dedicated instruments. Runaway electron bremsstrahlung can easily exceed photon fluxes of the order of 10^6 phs / cm^2 s even at several meters from the plasma column. To withstand this intense photon flux, while maintaining a useful temporal resolution to describe the fast-evolving runaway electron dynamics, high counting rate capability (> 1 MCps) spectrometers are needed. Moreover, these HXR detectors need to possess a wide dynamic energy range in excess of 10 MeV to fully capture the entirety of the bremsstrahlung spectrum. Moreover, HXR spectrometers need to be compact and insensitive to magnetic fields to be deployed in multi-line of sight systems close to tokamak.

In this paper we present the development of a novel HXR spectrometer optimised for the study of runaway electron bremsstrahlung emission and designed to be installed in array configuration at the DIII-D Gamma-Ray Imager (GRI) diagnostic (*5*, *6*).

II. HARD X-RAY DETECTOR

The HXR detector is based on a cerium doped yttrium aluminium perovskite (YAP:Ce) scintillator crystal coupled with a silicon photomultiplier (SiPM). Figure 1 shows a picture of the assembled HXR detector without its aluminum casing surrounding it. The cylindrical scintillator crystal measures 10 mm in diameter by 10 mm in length and was manufactured by Crytur (*7*). YAP:Ce is a very fast inorganic scintillator, with a scintillation decay time of approximately 25 ns. A fast scintillation decay time, coupled with a fast photodetector, is essential to achieve the high counting rate capabilities needed for this application. Moreover, YAP:Ce presents a good light yield of about 25 phs / keV and it is not hygroscopic. The crystal shape and dimensions were selected based on the results achieved at DIII-D by a previous HXR detector prototype (*8*) and dedicated MCNP simulations.

The close proximity of the GRI system to the DIII-D vessel and the consequent presence of high magnetic fields of few teslas at the detector location make the use of a photomultiplier tube as photodetector impractical. For this application, a silicon photomultiplier array (SiPM, model S13361-3050-NE04 by Hamamatsu (*9*)) was chosen instead. SiPMs are solid-state photodetectors made by thousands of avalanche

---

[a] Contributed paper published as part of the Proceedings of the Virtual 23rd Topical Conference on High-Temperature Plasma Diagnostics hosted by Los Alamos National Laboratory.

[b] Electronic mail: a.dalmolin@campus.unimib.it

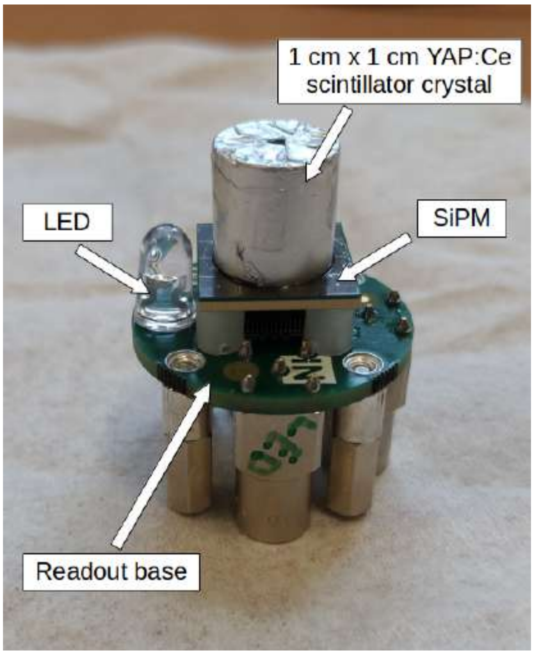

FIG. 1. A picture of the novel HXR spectrometer without its aluminum casing surrounding it. At the top of the picture the cylindrical YAP:Ce scintillator crystal is visible in its aluminum cladding. Below the crystal, the square SiPM used for photodetection and the internal LED used for detector gain monitoring are visible. Finally, the custom made readout board hosting the pulse shaping circuit and the connection ports can be appreciated at the bottom of the picture.

photodiodes connected in parallel and operated in Geiger mode. The relative small dimensions of these devices make them ideal for deployment in compact detectors. Moreover, SiPM are insensitive to magnetic fields and can reach high gains in the order of 10^5 - 10^6 (comparable to those of PMTs) at a relatively low bias voltage (near 60 V). Finally, it has been proven that SiPMs can sustain the high neutron flux associated with close proximity to tokamaks with little or no permanent damage (*10*).

A custom made pole-zero cancellation circuit is used to shape the detector signal. A more detailed description of the circuit design and working principle can be found in references (*11–14*). Figure 2 shows a typical pulse shape obtained for an HXR event detected by the YAP:Ce spectrometer. The signal has a fast rise time of $\approx$ 10 ns, a decay time of $\approx$ 45 ns, a pulse full width at half maximum of $\approx$ 70 ns and a pulse duration of $\approx$ 150 ns. This very fast signal reduces the probability of pile-up and allows for high counting rate operation in excess of 1 MCps.

SiPM gain is sensitive to temperature fluctuation. During a typical runaway electron discharge the amount of heat deposited into the detector is not sufficient to cause a noticeable deviation in the SiPM gain. As a result, data collected during a single discharge does not generally require offline correction of this effect. On the other hand, during a longer period of time of hours or days, the torus hall ambient temperature can change significantly, enough to cause a noticeable change in the detector gain. To ensure comparability between data collected across a large period of time, a temperature sensor was deposited on the back of the SiPM. This sensor is used to monitor and record the SiPM temperature throughout any single discharge and, if needed, these data can be used to correct the temperature induced gain shift when comparing different discharges.

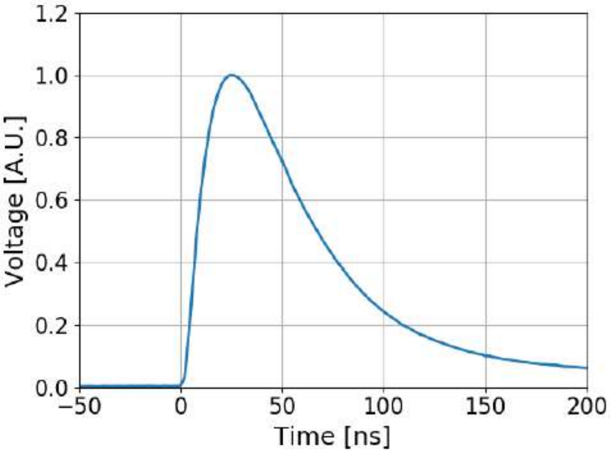

FIG. 2. Normalized output signal of the novel HXR spectrometer. The data shown is an average of 10 measured pulses. The combination of a fast inorganic scintillator crystal, a fast photodetector and dedicated pulse shaping circuit allow for signals with full with at half maximum of $\approx$ 70 ns.

As presented in more detail in the next section, under severe counting rates the signal current generated by the SiPM is high enough to cause a voltage drop on the avalanche photodiodes cells resulting in a consequent reduction in the detector gain. The magnitude of this effect was experimentally determined and results are presented in the next section. A light emitting diode (LED, model NSPB500AS by Nichia (*15*)) was installed inside the detector case near the SiPM. Taking advantage of the SiPM cells not covered by the scintillator crystal, the LED can be intermittently fired during operation to produce a constant reference light pulse and to provide online monitoring of the detector gain.

The detector energy resolution was measured using three radioactive sources, ^{22}Na (E_γ = 511 keV), ^{137}Cs (E_γ = 661.7 keV) and ^{60}Co (E_γ = 1332 keV). The results of these measurements are summarized in figure 3 in terms of energy resolution, i.e., the ratio of the full width at half maximum and the measured photo-peak energy. The detector energy resolution is better than 10% at 661.7 keV. The black dashed line shows the energy resolution extrapolated in the range of interest for runaway electron measurement.

III. MCPS COUNTING RATE CAPABILITY

At high counting rates ($\approx$ MCps), the output signal current produced by the SiPM can become significant, in the range of few mA. When this large output current flows through the SiPM quenching resistors, it can cause a voltage drop in the SiPM bias voltage. This produces an overall reduction in the detector gain (*12*). The SiPM gain at high counting rates is strictly decreasing as the output current increases. If left uncorrected, this effect produces an underestimation of the HXR enrgies.

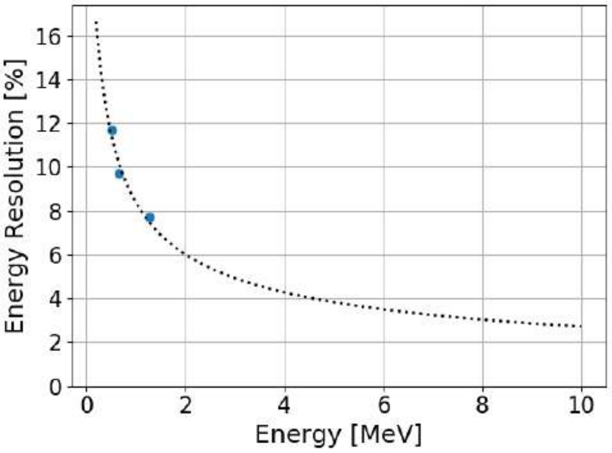

FIG. 3. Energy resolution of the novel HXR detector. Dots represent measurements obtained using radioactive sources (^{22}Na, ^{137}Cs and ^{60}Co respectively). The dashed black line represent the best fit of the collected data extrapolated over the region of interest for runaway electron bremsstrahlung measurements.

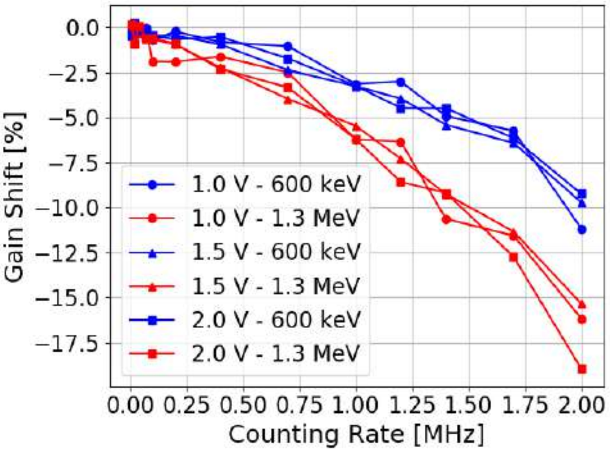

FIG. 4. The HXR detector response under high counting rates. Blue markers indicate the detector gain shift caused by LED events with an equivalent HXR energy of 600 keV, while the red ones with an equivalent energy 1.3 MeV. Different marker shapes represent different SiPM overvoltages used during the tests.

The magnitude of this effect was measured using a similar experimental setup to the one described in (*16*). The experimental setup consists of two blue LEDs (model NSPB500AS by Nichia (*15*)) that can be fired independently using an electrical pulser (Keysight model 81150A (*17*)). The SiPM is exposed to the light of the two LEDs using optical fibers. Light from the first LED is used to mock the scintillation light of an HXR with equivalent energy of 3 MeV. This LED is fired at a low rate of 10 kHz and its signal is used as a reference. The second LED mocks a lower equivalent energy HXR, either 0.6 MeV or 1.1 MeV. These light pulses are fired at a variable rate and are used to simulate the load on the SiPM generated by the measured radiation at different counting rates, with the LED equivalent energy representing the HXR radiation equivalent average energy.

A typical measurement starts with only the reference LED on. After a few seconds, the load LED is also turned on. The resulting signal current causes a small gain drop. This is visualized by a shift of the reference peak to the lower equivalent energies in the measured spectrum. By measuring this shift in the reference peak it is possible to quantify the relative detector gain shift introduced by the load. The results of these measurements can be appreciated in figure 4.

The detector gain shift increases more than linearly as a function of the load counting rate. One can also notice that doubling the equivalent energy of the load signal while keeping the firing rate fixed has the same effect of doubling the firing rate of the load signal while keeping the equivalent energy fixed, thus confirming that this shift is indeed caused by the output current. Moreover, for a load of approximately 0.6 MeV at a counting rate of 1.0 MHz, the detector shift is below 3.5% showing better performance than the previous prototypes (*8*, *12*, *13*).

IV. DETECTOR NON-LINEARITY

Silicon photomultipliers, due to the finite number of their avalanche photodiode cells and the limited recovery time needed for a fired pixel to return to its ready state, are intrinsically non-linear photodetectors. This is more evident when the number of scintillation photons impinging on the SiPM active surface is near to the total number of pixels in the SiPM. In this scenario, the probability of one or more of these photons to interact with an already firing pixel is not negligible. The larger the number of the scintillation photons, the higher the probability that a fraction of them will not contribute to the overall SiPM output, resulting in a smaller signal. Since the number of scintillation photons is proportional to the impinging HXR energy, non-linearity is more prominent for energetic HXRs.

An experimental setup was designed to measure the SiPM non-linearity as a function of energy (*8*). The light of a blue LED was split into two equal branches using optical fibres. One branch illuminated the SiPM through a small aperture in the YAP:Ce crystal aluminum cladding (still visible in figure 1) while the other illuminated an identical YAP:Ce crystal coupled with a photomultiplier tube (PMT, model R9420-100-10 by Hamamatsu (*18*)). Radioactive sources were used to provide energy calibration for both detectors. By adequately changing the piloting electrical pulser parameters, the LED emission can be shaped to mock the scintillation light generated by an HXR of variable equivalent energy. This emission was used to scan the equivalent HXR energy range, within the interval of the PMT linear response.

After correcting for the optical discrepancy introduced by the small difference in the two branches of optical fibers, the SiPM energy non-linearity was computed by confronting the energies measured by the two different detectors. The results of these measurements are presented in figure **??**.

As expected, the SiPM response is linear at low equivalent HXR energies and progressively deviates from the ideal behaviour as the equivalent HXR energy increases. At 10 MeV,

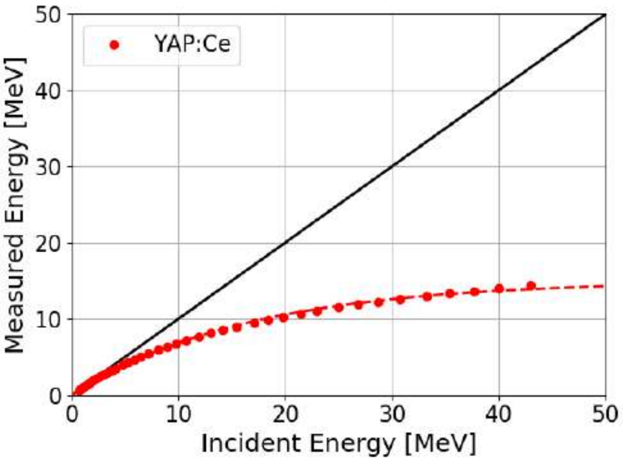

FIG. 5. Energy measured by the SiPM detector as a function of the equivalent HXR energy measured by the PMT. Red dots represent the collected data points while the dashed line is a best fit of the measured data. The solid black line indicates an ideal linear behaviour.

the non-linearity of the detector is approximately 30% and it reaches 50% at approximately 21 MeV.

V. CONCLUSIONS AND OUTLOOK

A novel HXR spectrometer optimized for runaway electron bremsstrahlung measurement was developed. Its compact size and insensitivity to magnetic fields make this design suitable for deployment in array configurations, such as the Gamma-Ray Imager at DIII-D. A very fast signal with a full width at half maximum of $\approx$ 70 ns was achieved by a combination of a fast inorganic scintillator crystal (YAP:Ce), a fast photodetector and dedicated pulse shaping electronics. Achieving fast signals in the order of 100 ns is essential to provide the high counting rate capability (> 1 MCps) the detector needs to sustain operation under the severe HXR fluxes associated with runaway electron bremsstrahlung emission. The detector showed good energy resolution of approximately 10% at 661.7 keV, which extrapolates favourably in the region of interest for runaway electron measurements.

In dedicated tests, the detector proved its stability under severe counting rates, obtaining a detector gain shift smaller than 3.5% under a load of approximately 600 keV at a rate of 1 MHz, improving on the results obtained by previous prototypes. This stability coupled with its fast signal provides the detector with high counting rate capability in excess of 1 MCps.

The detector energy non-linearity was characterized. The spectrometer presents a $\approx$ 30% deviation from linearity at 10 MeV and a 50% deviation at $\approx$ 21 MeV. It has to be noted that once the non-linear detector response is characterized, offline correction of the measured HXR spectra can be easily performed. The spectrometer presents a wide dynamic energy range in excess of 10 MeV, suitable for runaway electron bremsstrahlung measurements.

Development of this novel HXR spectrometer is now complete. The instrument is expected to be deployed in the forthcoming DIII-D runaway electron campaign when it will collect its first experimental data.

ACKNOWLEDGMENTS

This work has been carried out within the framework of the EUROfusion Consortium and has received funding from the Euratom research and training programme 2014-2018 and 2019-2020 under grant agreement No 633053. The views and opinions expressed herein do not necessarily reflect those of the European Commission.

This work supported in part by General Atomics Contract #4500085808.

REFERENCES

1. A. Lvovskiy *et al.*, *Plasma Physics and Controlled Fusion* **60**, 124003 (Nov. 2018).
2. A. Dal Molin *et al.*, presented at the 46th EPS Conference on Plasma Physics.
3. A. Lvovskiy *et al.*, *Nuclear Fusion* **59**, 124004, ISSN: 0029-5515 (Sept. 2019).
4. M. Nocente *et al.*, *Plasma Physics and Controlled Fusion* **62**, 014015, ISSN: 0741-3335 (Nov. 2019).
5. C. M. Cooper *et al.*, *Review of Scientific Instruments* **87**, 11E602 (Aug. 2016).
6. D. C. Pace *et al.*, *Review of Scientific Instruments* **87**, 043507 (Apr. 2016).
7. "YAP:Ce Technical Parameters", tech. rep. (Crytur), (`https://www.crytur.cz/materials/yap-ce/`).
8. A. Dal Molin *et al.*, *Review of Scientific Instruments* **89**, 10I134 (Oct. 2018).
9. "MPPC (Multi-Pixel Photon Counter) arrays S13361-3050 series", tech. rep. (Hamamatsu, 2020), (`https://www.hamamatsu.com/resources/pdf/ssd/s13361-3050_series_kapd1054e.pdf`).
10. D. Rigamonti *et al.*, *Journal of Instrumentation* **12**, C10007–C10007 (Oct. 2017).
11. M. Nocente *et al.*, *Review of Scientific Instruments* **85**, 11E108 (Nov. 2014).
12. M. Nocente *et al.*, *Review of Scientific Instruments* **87**, 11E714 (Aug. 2016).
13. D. Rigamonti *et al.*, *Review of Scientific Instruments* **87**, 11E717 (Aug. 2016).
14. D. Rigamonti *et al.*, *Review of Scientific Instruments* **89**, 10I116 (Oct. 2018).
15. "Specifications for blue LED NSPB500AS", tech. rep. (NICHIA Corporation).
16. M. Tardocchi *et al.*, *Review of Scientific Instruments* **79**, 10E524 (Oct. 2008).
17. "Keysight 81150A and 81160A Pulse Function Arbitrary Noise Generators", tech. rep. (Keysight Technologies, 2018).
18. "Photomultiplier Tube R9420", tech. rep. (Hamamatsu, 2014), (`https://www.hamamatsu.com/resources/pdf/etd/R9420_TPMH1296E.pdf`).

Bibliography

[1] Allen H. Boozer. "Theory of runaway electrons in ITER: Equations, important parameters, and implications for mitigation". In: *Physics of Plasmas* 22.3 (2015), p. 032504. DOI: `10.1063/1.4913582`.

[2] G. A. Wurden et al. "A New Vision for Fusion Energy Research: Fusion Rocket Engines for Planetary Defense". In: *Journal of Fusion Energy* 35.1 (2015), pp. 123–133. DOI: `10.1007/s10894-015-0034-1`.

[3] A. Gibson and JET Team. "Deuterium–tritium plasmas in the Joint European Torus (JET): Behavior and implications". In: *Physics of Plasmas* 5.5 (1998), pp. 1839–1847. DOI: `10.1063/1.872854`.

[4] John Wesson. *Tokamaks*. OXFORD UNIV PR, 2011. 812 pp. ISBN: 0199592233. URL: `https://www.ebook.de/de/product/14641403/john_wesson_tokamaks.html`.

[5] T.C Hender et al. "Chapter 3: MHD stability, operational limits and disruptions". In: *Nuclear Fusion* 47.6 (2007), S128–S202. DOI: `10.1088/0029-5515/47/6/s03`.

[6] H. Dreicer. "Electron and Ion Runaway in a Fully Ionized Gas. I". In: *Physical Review* 115.2 (1959), pp. 238–249. DOI: `10.1103/physrev.115.238`.

[7] H. Dreicer. "Electron and Ion Runaway in a Fully Ionized Gas. II". In: *Physical Review* 117.2 (1960), pp. 329–342. DOI: `10.1103/physrev.117.329`.

[8] J.W. Connor and R.J. Hastie. "Relativistic limitations on runaway electrons". In: *Nuclear Fusion* 15.3 (1975), pp. 415–424. DOI: `10.1088/0029-5515/15/3/007`.

[9] A. Stahl et al. "Effective Critical Electric Field for Runaway-Electron Generation". In: *Physical Review Letters* 114.11 (2015). DOI: `10.1103/physrevlett.114.115002`.

[10] Boris N. Breizman et al. "Physics of runaway electrons in tokamaks". In: *Nuclear Fusion* 59.8 (2019), p. 083001. DOI: `10.1088/1741-4326/ab1822`.

[11] M.N Rosenbluth and S.V Putvinski. "Theory for avalanche of runaway electrons in tokamaks". In: *Nuclear Fusion* 37.10 (1997), pp. 1355–1362. DOI: `10.1088/0029-5515/37/10/i03`.

[12] G Pautasso et al. "Plasma shut-down with fast impurity puff on ASDEX Upgrade". In: *Nuclear Fusion* 47.8 (2007), pp. 900–913. DOI: `10.1088/0029-5515/47/8/023`.

[13] S A Bozhenkov et al. "Generation and suppression of runaway electrons in disruption mitigation experiments in TEXTOR". In: *Plasma Physics and Controlled Fusion* 50.10 (2008), p. 105007. DOI: `10.1088/0741-3335/50/10/105007`.

[14] M. Lehnen et al. "Runaway generation during disruptions in JET and TEXTOR". In: *Journal of Nuclear Materials* 390-391 (2009), pp. 740–746. DOI: `10.1016/j.jnucmat.2009.01.200`.

[15] C. Reux et al. "Experimental study of disruption mitigation using massive injection of noble gases on Tore Supra". In: *Nuclear Fusion* 50.9 (2010), p. 095006. DOI: `10.1088/0029-5515/50/9/095006`.

[16] M. Lehnen et al. "Disruption mitigation by massive gas injection in JET". In: *Nuclear Fusion* 51.12 (2011), p. 123010. DOI: `10.1088/0029-5515/51/12/123010`.

[17] N. Commaux et al. "Demonstration of rapid shutdown using large shattered deuterium pellet injection in DIII-D". In: *Nuclear Fusion* 50.11 (2010), p. 112001. DOI: `10.1088/0029-5515/50/11/112001`.

[18] N. Commaux et al. "Novel rapid shutdown strategies for runaway electron suppression in DIII-D". In: *Nuclear Fusion* 51.10 (2011), p. 103001. DOI: `10.1088/0029-5515/51/10/103001`.

[19] N. Commaux et al. "First demonstration of rapid shutdown using neon shattered pellet injection for thermal quench mitigation on DIII-D". In: *Nuclear Fusion* 56.4 (2016), p. 046007. DOI: `10.1088/0029-5515/56/4/046007`.

[20] L.R. Baylor et al. "Disruption Mitigation System Developments and Design for ITER". In: *Fusion Science and Technology* 68.2 (2015), pp. 211–215. DOI: `10.13182/fst14-926`.

[21] M. Lehnen et al. "Suppression of Runaway Electrons by Resonant Magnetic Perturbations in TEXTOR Disruptions". In: *Physical Review Letters* 100.25 (2008). DOI: `10.1103/physrevlett.100.255003`.

[22] R Yoshino and S Tokuda. "Runaway electrons in magnetic turbulence and runaway current termination in tokamak discharges". In: *Nuclear Fusion* 40.7 (2000), pp. 1293–1309. DOI: `10.1088/0029-5515/40/7/302`.

[23] G Papp et al. "The effect of resonant magnetic perturbations on runaway electron transport in ITER". In: *Plasma Physics and Controlled Fusion* 54.12 (2012), p. 125008. DOI: `10.1088/0741-3335/54/12/125008`.

[24] M Gobbin et al. "Runaway electron mitigation by 3D fields in the ASDEX-Upgrade experiment". In: *Plasma Physics and Controlled Fusion* 60.1 (2017), p. 014036. DOI: `10.1088/1361-6587/aa90c4`.

[25] H. Bethe and W. Heitler. "On the stopping of fast particles and on the creation of positive electrons". In: *Proceedings of the Royal Society of London. Series A, Containing Papers of a Mathematical and Physical Character* 146.856 (1934), pp. 83–112. DOI: `10.1098/rspa.1934.0140`.

[26] Samuel Glasstone and Ralph H. Lovberg. *Controlled Thermonuclear Reactions*. Robert E. Krieger Publishing Company, 1975.

[27] Glenn F. Knoll. *Radiation Detection and Measurement*. John Wiley & Sons Inc, 2010. 864 pp. ISBN: 0470131489.

[28] C. M. Cooper et al. "Applying the new gamma ray imager diagnostic to measurements of runaway electron Bremsstrahlung radiation in the DIII-D Tokamak (invited)". In: *Review of Scientific Instruments* 87.11 (2016), 11E602. DOI: 10.1063/1.4961288.

[29] D. Rigamonti et al. "The upgraded JET gamma-ray cameras based on high resolution/high count rate compact spectrometers". In: *Review of Scientific Instruments* 89.10 (2018), p. 10I116. DOI: 10.1063/1.5038839.

[30] A. Dal Molin et al. "Development of a new compact gamma-ray spectrometer optimised for runaway electron measurements". In: *Review of Scientific Instruments* 89.10 (2018), p. 10I134. DOI: 10.1063/1.5038803.

[31] L. Martinelli. "Characterization of gamma ray spectrometers based on silicon photomultipliers and a LYSO crystal for fusion plasma diagnostics". MA thesis. Università degli Studi di Milano-Bicocca, 2017.

[32] C.L. Melcher and J.S. Schweitzer. "A promising new scintillator: cerium-doped lutetium oxyorthosilicate". In: *Nuclear Instruments and Methods in Physics Research Section A: Accelerators, Spectrometers, Detectors and Associated Equipment* 314.1 (1992), pp. 212–214. DOI: 10.1016/0168-9002(92)90517-8.

[33] C. L. Melcher. "Scintillation crystals for PET." In: *Journal of nuclear medicine : official publication, Society of Nuclear Medicine* 41 (6 2000), pp. 1051–1055. ISSN: 0161-5505. ppublish.

[34] *Scintillation Crystals*. Tech. rep. SCIONIX, 2020. URL: https://scionix.nl/scintillation-crystals/.

[35] *LYSO Scintillation Material*. Tech. rep. Saint Gobain, 2014. URL: https://www.crystals.saint-gobain.com/sites/imdf.crystals.com/files/documents/lyso-material-data-sheet_1.pdf.

[36] Richard Firestone. *Table of isotopes*. New York: Wiley, 1999. ISBN: 9780471330561.

[37] *Lanthanum Bromide Scintillators Performance Summary*. Tech. rep. Saint-Gobain, 2019. URL: https://www.crystals.saint-gobain.com/sites/imdf.crystals.com/files/documents/labr-performance-summary-2019.pdf.

[38] D. C. Pace et al. "Gamma ray imager on the DIII-D tokamak". In: *Review of Scientific Instruments* 87.4 (2016), p. 043507. DOI: 10.1063/1.4945566.

[39] *MPPC (Multi-Pixel Photon Counter) arrays S13361-3050 series*. Tech. rep. Hamamatsu, 2020. URL: https://www.hamamatsu.com/resources/pdf/ssd/s13361-3050_series_kapd1054e.pdf.

[40] *MPPC, Technical Note*. Tech. rep. Hamamatsu, 2017. URL: https://www.hamamatsu.com/resources/pdf/ssd/mppc_kapd9005e.pdf.

[41] D. Rigamonti et al. "Characterization of a compact LaBr3(Ce) detector with Silicon photomultipliers at high 14 MeV neutron fluxes". In: *Journal of Instrumentation* 12.10 (2017), pp. C10007–C10007. DOI: 10.1088/1748-0221/12/10/c10007.

[42] M. Nocente et al. "Experimental investigation of silicon photomultipliers as compact light readout systems for gamma-ray spectroscopy applications in fusion plasmas". In: *Review of Scientific Instruments* 85.11 (2014), 11E108. DOI: 10.1063/1.4886755.

[43] D. Rigamonti et al. "Performance of the prototype LaBr3 spectrometer developed for the JET gamma-ray camera upgrade". In: *Review of Scientific Instruments* 87.11 (2016), 11E717. DOI: 10.1063/1.4961060.

[44] *Photomultiplier Tube R9420*. Tech. rep. Hamamatsu, 2014. URL: https://www.hamamatsu.com/resources/pdf/etd/R9420_TPMH1296E.pdf.

[45] *Specifications for blue LED NSPB500AS*. Tech. rep. NICHIA Corporation.

[46] *Keysight 81150A and 81160A Pulse Function Arbitrary Noise Generators*. Tech. rep. Keysight Technologies, 2018.

[47] M. Tardocchi et al. "Gamma ray spectroscopy at high energy and high time resolution at JET". In: *Review of Scientific Instruments* 79.10 (2008), 10E524. DOI: 10.1063/1.2964205.

[48] *730 Digitizer Family*. Tech. rep. CAEN Electronic Instrumentation, 2019.

[49] M. Nocente et al. "Gamma-ray spectroscopy at MHz counting rates with a compact LaBr3 detector and silicon photomultipliers for fusion plasma applications". In: *Review of Scientific Instruments* 87.11 (2016), 11E714. DOI: 10.1063/1.4961073.

[50] A Lvovskiy et al. "The role of kinetic instabilities in formation of the runaway electron current after argon injection in DIII-D". In: *Plasma Physics and Controlled Fusion* 60.12 (2018), p. 124003. DOI: 10.1088/1361-6587/aae95a.

[51] A. Lvovskiy et al. "Observation of rapid frequency chirping instabilities driven by runaway electrons in a tokamak". In: *Nuclear Fusion* 59.12 (2019), p. 124004. ISSN: 0029-5515. DOI: 10.1088/1741-4326/ab4405.

[52] *YAP:Ce Technical Parameters*. Tech. rep. Crytur. URL: https://www.crytur.cz/materials/yap-ce/.

[53] E. V. D. van Loef et al. "High-energy-resolution scintillator: Ce3+ activated LaBr3". In: *Applied Physics Letters* 79.10 (2001), pp. 1573–1575. DOI: 10.1063/1.1385342.

[54] *Photomultiplier Tubes for Gamma Camera*. Tech. rep. Hamamatsu, 2007. URL: `https://www.hamamatsu.com/resources/pdf/etd/Gamma_PMT_TPMH1133E.pdf`.

[55] *Photomultiplier Tubes, Basics and Applications*. Tech. rep. Hamamatsu, 2007. URL: `https://www.hamamatsu.com/resources/pdf/etd/PMT_handbook_v3aE.pdf`.

[56] *NDT14xx, N14xxET, N1570 NIM & Desktop HV Power Supplies*. Tech. rep. CAEN Electronic Instrumentation, 2020.

[57] *NI-5772 Specifications*. Tech. rep. National Instruments, 2020. URL: `https://www.ni.com/documentation/en/digitizer-adapter-module-for-flexrio/latest/specs-ni-5772/specs/`.

[58] *BNC model 577*. Tech. rep. Berkeley Nucleonics.

[59] E. Panontin. "Analysis Methods for Gamma RayMeasurements from Runaway ElectronExperiments at ASDEX Upgrade". MA thesis. Università degli Studi di Milano-Bicocca, 2017.

[60] M. Nocente. "Neutron and gamma-ray emission spectroscopy as fast ion diagnostics in fusion plasmas". PhD thesis. Università degli Studi di Milano-Bicocca, 2012. URL: `http://hdl.handle.net/10281/28397`.

[61] M. Nocente et al. "Conceptual design of the radial gamma ray spectrometers system for α particle and runaway electron measurements at ITER". In: *Nuclear Fusion* 57.7 (2017), p. 076016. DOI: `10.1088/1741-4326/aa6f7d`.

[62] F. Salvat et al. "Monte Carlo simulation of bremsstrahlung emission by electrons". In: *Radiation Physics and Chemistry* 75.10 (2006), pp. 1201–1219. DOI: `10.1016/j.radphyschem.2005.05.008`.

[63] Francesc Salvat and JoséM. Fernández-Varea. "Semiempirical cross sections for the simulation of the energy loss of electrons and positrons in matter". In: *Nuclear Instruments and Methods in Physics Research Section B: Beam Interactions with Materials and Atoms* 63.3 (1992), pp. 255–269. DOI: `10.1016/0168-583x(92)95108-4`.

[64] C. J. Werner. *MCNP Users Manual - Code Version 6.2*. report LA-UR-17-29981. Los Alamos National Laboratory. 2017. URL: `https://mcnp.lanl.gov/pdf_files/la-ur-17-29981.pdf`.

[65] A. N. Tikhonov. "Solution of incorrectly formulated problems and the regularization method". In: *Soviet Math. Dokl.* 4 (1963), pp. 1035–1038.

[66] A. N. Tikhonov et al. *Numerical Methods for the Solution of Ill-Posed Problems*. Springer Netherlands, 1995. DOI: `10.1007/978-94-015-8480-7`.

[67] M. Salewski et al. "Measurement of a 2D fast-ion velocity distribution function by tomographic inversion of fast-ion D-alpha spectra". In: *Nuclear Fusion* 54.2 (2014), p. 023005. DOI: `10.1088/0029-5515/54/2/023005`.

[68] M. Salewski et al. “High-definition velocity-space tomography of fast-ion dynamics”. In: *Nuclear Fusion* 56.10 (2016), p. 106024. DOI: 10.1088/0029-5515/56/10/106024.

[69] M Weiland et al. “Enhancement of the FIDA diagnostic at ASDEX Upgrade for velocity space tomography”. In: *Plasma Physics and Controlled Fusion* 58.2 (2016), p. 025012. DOI: 10.1088/0741-3335/58/2/025012.

[70] A S Jacobsen et al. “Inversion methods for fast-ion velocity-space tomography in fusion plasmas”. In: *Plasma Physics and Controlled Fusion* 58.4 (2016), p. 045016. DOI: 10.1088/0741-3335/58/4/045016.

[71] M. Salewski et al. “MeV-range velocity-space tomography from gamma-ray and neutron emission spectrometry measurements at JET”. In: *Nuclear Fusion* 57.5 (2017), p. 056001. DOI: 10.1088/1741-4326/aa60e9.

[72] M. Weiland et al. “Phase-space resolved measurement of 2nd harmonic ion cyclotron heating using FIDA tomography at the ASDEX Upgrade tokamak”. In: *Nuclear Fusion* 57.11 (2017), p. 116058. DOI: 10.1088/1741-4326/aa7e0a.

[73] M. Salewski et al. “Alpha-particle velocity-space diagnostic in ITER”. In: *Nuclear Fusion* 58.9 (2018), p. 096019. DOI: 10.1088/1741-4326/aace05.

[74] Birgitte Madsen et al. “Fast-ion velocity-space tomography using slowing-down regularization in EAST plasmas with co- and counter-current neutral beam injection”. In: *Plasma Physics and Controlled Fusion* (2020). DOI: 10.1088/1361-6587/abb79b.

[75] B. Madsen et al. “Tomography of the positive-pitch fast-ion velocity distribution in DIII-D plasmas with Alfvén eigenmodes and neoclassical tearing modes”. In: *Nuclear Fusion* 60.6 (2020), p. 066024. DOI: 10.1088/1741-4326/ab82b5.

[76] P. Hansen. “The L-Curve and Its Use in the Numerical Treatment of Inverse Problems”. In: vol. 4. 2001, pp. 119–142.

[77] C. L. Lawson and R. J. Hanson. *Solving Least Square Problems*. CAMBRIDGE, 1987. 350 pp. ISBN: 0898713560. URL: https://www.ebook.de/de/product/7285518/charles_l_lawson_richard_j_hanson_solving_least_square_problems.html.

[78] Johnathan M. Bardsley and Curtis R. Vogel. “A Nonnegatively Constrained Convex Programming Method for Image Reconstruction”. In: *SIAM Journal on Scientific Computing* 25.4 (2004), pp. 1326–1343. DOI: 10.1137/s1064827502410451.

[79] J. M. Bardsley and N. Laobeul. “Tikhonov regularized Poisson likelihood estimation: theoretical justification and a computational method”. In: *Inverse Problems in Science and Engineering* 16.2 (2008), pp. 199–215. DOI: 10.1080/17415970701404235.

[80] G. Fussmann. “On the motion of runaway electrons in momentum space”. In: *Nuclear Fusion* 19.3 (1979), pp. 327–334. DOI: 10.1088/0029-5515/19/3/005.

[81] J. R. Martín-Solís et al. “Momentum–space structure of relativistic runaway electrons”. In: *Physics of Plasmas* 5.6 (1998), pp. 2370–2377. DOI: `10.1063/1.872911`.

[82] M. Bakhtiari, G. J. Kramer, and D. G. Whyte. “Momentum-space study of the effect of bremsstrahlung radiation on the energy of runaway electrons in tokamaks”. In: *Physics of Plasmas* 12.10 (2005), p. 102503. DOI: `10.1063/1.2065368`.

[83] I. Fernández-Gómez, J. R. Martín-Solís, and R. Sánchez. “Determination of the parametric region in which runaway electron energy losses are dominated by bremsstrahlung radiation in tokamaks”. In: *Physics of Plasmas* 14.7 (2007), p. 072503. DOI: `10.1063/1.2746219`.

[84] M. Nocente et al. “Energy resolution of gamma-ray spectroscopy of JET plasmas with a LaBr3 scintillator detector and digital data acquisition”. In: *Review of Scientific Instruments* 81.10 (2010), p. 10D321. DOI: `10.1063/1.3501386`.

[85] Marian Curuia et al. “Upgrade of the tangential gamma-ray spectrometer beamline for JET DT experiments”. In: *Fusion Engineering and Design* 123 (2017), pp. 749–753. DOI: `10.1016/j.fusengdes.2017.05.064`.

Ringraziamenti

Un ringraziamento speciale va a tutte quelle persone che mi sono state vicine e mi hanno sostenuto in questi anni. In primis alla mia famiglia, che non mi ha mai fatto mancare amore e che mi ha sempre spronato a perseguire le mie capacità fino in fondo. Ai miei amici, nuovi e vecchi, vicini e lontani, che hanno condiviso con me il peso nei momenti più faticosi e mi hanno ridato vigore e gioia nel proseguire. Ai miei colleghi che mi hanno insegnato con pazienza a fare ricerca. Ai miei compagni di banda e di coro, da cui ho imparato il valore del bello e l'importanza nel condividerlo. E infine a Isabella, la mia compagna, che più di tutti mi ha sorretto e incoraggiato in questi meravigliosi anni. Questo lavoro è in larga parte merito vostro, grazie.